First direct mass measurements on nobelium and lawrencium with the Penning trap mass spectrometer SHIPTRAP

Dissertation zur Erlangung des Grades
Doktor der Naturwissenschaften
am Fachbereich 08: Physik, Mathematik und Informatik
der Johannes Gutenberg-Universität Mainz

von
Michael Gerhard Dworschak
geboren in Miltenberg

Mainz 2009

1. Gutachter:
2. Gutachter:

Tag der mündlichen Prüfung: 08.12.2009

Erste direkte Massenmessungen an Nobelium- und Lawrenciumisotopen mit dem Penningfallen-Massenspektrometer SHIPTRAP

Das Penningfallen-Massenspektrometer SHIPTRAP wurde gebaut um Hochpräzisionsmassenmessungen an schweren Radionukliden durchzuführen, die in Fusionsreaktionen produziert und vom Geschwindigkeitsfilter SHIP vom Primärstrahl separiert werden. Es besteht aus einer Gaszelle zur Abbremsung der hochenergetischen Reaktionsprodukte, einem RFQ-Kühler und Buncher zur Kühlung und Akkumulation der Ionen und einem Doppel-Penningfallen-System um Massenmessungen durchzuführen. Die Masse wird durch die Messungen der Zyklotronfrequenz des entsprechenden Ions in einem starken homogenen Magnetfeld bestimmt. Diese Frequenz wird mit der Frequenz eines wohlbekannten Referenzions verglichen. Mit dieser Methode können relative Fehler in der Größenordnung von 10^{-8} erreicht werden. Kürzlich konnten die Massen der Nobeliumisotope $^{252-254}$No (Z=102) und des Lawrenciumisotops ^{255}Lr (Z=103) erstmals erfolgreich gemessen werden. Dies waren die ersten direkten Massenmessungen an Transuranen. Die Produktionrate dieser Atome lag bei etwa eins pro Sekunde und weniger. Die Ergebnisse der Massenmessungen an Nobelium bestätigen die früheren Massenwerte, die aus Q_α-Messungen abgeleitet wurden. Im Fall von ^{255}Lr wurde der Massenexzess, der bis dahin nur aus systematischen Trends abgeschätzt wurde, zum ersten Mal direkt bestimmt. Diese Ergebnisse sind ein erster Schritt für die an SHIPTRAP geplante Erforschung der Region der Transurane. Das Hauptziel ist hierbei die Bestimmung der Endpunkte der α-Zerfallsketten, die in superschweren Elementen in der Nähe der vorhergesagten Stabilitätsinsel ihren Ursprung nehmen.

First direct mass measurements on nobelium and lawrencium with the Penning trap mass spectrometer SHIPTRAP

The Penning trap mass spectrometer SHIPTRAP at GSI Darmstadt was set up for high-precision mass measurements of heavy radionuclides produced in fusion evaporation reactions and separated from the primary beam by the velocity filter SHIP. It consists of a gas stopping cell for the deceleration of the high energetic reaction products, an RFQ cooler and buncher for cooling and accumulation of the ions, and a double Penning trap system to perform mass measurements. The mass is determined by measuring the cyclotron frequency of the ion of interest in a strong homogeneous magnetic field and comparing it to the frequency of a well-known reference ion. With this method relative uncertainties in the order of 10^{-8} can be achieved. Recently, mass measurements of the three nobelium isotopes $^{252-254}$No (Z=102) and the lawrencium isotope ^{255}Lr (Z=103) were performed successfully. These were the first direct mass measurements of transuranium elements ever performed. The production rate of the atoms of interest was about one per second or less. The results of the measurements on nobelium confirm the previous mass values which were deduced from Q_α values. In the case of ^{255}Lr the mass excess value, which was previously only estimated from systematic trends, was for the first time directly measured. These results mark the first step in the exploration of the region of transuranium elements which is planned at SHIPTRAP. The main objective is to fix the endpoints of α decay chains which are originating from superheavy elements close to the predicted island of stability.

Contents

List of Figures

List of Tables

1 Introduction

For a long time the heaviest known element was uranium ($Z = 92$), which was discovered at the end of the 18$^{\text{th}}$ century. The discovery of the neutron in 1932 was a very important step for the production of transuranium elements. The first manmade species of this kind were produced by successive neutron capture and subsequent β^- decay starting from the uranium isotope ^{238}U. This chain of production was, however, interrupted. At this time it was not found obvious that spontaneous fission was the limiting factor.

From 1940 until 1955 the elements from neptunium ($Z = 93$) to mendelevium ($Z = 101$) were synthesized in nuclear reactions with neutrons or light ions as projectiles [Meld1967, McMi1949, Seab1946]. The half-life is rapidly decreasing as one climbs up in proton number. While the uranium isotope ^{238}U has a half-life of $4.5 \cdot 10^9$ years, which is around as much as the age of the earth, the longest-lived mendelevium isotope ^{258}Md has a half-life of only 52 days.

When physicists began to reveal the structure of the atomic nucleus an obvious reason for the limitation of the the stability of nuclear masses was found. The existence of high-Z elements was thought to be impossible due to the dominant effect of the Coulomb repulsion of the protons.

Predictions of the existence of heavier elements were derived from theoretical calculations taking into account microscopic shell corrections. On this basis a spherical shell closure was predicted at a proton number $Z = 114$ and a neutron number $N = 184$ [Mose1969, Nils1969]. Thus, one expected the nuclei in the vicinity of this shell closure to be comparably stable. The position of this so-called island of stability has been verified by later, more advanced calculations [Paty1991, Möll1992, Möll1994]. In addition these calculations predicted the existence of a region of deformed nuclei around a deformed shell closure at $Z = 108$ and a neutron number $N = 162$.

In order to verify these theoretical predictions it was necessary to develop new experimental methods first for the production of heavier elements and second for the study of their atomic and nuclear ground state properties. Advancing to elements heavier than mendelevium was made possible by the use of actinide targets which were bombarded with light ions ($Z = 5$ to 10) from accelerators. With this so-called hot fusion - where the excitation energy of the compound nucleus is in the order of 40 MeV - the elements from nobelium ($Z = 102$) to seaborgium ($Z = 106$) could be synthesized in the years from 1958 until 1974 [Fler1983, Seab1990].

In the last decades a remarkable progress in experimental facilities has been made which enabled the discovery of the elements up to $Z = 118$. The elements from bohrium ($Z = 107$) up to the element 112 - for which the name copernicium was recently suggested - were produced at SHIP [Münz1979] in so-called cold fusion reactions, where the excitation energy of the compound nucleus is in the order of 20 MeV or even less. This is achieved by using stable targets - lead or bismuth - and

projectile beams in the order of $Z = 20$ to 30. Higher-Z elements were produced in Dubna (Russia) using actinide targets[1] [Ogan2007]. The production of superheavy elements is very demanding to the apparatus since the production cross sections are extremely low. Although the intensity of the ion beams available at today's accelerator facilities have been increased significantly, the production rates for the heaviest elements are still in the order of one ion per week for element 112.

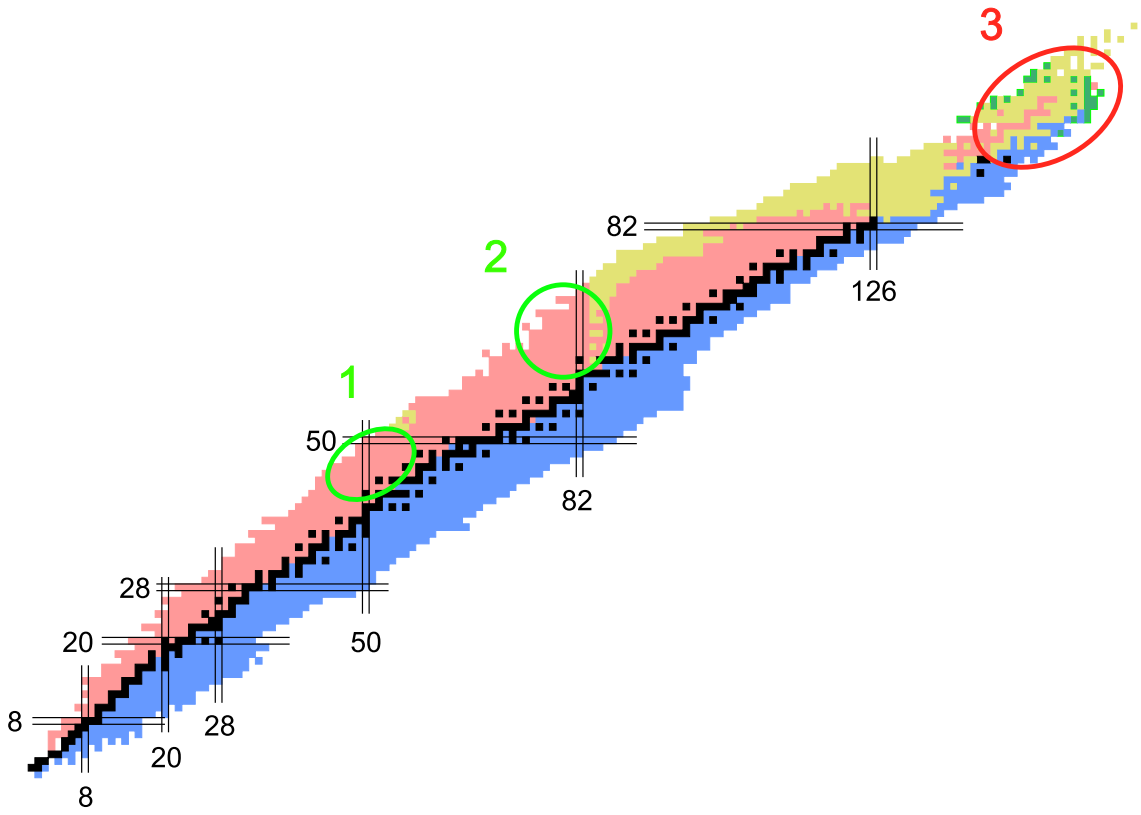

Figure 1.1: The different regions of interest at SHIPTRAP are illustrated on the chart of nuclides. The region of rp-process endpoints (1), proton emitters (2) and transuranium elements (3) have been addressed already by SHIPTRAP [Bloc2007].

The existence of these elements can only be explained with the strong influence of shell effects and thus confirms the previously developed theories. The question of what is the heaviest element that can exist is thus linked with the understanding of the stabilization effect due to changes in the shell structure. Measuring the properties of superheavy elements is thus of utmost importance to improve the knowledge about the behaviour of nuclear matter in extreme conditions. One still missing experimental prove is the discovery of the island of stability. Although the nuclides investigated until now are already very close to it, the final step is still missing.

The knowledge about the superheavy elements which are already known is still

[1] The element 113 was produced in RIKEN (Japan) using a zinc beam on a bismuth target. It was, however, already observed before as a decay product of element 115, which was produced at Dubna.

rather limited. Since the binding energy is the reason for the stability of the superheavy elements it is important to have reliable mass values of nuclei in this region. Until 2008 there was no nuclide heavier than uranium whose mass has been measured directly. The masses in this region were based on measurements of decay energies. This implies non-negligible uncertainties, which increase with the length of the decay chain.

It was thus desirable to have an independent check for the masses determined indirectly by measuring decay energies. The most precise way to perform mass measurements is by using Penning traps [Blau2006]. With this tool it is possible to determine the mass by measuring the cyclotron frequency of a trapped ion. The first precision experiment with a Penning trap was performed by the Nobel laureate of 1989, H. Dehmelt, who used it to measure the g-factor of the electron and the positron [Dehm1990]. The first facility with the aim of measuring the masses of short-lived nuclei with a Penning trap was the mass spectrometer ISOLTRAP [Boll1996, Mukh2008], which is installed at CERN. There, the masses of more than 200 short-lived species could be measured; in the most cases with a considerable improvement compared to previous measurements.

Inspired by the success of this experiment among many others a new Penning trap facility was planned which was dedicated to the measurement of masses in the region of the superheavy nuclides. In order to have access to superheavy nuclides this new Penning trap system was installed behind the velocity filter SHIP at GSI. This facility, named SHIPTRAP, is producing data since 2005. It is focusing mainly on three regions of the chart of nuclides. The first region in the vicinity of the doubly-magic nucleus ^{100}Sn is the expected end of the rp-process in the tin-antimony-tellurium cycle [Scha2001] (see Fig. 1.1). The mass values are here needed for the determination of the proton separation energies. The second region is concerned with neutron-deficient nuclides around $A \approx 150$ at the proton drip-line including ground-state proton emitters. The third region, which is the main goal of SHIPTRAP and the topic of this thesis, are the transfermium elements.

During an experiment performed at SHIPTRAP in 2008, the masses of the three nobelium ($Z = 102$) isotopes ^{252,253,254}No have been directly measured for the first time. These ions are the heaviest radionuclides ever measured directly. These nuclides are linked via α decays to isotopes of the element darmstadtium, which has the proton number $Z = 110$. In 2009 a further experiment aiming for the element lawrencium ($Z = 103$) was started. In this thesis the results of these experiments are presented and discussed.

In Chap. 2 an overview over the most important theoretical mass models is given. The experimental setup of the high precision mass spectrometer SHIPTRAP is presented in Chap. 3. Finally, in Chap. 4 the performance of the experiment is described and the obtained data are discussed.

2 Nuclear mass models

Nuclear masses are of interest since they contain all information about the inner structure of nuclei. Since Einstein postulated the energy-mass equivalence the mass of a nuclide is interpreted as the total energy of it constituents, the so-called nucleons. When forming a nuclide the nucleons lose a certain part of their mass and convert it into binding energy. This binding energy prevents the nucleus from decaying. The basic problem is here the understanding of the attracting force keeping the nucleons together. Due to the electromagnetic force there should be a strong repulsive force between the positive charged protons. Indeed one is observing that for increasing proton number Z a higher neutron number N is needed to make the nuclide stable. The highest stable $N = Z$ nuclide is ^{40}Ca. For heavier nuclides N has to be larger than Z to achieve stability. So it is obvious that some attractive force between the nucleons has to exist to guarantee the stability of the nuclide. This so-called strong-interaction is acting only between two neighbouring nucleons by the exchange of mesons. This strong force has been the basis of many theoretical nuclear models. However, the interaction of $A = N + Z$ particles is soon becoming very complicated and cannot be solved exactly. For this reason one has to find suitable approximations of the interaction between the single particles.

The first mass models were purely macroscopic (see Sec. 2.1). Later microscopic corrections were added to these macroscopic models (see Sec. 2.2) and also purely microscopic approaches were made (see Sec. 2.3). This chapter gives a short overview over some of the most important nuclear mass models, especially for the heavy and super heavy mass region. In section 2.4 conclusions with respect to heavy nuclides are drawn.

2.1 The liquid-drop model

The first attempt to describe the binding energy of a nucleus in a macroscopic way was done by Carl Friedrich von Weizsäcker in the year 1935 [Weiz1935]. It treats the nucleus as a drop of an incompressible homogeneous liquid which is kept together by the nuclear force. The binding energy E_B was explained as a consequence of five contributions[1] which will be explained in the following:

$$E_B = E_{Vol} + E_{Surf} + E_{Coul} + E_{Asym} + E_{Pair}. \tag{2.1}$$

[1]The ansatz given by von Weizsäcker in [Weiz1935] is starting with $E_B = E_V + E_S + E_C$. In the formula with which he concludes this publication the quantities a_x also show a dependence on N and Z. At this point it was found to be more illustrative to chose later forms of the binding energy of the liquid-drop model instead of discussing the original formula of von Weizsäcker.

To be consistent with the mass formulas discussed in the following sections the binding energy E_B is here defined as a negative value due to

$$m_{atom} = m_n N + (m_p + m_e)Z + \frac{E_B}{c^2} + \frac{E_{B_e}}{c^2}. \tag{2.2}$$

This is different from von Weizsäcker's definition, who has defined the binding energy as a positive value. Due to the definition in Eq. (2.2) a small binding energy is favorable since it leads to a higher stability of the nucleus. m_n is the neutron mass, m_p the proton mass, m_e the electron mass and E_{B_e} the binding energies of the electrons. The mass formula of Eq. (2.2) thus describes the mass of an atom and not only the mass of the nucleus.

The first term of Eq. (2.1), $E_{Vol} = -a_{Vol} \cdot A$, is resulting from the strong interaction between the single nucleons. This interaction, however, has a very short range and thus is only affecting the neighboring particles. It is assumed that this contribution to the binding energy is proportional to the mass number A and thus to the volume of the nucleus. Therefore, it is also called *volume energy*. The constant a_{Vol} is about 15.67 MeV.

The second term, the so-called *surface energy*, is taking into account that the nucleons at the surface of the nucleus have fewer direct neighbours than nucleons in the center and are therefore less bound. The *surface energy* is a negative contribution to the binding energy and is written as $E_{Surf} = a_{Surf} \cdot A^{\frac{2}{3}}$, with $a_{Surf} \approx 17.23$ MeV. The dependence on $A^{\frac{2}{3}}$ is due to the fact that the surface is proportional to r^2 and r is proportional to $A^{\frac{1}{3}}$.

The third term describes the Coulomb repulsion of the protons in the nucleus and is therefore called *Coulomb energy*. Derived from the Coulomb potential $V_{Coul} = q/(4\pi\epsilon_0 r)$ it is written as $E_{Coul} = a_{Coul} \cdot Z^2 \cdot A^{-\frac{1}{3}}$, with a_{Coul} being approximately 0.714 MeV. This term is also a positive contribution to the binding energy and is one reason that causes nuclei with high Z to be unstable.

The fourth term is based on the assumption that symmetric neutron and proton configurations are favorable. Each quantum state can only be populated with two particles since protons and neutrons are both fermions. The highest populated state is defining the fermi energy. Configurations in which protons and neutrons have the same fermi energy are assumed to be more stable. Thus, the so-called *asymmetry energy term* is chosen in a way that it vanishes for $N = Z$:

$$E_{Asym} = a_{Asym} \cdot \frac{(\frac{A}{2} - Z)^2}{A}. \tag{2.3}$$

For nuclei with $N \neq Z$ it has a positive contribution to the binding energy. The constant a_{Asym} is about 93.15 MeV.

The last term, the so-called *pairing correction*, is an empirical correction to the liquid-drop model. It is defined as

$$E_{Pair} = \begin{cases} -a_{Pair} \cdot A^{-\frac{1}{2}} & \text{for even-even nuclides} \\ 0 & \text{for even-odd nuclides} \\ +a_{Pair} \cdot A^{-\frac{1}{2}} & \text{for odd-odd nuclides .} \end{cases}$$

The increased stability for even-even nuclides is explained with the combination of two neutrons or two protons to a nucleon pair which leads to a smaller binding energy. The quantity a_{Pair} is approximately 11.2 MeV.

With this formula the main trends in atomic masses known at that time were reproduced reasonably well. There is, however, a significant systematic deviation which shows a relatively high stability for certain proton and neutron numbers Z, $N = 2$, 8, 20, 28, 50, 82 (see Fig. 2.1). These numbers are called "magic" numbers and can be explained with the influence of shell effects [Maye1948]. Analogue to the electrons in the atomic shells the nucleons are also regarded to be arranged in shells. A closed shell leads to an increased stability or to a higher binding energy, respectively. The difference to the atomic shell is that there exist now two kinds of particles. Protons have a repulsive Coulomb force between each other and neutrons are electrically neutral particles. Both kinds of particles, however, are interacting due to a short-ranged nuclear force.

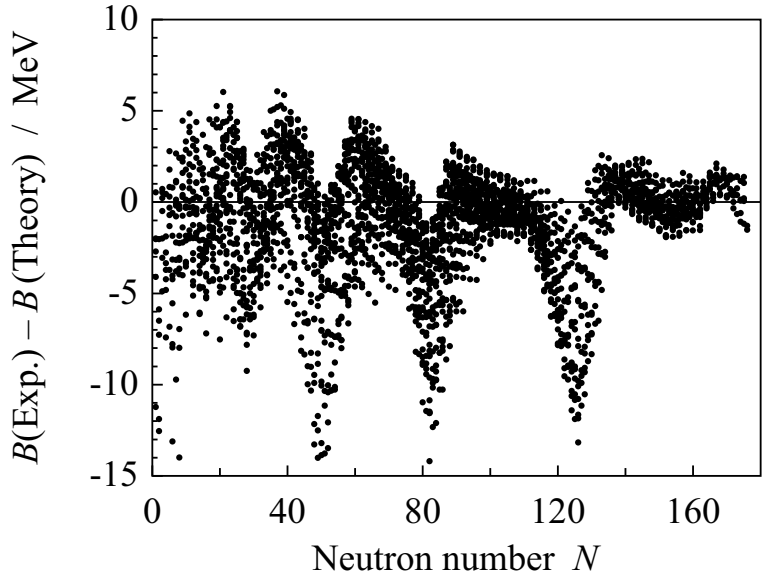

Figure 2.1: The deviation of the mass values predicted by von Weizsäcker and the experimental results of the Atomic Mass Evaluation (AME) [Audi2003] is shown.

Obviously it is necessary to extend the liquid-drop model with additional terms that take shell effects into account, as discussed in Sec. 2.2. With these corrections the liquid-drop model, which starts from a macroscopic ansatz, is still used today. Apart from this there exist also microscopic approaches for the calculation of nuclear masses. Two of these approaches, the Hartree-Fock-Bogolyubov ansatz and the Skyrme-Hartree-Fock BCS ansatz, are described in section 2.3.

2.2 The macroscopic-microscopic model

Due to the significant deviation of the masses obtained with the liquid-drop model mass formula from the experimental values it was obvious that further modifications had to be made. One possibility was to perform *ab initio* calculations only taking into account the basic natural constants. This possibility will be described in chapter 2.3. In addition, since the liquid-drop model already has pointed out a quite promising approach to predict nuclear masses, it was not completely given up but further developed. Several attempts have been made to correct the deviations due to the shell effects by adding additional microscopic terms to the liquid-drop model mass formula. The first attempt was made by Myers and Swiatecki in 1966 (see Sec. 2.2.1) taking into account shell corrections only for spherical nuclei. Strutinsky in 1967 developed an ansatz (see Sec. 2.2.2) which is still today the basis of many macroscopic-microscopic calculations. Two of these are presented in the following, namely the finite-range liquid-drop model (see Sec. 2.2.3) and the finite-range droplet model (see Sec. 2.2.4), both in the form given by [Möll1995].

2.2.1 The approach of Myers and Swiatecki

The first attempt to include shell effects into theoretical calculations was made by Myers and Swiatecki [Myer1966]. The calculations are based on the liquid-drop model (see Chap. 2.1) and contain some additional contributions to the total mass. The deviations from the masses of nuclides at magic numbers are explained by the so-called *bunching* of single particle energy levels. Furthermore, some modifications to address non-spherical nuclear shapes were made. This is an important advantage compared to the liquid-drop model in which all nuclides were supposed to have spherical shape. The binding energy is given by

$$E_B = E_{Vol} + E_{Surf} + E_{Coul} + E_{Pair} + E_{Wig} + S(N,Z) \cdot e^{-\frac{\overline{(\delta R)^2}}{a^2}}. \qquad (2.4)$$

The first four terms are already appearing in Eq. (2.1). The Wigner term is an additional contribution to the binding energy which was added to obtain a better reproducibility of the masses of light nuclides ($A < 50$). It has the form $E_{Wig} = V_{Wig} \cdot e^{-\lambda\frac{|N-Z|}{A}}$ and has some resemblance with the asymmetric energy term in Eq. (2.1), with the difference that the neutron excess is now appearing in the exponent. The Wigner energy V_{Wig} is here a negative constant which was found to be -7 MeV in this case [Myer1966]. λ was in the same publication chosen to be 6. This term mainly corrects for deviations observed before on the $N = Z$ line. For nuclei with increasing $|N - Z|$ this term approaches to zero.

The shell effects are included in the last term of Eq. (2.4) which is defined as

$$S(N,Z) = \sum \epsilon_i(bunched) - \sum \epsilon_i(unbunched). \qquad (2.5)$$

ϵ_i are the single-particle contributions to the total energy. The exponential term contains the distortion of the nucleus which is defined as the root-mean-square value of the deviation of the radius R from its average value R_0. R is dependent on the

azimuthal and polar angles and is defining the nuclear surface. The distortion is obtained by integrating over the whole solid angle 4π due to the equation

$$\overline{(\delta R)^2} = \frac{\int (R - R_0)^2 d\Omega}{\int d\Omega}. \tag{2.6}$$

The distortion disappears for nuclei with spherical shape which means that the shell corrections in Eq. (2.4) are at maximum for this case. For non-zero distortions the factor $e^{-\frac{\overline{(\delta R)^2}}{a^2}}$ is attenuating the shell effect term $S(N, Z)$ and makes it finally disappearing for big distortions. This assumption that the shell effects are negligible for strongly deformed nuclei, however, turns later out to be incorrect.

The optimum parameters are found by comparing the predictions of the mass formula with experimental results. Regarding the deviation to the experimental data after several iterations of optimization one can state that the formula of Myers and Swiatecki marks an improvement compared to the purely macroscopic liquid-drop model. It was the first step to include shell corrections and thus combining macroscopic and microscopic calculations. This method was then further developed by using the Strutinsky ansatz, which is described in the following.

2.2.2 The Strutinsky ansatz

Only one year after Myers and Swiatecki had included the first shell corrections into the liquid-drop model a new attempt was made to add microscopic corrections to a macroscopic model. This so-called Strutinsky theorem [Stru1967, Stru1968] (named after V.M. Strutinksy) is still today the basis of most of the macroscopic-microscopic models and is therefore shortly summarized.

Using this ansatz, the total binding energy of a nucleus E_B is calculated as the sum of the liquid-drop model energy E_{LDM}, the shell corrections δS and the pairing corrections δP:

$$E_B = E_{LDM} + \sum_{p,n} (\delta S + \delta P). \tag{2.7}$$

The shell corrections δS are determined by calculating the difference between the shell energy for a realistic nuclear level scheme with non-uniform level spacings

$$S = \sum_i n_i \epsilon_i \tag{2.8}$$

and a uniform level distribution

$$\tilde{S} = \int_{-\infty}^{+\infty} \epsilon g(\epsilon) d\epsilon. \tag{2.9}$$

ϵ_i are the single particle energy eigenvalues and n_i are the corresponding occupation numbers. The function $g(\epsilon)$ is defined as

$$g(\epsilon) = \frac{1}{\gamma\sqrt{\pi}} \sum_i n_i e^{-\frac{(\epsilon - \epsilon_i)^2}{\gamma^2}}, \tag{2.10}$$

with γ being a smearing parameter. The shell corrections δS are calculated for different values for γ aiming for a plateau in which δS is more or less constant for variations of γ in a wide range. This can be achieved for nuclei close to the stability line, while the results for nuclei far from stability are not satisfying.

The pairing corrections δP are calculated in a similar manner using the BCS (Bardeen-Cooper-Schrieffer) theory. The influence of the pairing will be described while discussing the purely microscopic model (see Sec. 2.3).

2.2.3 The finite-range liquid-drop model

The finite-range liquid-drop model (FRLDM) has been derived from the liquid-drop model by including further correction terms. Although it does not reproduce the experimental data as well as the finite-range droplet model (FRDM, see Sec. 2.2.4) it is still shortly described here for reasons of completeness. Many terms that appear in the FRDM are already showing up in the FRLDM. In this section only the macroscopic terms are presented. The microscopic corrections are calculated using the Strutinsky ansatz (see Sec. 2.2.2) and are similar for FRLDM and FRDM.

The macroscopic part of the binding energy of a nuclide can be written as [Möll1995]

$$E_B = E_{Vol}+E_{Surf}+E_{Coul}+E_{Asym}+E_{Pair}+E_{Wig}+E_{Form}+E_{Exch}+E_{A^0}+E_{El}. \quad (2.11)$$

Some terms are in principle already known from equations (2.1) and (2.4). They are, however, slightly modified.

The volume energy term E_{Vol} contains in addition to the dependence on the mass number A also a dependence on the relative neutron excess $I = \frac{N-Z}{A}$ and the volume-asymmetry constant κ_{Vol}:

$$E_{Vol} = -a_{Vol}(1 - \kappa_{Vol} I^2)A. \quad (2.12)$$

Analogue the surface energy term E_{Surf} is also extended by I, the surface-asymmetry constant κ_{Surf} and the relative generalized surface energy B_1. It is written as

$$E_{Surf} = a_{Surf}(1 - \kappa_{Surf} I^2)B_1 A^{2/3}. \quad (2.13)$$

This modification is taking into account the finite range of the interaction between two nucleons.

The Coulomb term E_{Coul} has the same form as in the liquid-drop model in Sec. 2.1. The Coulomb constant a_{Coul} is here related to the elementary charge e, the nuclear radius constant r_0 and the relative Coulomb energy B_3:

$$a_{Coul} = \frac{3}{5} \cdot \frac{e^2}{r_0} B_3. \quad (2.14)$$

The charge asymmetry energy term E_{Asym} is defined to be proportional to $N - Z$:

$$E_{Asym} = -a_{Asym}(N - Z). \quad (2.15)$$

The pairing energy E_{Pair} is now not only distinguishing between three but between four cases:

$$E_{Pair} = \begin{cases} \overline{\Delta}_n + \overline{\Delta}_p - \delta_{np} & Z \text{ and } N \text{ odd} \\ \overline{\Delta}_p & Z \text{ odd and } N \text{ even} \\ \overline{\Delta}_n & Z \text{ even and } N \text{ odd} \\ 0 & Z \text{ and } N \text{ even} . \end{cases}$$

As before the highest stability is obtained in the case that both, Z and N, are even. In this case E_{Pair} is zero. In the other cases it is dependent on the average neutron pairing gap $\overline{\Delta}_n$, the average proton pairing gap $\overline{\Delta}_p$ and the average neutron-proton interaction energy δ_{np}, which are defined as

$$\overline{\Delta}_n = \frac{r_{mac} B_S}{N^{1/3}} \tag{2.16}$$

$$\overline{\Delta}_p = \frac{r_{mac} B_S}{Z^{1/3}} \tag{2.17}$$

$$\delta_{np} = \frac{h}{B_S A^{2/3}}. \tag{2.18}$$

r_{mac} is the average pairing gap constant and h is the neutron-proton interaction constant. B_S is the relative surface energy, which is defined as the ratio of the surface area of the nucleus at the actual shape to the surface area at the spherical shape.

The Wigner energy is given by $E_{Wig} = W/A$ in case that $I = 0$ and N and Z are odd numbers and $E_{Wig} = W \cdot |I|$ in all other cases. W is a positive constant, the so-called Wigner constant. Also this term results in a higher stability for even-even nuclides.

The proton form-factor term E_{Form} is newly introduced here and given as a function of the Fermi wave number k_F and the proton root-mean-square radius r_p:

$$E_{Form} = f(k_F r_p) \frac{Z^2}{A}. \tag{2.19}$$

It is a positive contribution to the total mass, which means that it makes the nucleus more unstable.

The Coulomb exchange correction energy term E_{Exch} is given by

$$E_{Exch} = -a_{Exch} \cdot \frac{Z^{4/3}}{A^{1/3}} \tag{2.20}$$

with

$$a_{Exch} = -\frac{3}{4} \cdot \left(\frac{3}{2\pi}\right)^{2/3} \cdot \frac{e^2}{r_0}, \tag{2.21}$$

where e is the elementary charge and r_0 is the nuclear radius constant. Since E_{Exch} is negative it contributes to a higher stability of the nucleus.

The A^0 energy term E_{A^0} is a pure phenomenological term and is written as

$$E_{A^0} = a_0 \cdot A^0. \tag{2.22}$$

Table 2.1: The constants of the FRLDM from [Möll1995].

a_{Vol}	16.00126	MeV
κ_{Vol}	1.92240	MeV
a_{Surf}	21.18466	MeV
κ_{Surf}	2.345	MeV
r_0	1.16	fm
a_{Asym}	0.10289	MeV
r_{mac}	4.80	MeV
h	6.6	MeV
W	30	MeV
r_p	0.80	fm
a_{A^0}	2.615	MeV
a_{El}	14.33	eV

The last term, E_{El}, is taking into account the energy of the bound electrons. It is given by

$$E_{El} = -a_{El} \cdot Z^{2.39}, \tag{2.23}$$

with a_{El} being the electronic-binding constant. The influence of the electrons in the atomic shell is thus identified as a contribution to a higher stability of the nucleus. The constants of the FRLDM from [Möll1995] are listed in Tab. 2.1.

2.2.4 The finite-range droplet model

The finite-range droplet model is an extension of the finite-range liquid-drop model including some additional macroscopic terms. The main difference is that the FRLDM - as the liquid-drop model - still implies the incompressibility of the nuclear material. The FRDM, in contrary, is allowing for compression of nuclear material by an additional compressibility term $\Delta E_{B,compr}$ which is added to the macroscopic part of the binding energy. It is written as [Möll1995]

$$\Delta E_{B,compr} = E_{Curv} + E_{VR} + E_{SR}. \tag{2.24}$$

The term describing the volume energy is again extended and is now dependent on the symmetry-energy constant J, the average nuclear asymmetry $\bar{\delta}$, the nuclear compressibility constant K and the average relative deviation of the nuclear density from its average value $\bar{\epsilon}$. It is written as

$$E_{Vol} = (-a_{Vol} + J\bar{\delta}^2 - \frac{1}{2}K\bar{\epsilon}^2)A. \tag{2.25}$$

$\bar{\delta}$ is dependent on the mass number A, the proton number Z, the relative neutron excess I, the neutron skin energy

$$B_V \propto \int_S \bar{W}(r)dS, \tag{2.26}$$

Table 2.2: The constants of the FRDM from [Möll1995].

a_{Vol}	16.247	MeV
J	32.73	MeV
K	240	MeV
a_{Surf}	22.92	MeV
a	0.68	fm
Q	29.21	MeV
r_0	1.16	fm
a_{Asym}	0.436	MeV
r_{mac}	4.80	MeV
h	6.6	MeV
W	30	MeV
r_p	0.80	fm
a_{A^0}	0	
a_{El}	14.33	eV
a_{Curv}	0	

the surface energy

$$B_{Surf} = \frac{A^{-2/3}}{4\pi r_0^2} \int_S dS \tag{2.27}$$

and the relative generalized surface or nuclear energy

$$B_1 \propto \int\int_V \left(2 - \frac{|r - r'|}{a}\right) \frac{e^{|r-r'|/a}}{|r - r'|/a} d^3r d^3r' \tag{2.28}$$

and some additional constants. The constant a is the range of the Yukawa-plus-exponential potential. The expression for $\bar{\epsilon}$ is containing the exponential term $Ce^{-\gamma A^{1/3}}$ which was added to obtain a better description of compressibility effects. C characterizes the strength and γ the range of this term.

The expression for the surface energy is modified to

$$E_{Surf} = (a_{Surf} B_1 + \frac{9}{4}\frac{J^2}{Q}\bar{\delta}^2 \frac{B_{Surf}^2}{B_1}) A^{2/3}, \tag{2.29}$$

with Q being the effective surface-stiffness constant. The additional term is mainly correcting for finite range effects.

The terms for the Coulomb energy E_{Coul}, the asymmetry energy E_{Asym}, the pairing energy E_{Pair}, the Wigner energy E_{Wig}, the proton form-factor correction to the Coulomb energy E_{Form}, the Coulomb exchange correction energy E_{Exch}, the A^0 energy E_{A^0} and the energy of the bound electrons E_{El} are identical with the ones of the FRLDM (see Sec. 2.2.3). Only some of the constants are different (see Tab. 2.2).

The first additional term, the curvature energy, is given by

$$E_{Curv} = a_{Curv} B_k A^{1/3}, \tag{2.30}$$

where B_k is proportional to the integral over the radii of curvature R_1 and R_2:

$$B_k \propto \int_S \left(\frac{1}{R_1} + \frac{1}{R_2}\right) dS. \tag{2.31}$$

The volume redistribution energy term E_{VR} has the form

$$E_{VR} = -a_{VR} B_r Z^2 A^{1/3}. \tag{2.32}$$

The constant a_{VR} is defined as

$$a_{VR} = \frac{3}{2800}\left(\frac{1}{J} + \frac{18}{K}\right)\frac{e^4}{r_0^2}. \tag{2.33}$$

The volume redistribution energy B_r is proportional to $\int_V [\bar{W}(r)]^2 dV$. $\bar{W}(r)$ is defined as

$$\bar{W}(r) = W(r) - \bar{W}, \tag{2.34}$$

with

$$W(r) = \int_V \frac{1}{|r - r'|} d^3r' \tag{2.35}$$

and

$$\bar{W} \propto \int_V W(r) d^3r. \tag{2.36}$$

The surface redistribution energy term E_{SR} is given by

$$E_{SR} = -a_{SR}\frac{B_w B_{Surf}}{B_1} Z^2, \tag{2.37}$$

with

$$a_{SR} = \frac{9}{1600} \cdot \frac{e^4}{Q r_0^2}. \tag{2.38}$$

and B_w being proportional to $\int_S [\bar{W}(r)]^2 dS$.

Nuclear models based on the liquid-drop model and including additional shell and pairing corrections are still used today. These models are able to predict the masses of superheavy nuclides with uncertainties in the order of several hundred keV. For unknown nuclei they thus deliver very helpful information. However, the uncertainty of the mass measurements presented in this work are still out of reach for the most advanced theoretical calculations.

Predictions for nuclei in the region of heavy and superheavy elements obtained with macroscopic-microscopic approaches are discussed in Sec. 2.4. In Sec. 4.6 the results of FRLDM and FRDM are compared with results from microscopic theories and experimental data.

2.3 Microscopic models

Apart from the mass models discussed until now, which all are based on the macroscopic liquid-drop model, there exist also some purely microscopic approaches. The nucleus is regarded as a many body system composed of a certain number of neutrons and protons, each of them described with a single particle wave function ϕ_α. To obtain information on the binding energy or the single particle energy states of a certain nucleus, the Schrödinger equation

$$H(x_1, x_2, ..., x_A)\Psi_n(x_1, x_2, ..., x_A) = E_n\Psi_n(x_1, x_2, ..., x_A) \tag{2.39}$$

has to be solved. With increasing A this problem soon gets very complicated and in the case of superheavy nuclides it is far from being solved with the computational techniques which are available nowadays. One has thus to find suitable approximations to this ideal *ab initio* approach.[2] In the Hartree-Fock approximation, which is described in the beginning of this section (2.3.1), the interaction between the single particles is described by a mean-field. The binding energy can be found with the Ritz variation principle (sec. 2.3.2). As examples of microscopic mass models, which are used nowadays, the Hartree-Fock-Bogolyubov method and the Skyrme-Hartree-Fock BCS method are introduced in sec. 2.3.3.

2.3.1 The Hartree-Fock approximation

The basic idea behind the Hartree-Fock ansatz is to approximate the many-body interactions between the single particles with the help of an effective potential. The Hamiltonian

$$H = -\frac{\hbar^2}{2m}\sum_i \nabla_i^2 + \sum_{i,j} V_{i,j} + \sum_{i,j,k} V_{i,j,k} + ... \tag{2.40}$$

can thus be approximated as a Hamilton operator in an effective single particle potential:

$$H^{HF} = -\frac{\hbar^2}{2m}\sum_i \nabla_i^2 + \sum_i V_i^{HF}. \tag{2.41}$$

It is thus not longer necessary to take into account the interaction between the single particles but only the interaction between one single particle i and the mean field V_i^{HF} which is created by the other particles. Since the particles are now only interacting by the mean field they can be regarded to be independent.

The unknown total wave function $\Psi_n(x_1, x_2, ..., x_A)$ is written as the Slater determinant $\Phi_\alpha(x_1, x_2, ..., x_A)$ of the single particle wave functions $\phi_i(x_j)$, $i, j = 1, 2, ..., A$. The index α_i represents a complete set of quantum numbers of the state α_i. The Slater determinant is chosen as a wave function because it is fulfilling the constraint to be antisymmetric.

[2] For light nuclei ab initio approaches are still applicable. Since they are irrelevant for heavy nuclides they are not discussed in this thesis.

2.3.2 The Ritz variation principle

An approximated solution of this Schrödinger equation can be found with the help of the Ritz variation principle. It is one of the most important concepts in many-particle quantum mechanics and is making use of the principle of minimal energy. The wave function Φ is varied until a minimum energy for the ground state is obtained. The real energy of the ground state is always smaller than or equal to the ground state energy obtained by variations of the wave function:

$$E_0 = \langle \Psi | H | \Psi \rangle \leq \langle \Phi | H | \Phi \rangle = E_{Ritz}. \tag{2.42}$$

This method is also used in the Skyrme-Hartree-Fock method (see sec. 2.3.3).

2.3.3 The Hartree-Fock method with Skyrme interaction

The Hartree-Fock method with Skyrme interaction is a successful model for reproducing atomic masses on the basis of microscopic calculations. It is the basis of microscopic models that are still in use today, like for example the Hartree-Fock-Bogolyubov (HFB) model [Mang1975] and the Skyrme-Hartree-Fock BCS (SHF-BCS) model [Bend2003]. These models are based on the principle of the Hartree-Fock calculations, particularly with respect to the use of a mean-field as an effective potential. The binding energy can be obtained as a product of different energy functionals due to

$$E_B = E_{kin} + E_{Coul} + E_{Skyrme} + E_{pair} + E_{corr}. \tag{2.43}$$

The expressions E_x are so-called energy functionals which can be obtained by calculating the expectation value of the respective Hamiltonian:

$$\mathcal{E}_x = \langle \Psi | H_x | \Psi \rangle. \tag{2.44}$$

The relation between the energy functional E_x and the energy density functional $\mathcal{E}_x$ is given by:

$$E_x = \int \mathcal{E}_x(\mathbf{r}) d^3\mathbf{r}. \tag{2.45}$$

In the following the individual contributions to the total energy functional or the binding energy E_B, respectively, are shortly described.

Kinetic energy and Coulomb energy

The kinetic energy can be written as

$$E_{kin} \approx \frac{\hbar^2}{2m} \int \sum_q \tau_q(\mathbf{r}) d^3\mathbf{r}. \tag{2.46}$$

For reasons of simplification the proton and neutron masses are regarded to be equal and expressed by an average value $m = 938.919$ MeV/c^2. The quantity τ_q is the kinetic density. The parameter q stands for both types of nucleons, neutrons and protons, respectively.

The Coulomb energy is given by

$$E_{Coul} = \frac{e^2}{8\pi\epsilon} \int \frac{|\rho_p(\mathbf{r}, \mathbf{r}')|^2}{|\mathbf{r} - \mathbf{r}'|} d^3\mathbf{r} d^3\mathbf{r}', \tag{2.47}$$

with ρ_p being the proton density.

The Skyrme energy

In addition to these two fundamental energies a new energy based on the Skyrme force is introduced. It is named after T.H.R. Skyrme and has been successfully applied in fields of nuclear physics calculations [Vaut1972, Vaut1973]. The Skyrme force V_{Skyrme} is a simplified expression for the potential energy in Eq. (2.40) and consists of three terms:

$$V_{Skyrme} = V_{12} + V_{DD} + V_{LS}. \tag{2.48}$$

The first contribution is the two-body interaction which is given by

$$\begin{aligned} V_{12} &= t_0(1 + x_0 P_\sigma)\delta(\mathbf{r}_1 - \mathbf{r}_2) + \frac{t_1}{2}(1 + x_1 P_\sigma)\{\mathbf{k}^2, \delta(\mathbf{r}_1 - \mathbf{r}_2)\} + \\ &\quad t_2(1 + x_2 P_\sigma)\mathbf{k}\delta(\mathbf{r}_1 - \mathbf{r}_2)\mathbf{k}. \end{aligned} \tag{2.49}$$

P_σ is the spin-exchange operator, $\mathbf{k}$ is the relative momentum and ρ is the nucleon density. t_i and x_i are free parameters that have to be fitted to experimental data. For a better description of the short-ranged nuclear force the Skyrme force is assumed as zero-range interaction and expressed as a delta-function.

The three-body interaction can be reduced to a density-dependent two-body interaction, which is described by

$$V_{DD} = \frac{t_3}{6}(1 + x_3 P_\sigma)\rho^\alpha(\frac{\mathbf{r}_1 - \mathbf{r}_2}{2})\delta(\mathbf{r}_1 - \mathbf{r}_2). \tag{2.50}$$

The third term is taking into account relativistic corrections to the Hamiltonian. This so-called spin-orbit interaction is given by

$$V_{LS} = i\frac{t_4}{2}\{\delta(\mathbf{r}_1 - \mathbf{r}_2)\mathbf{k}, (\sigma_1 + \sigma_2) \times \mathbf{k}\}. \tag{2.51}$$

The energy functional E_{Skyrme} is obtained as expectation value of V_{Skyrme} and due to Eqs. (2.44) and (2.45):

$$E_{Skyrme} = \langle\Psi|V_{Skyrme}|\Psi\rangle = \int \mathcal{E}_{Skyrme}(\mathbf{r}) d^3\mathbf{r}. \tag{2.52}$$

$\mathcal{E}_{Skyrme} = \mathcal{E}_{12} + \mathcal{E}_{DD} + \mathcal{E}_{LS}$ is the Skyrme energy density functional. The three contributions are given by

$$\mathcal{E}_{12} = \frac{b_0}{2}\rho^2 - \frac{b_0'}{2}\sum_q \rho_q^2 + b_1[\rho\tau - \mathbf{j}^2] - b_1'[\rho_q\tau_q - \mathbf{j}_q^2] - b_2\rho\Delta\rho + b_2'\sum_q \rho_q\Delta\rho_q \tag{2.53}$$

$$\mathcal{E}_{DD} = \frac{b_3}{3}\rho^{\alpha+2} - \frac{b_3'}{3}\rho^\alpha \sum_q \rho_q^2 \tag{2.54}$$

$$\begin{aligned}\mathcal{E}_{LS} &= -b_4[\rho\boldsymbol{\nabla}\cdot\mathbf{J}+\boldsymbol{\sigma}\cdot(\boldsymbol{\nabla}\times\mathbf{j})]-b'_4\sum_q[\rho_q\boldsymbol{\nabla}\cdot\mathbf{J}_q+\boldsymbol{\sigma}_q\cdot(\boldsymbol{\nabla}\times\mathbf{j}_q)]- \\ & b_5[\mathbf{J}^2-\boldsymbol{\sigma}\cdot\boldsymbol{\tau}]+b'_5\sum[\mathbf{J}_q^2-\boldsymbol{\sigma}_q\cdot\boldsymbol{\tau}_q]. \end{aligned} \tag{2.55}$$

For the spin-orbit energy density $\mathcal{E}_{LS}$ also other parametrizations can be used as e.g. described in [Bend1998, Klüp2008]. The parameters b_i and b'_i are related to the previously used parameters t_i and x_i [Klüp2008]. The local densities and currents of the energy functional contain information about the single particle wave functions and are defined by

- **particle density**

$$\rho_q(\mathbf{r}) = \sum_{\alpha\in q} v_\alpha^2|\psi_\alpha(\mathbf{r})|^2 \tag{2.56}$$

- **kinetic density**

$$\tau_q(\mathbf{r}) = \sum_{\alpha\in q} v_\alpha^2|\boldsymbol{\nabla}\psi_\alpha(\mathbf{r})|^2 \tag{2.57}$$

- **spin density**

$$\boldsymbol{\sigma}_q(\mathbf{r}) = \sum_{\alpha\in q} v_\alpha^2\psi_\alpha^\dagger(\mathbf{r})\hat{\boldsymbol{\sigma}}\psi_\alpha(\mathbf{r}) \tag{2.58}$$

- **current** (momentum density)

$$\boldsymbol{j}_q(\mathbf{r}) = -\frac{i}{2}\sum_{\alpha\in q} v_\alpha^2\big\{\psi_\alpha^\dagger(\mathbf{r})\boldsymbol{\nabla}\psi_\alpha(\mathbf{r})-\boldsymbol{\nabla}\psi_\alpha^\dagger(\mathbf{r})\psi_\alpha(\mathbf{r})\big\} \tag{2.59}$$

- **spin-orbit density**.

$$\boldsymbol{J}_q(\mathbf{r}) = -i\sum_{\alpha\in q} v_\alpha^2\psi_\alpha^\dagger(\mathbf{r})\boldsymbol{\nabla}\times\hat{\boldsymbol{\sigma}}\psi_\alpha(\mathbf{r}) \tag{2.60}$$

- **kinetic spin density**

$$\boldsymbol{\tau}_q(\mathbf{r}) = \sum_{\alpha\in q} v_\alpha^2\big[\boldsymbol{\nabla}\psi_\alpha^\dagger(\mathbf{r})\big]\cdot\boldsymbol{\nabla}\big[\hat{\boldsymbol{\sigma}}\psi_\alpha(\mathbf{r})\big] \tag{2.61}$$

ψ_α are the single particle wave functions and v_α^2 is the occupation probability of the state α. The occupation probability v_α^2 is a result of including a residual two-body interaction (see section "Pairing energy") and can take values in the interval $[0,1]$. For the case of pure Hartree-Fock the occupation probability v_α^2 is 0 for all particles below zero and above the Fermi energy.

Pairing energy

The previous terms are based on the assumption that the single nucleons are independent particles and do not interact with each other. For a more realistic description the formation of nucleon pairs (proton-proton pairs and neutron-neutron pairs) has to be taken into account. Thus a pairing force which is creating a short-ranged pairing field is introduced (for details see e.g. [Ring1980, Bend2003]). The pairing energy density functional is given by

$$\mathcal{E}_{pair} = \frac{1}{4}\sum_{q}\int V_{pair,q}(\mathbf{r})\chi_q^2(\mathbf{r})d^3\mathbf{r}, \tag{2.62}$$

where $V_{pair,q}$ is the pairing strength. The local pair density χ_q is defined by

$$\chi_q = -\sum_{\alpha\in q} u_\alpha v_\alpha |\psi_\alpha(\mathbf{r})|^2, \tag{2.63}$$

and is also a function of the occupation amplitude v_α. Additionally it contains the non-occupation amplitude u_α which is connected with v_α by $u_\alpha = \sqrt{1-v_\alpha^2}$.

Corrections

Apart from the upper four terms which are contributing to the energy functional some corrections have to be included. One example is the center-of-mass correction, which is an approximate projection onto an ideal center-of-mass momentum. This is necessary because the mean field description violates the translational invariance. The center-of-mass correction can be written as

$$\mathcal{E}_{CM} = \frac{\hbar^2}{2m}\langle\hat{P}_{cm}\rangle. \tag{2.64}$$

Determination of the binding energy

The determination of the binding energy is performed according to the Ritz variation principle. The optimum Hamiltonian is found by varying the energy functional E_B, or the energy density functional $\mathcal{E}$, respectively, for the different densities $J_{i,q}$:

$$\hat{h}_q(\mathbf{r}) = \sum_{J_{i,q}}\int d^3\mathbf{r}'\frac{\delta\mathcal{E}}{\delta J_{i,q}(\mathbf{r}')}\left[\delta(\mathbf{r}-\mathbf{r}')\hat{J}_{i,q}(\mathbf{r}')\right]. \tag{2.65}$$

$J_{i,q}$ represents the particle density ρ_q, the kinetic density τ_q, the spin density σ_q, the current density j_q, the spin-orbit current J_q, and the kinetic spin density $\mathbf{t}_q$ (see Eq. (2.56)-(2.61)). The optimum value is found if E_B is minimal: $\delta E_B = 0$. This energy minimum is determined by varying the energy functional with respect to the single particle wave functions and with respect to the occupation probabilities.

The variation principles due to HFB is done according to the two HFB equations [Bend1998]

$$\int dx'\left[\left(\hat{h}_q(\boldsymbol{r}',\boldsymbol{r})-\lambda\delta(\boldsymbol{r}'-\boldsymbol{r})\right)v_\alpha^2-\frac{1}{2}u_\alpha v_\alpha\Delta(\boldsymbol{r}',\boldsymbol{r})\right]\psi_\alpha(\boldsymbol{r}') = \sum_i \lambda_{i\alpha}\psi_i(\boldsymbol{r}) \tag{2.66}$$

and

$$2(h_{\alpha\alpha} - \lambda)u_\alpha v_\alpha = \Delta_{\alpha\bar{\alpha}}(u_\alpha^2 - v_\alpha^2), \tag{2.67}$$

where the Lagrange multiplier λ can be interpreted as the Fermi energy. The quantity

$$h_{\alpha\alpha} = \int\int d^3\boldsymbol{r}d^3\boldsymbol{r}'\psi_\alpha^\dagger(\boldsymbol{r}')\hat{h}_q(\boldsymbol{r}',\boldsymbol{r})\psi_\alpha(\boldsymbol{r}) \tag{2.68}$$

is the matrix element of the single particle hamiltonian and

$$\Delta_{\alpha\bar{\alpha}} = \int\int d^3\boldsymbol{r}d^3\boldsymbol{r}'\psi_\alpha^\dagger(\boldsymbol{r}')\Delta(\boldsymbol{r}',\boldsymbol{r})\psi_\alpha(\boldsymbol{r}) \tag{2.69}$$

is the matrix element of the pairing potential $\Delta(\boldsymbol{r}',\boldsymbol{r})$. The wave functions and the occupation probabilities v_α^2 are varied at the same time. The HFB equations are directly related to the pairing interaction. The solution is in this case very complex and not discussed here. The most advanced version of the HFB model is the HFB-17 [Gori2009], which is providing data that are very close to the experimental results (see Sec. 4.6).

Another possibility is the SHF-BCS ansatz. Here, the feedback of the occupation probabilities v_α on the mean-field is neglected. The HFB equations (2.66) and (2.67) are then simplified and the SHF-BCS equations are obtained:

$$\hat{h}_q\psi_\alpha = \epsilon_\alpha\psi_\alpha \tag{2.70}$$

$$2(\epsilon_\alpha - \lambda)u_\alpha v_\alpha = \Delta_\alpha(u_\alpha^2 - v_\alpha^2) \tag{2.71}$$

where Δ_α is a state dependent gap, which is given by

$$\Delta_\alpha = \int d^3\mathbf{r}\psi_\alpha^\dagger(\mathbf{r})\Delta(\mathbf{r})\psi_\alpha(\mathbf{r}). \tag{2.72}$$

Iteratively solving the two SHF-BCS equations one gets the single particle wave functions ψ_α, the single particle energies ϵ_α, the occupation probabilities v_α^2, and the Fermi energy λ. By using the pairing ansatz also energy levels above the Fermi energies $\epsilon_{F,p}$ (for protons) and $\epsilon_{F,n}$ (for neutrons) are included.

Determining binding energy for fixed quadrupole deformation

Another important point is the deformation of the nucleus, which is taken into account by including an additional quadrupole operator $\hat{Q}_{20}$ into the Schrödinger equation:

$$(\hat{H}_\alpha - \lambda\hat{Q}_{20})|\Phi_{\alpha 20}\rangle = \epsilon_\alpha|\Phi_{\alpha 20}\rangle. \tag{2.73}$$

$\hat{H}_\alpha$ represents the Hamiltonian of the total wave function which contains all contributions of the energy functional. This Hamiltonian is now modified to the "deformed" Hamiltonian $\hat{H}_{\alpha,def} = \hat{H}_\alpha - \lambda\hat{Q}_{20}$.

Without formally including this quadrupole operator into the Schrödinger equation the iteration will automatically end at a deformation which leads to the global minimum of the binding energy. With the new formalism it is possible to fix the deformation - in this case only quadrupole deformation - to a certain value and

calculate the corresponding binding energy. The binding energy of the nucleus as a function of the deformation provides important information about the half-life of the nucleus.

Many microscopic mass models which are still used today are based on mean-field approaches. The example chosen in this section is the approach of [Bend2003]. Another example for a microscopic model is the Hartree-Fock-Bogolyubov (HFB) method [Mang1975]. This method has been constantly developed further and recently advanced to version HBF-17 [Gori2009]. Like the approach described above it is also using the Skyrme force to achieve a suitable approach for the nucleon-nucleon interaction. The results of both models for some isotopes in the heavy and superheavy region are compared with results from macroscopic-microscopic approaches and experimental values in Sec. 4.6.

2.4 Predictions of the mass models for superheavy nuclei

The nuclear masses derived from the recent models are not very precise compared with experimental results (predictions of different models are shown in Tab. 4.16). They are, however, of importance for the understanding of the existence of superheavy elements and especially of utmost importance for the prediction of the location of the "island of stability". Nuclear mass models cannot only be used for the determination of the mass. From the behaviour of the binding energy of a nucleus as a function of the deformation one can also obtain information about the fission barrier and thus about the half-life.

According to early calculations based on the liquid drop model (see Sec. 2.1) the existence of heavy nuclides was limited by the instability with respect to spontaneous fission [Bohr1939, Fren1937]. The stability of the nucleus is in this case dominated by the contributions of the surface energy and the Coulomb energy (see Fig. 2.2). With increased deformation the reduced Coulomb repulsion leads to a lower energy, the surface energy is however increased. The sum of both contributions leads to instability for high deformation. The height of the sum potential maximum is called liquid drop fission barrier B_f. It defines the scission point at which the drop disrupts into two fragments. For deformations smaller than the scission point the nucleus is kept together by a backdriving force. Deformations above the scission point lead to a disruptive force which results in the decay of the nucleus.

Based on the constraint that the fission barrier B_f has to be larger than zero one can derive a limit for the stability of a nucleus. The disappearance of the fission barrier was predicted for nuclei with $Z^2/A > 39$.[3] Configurations for heavy nuclides with $Z^2/A > 39$ are only theoretically understood when shell corrections are included (see Fig. 2.3). By including shell effects (see Sec. 2.2) into the calculation one can find more stable configurations even for heavy nuclides. Especially in the region of nuclides with $Z \approx 100$ the stability is due to theory mainly caused by shell effects, which are resulting in a deformation of the nucleus. These shell effects rearrange the

[3] This value is dependent on the parametrization and varies between 35 and 45.

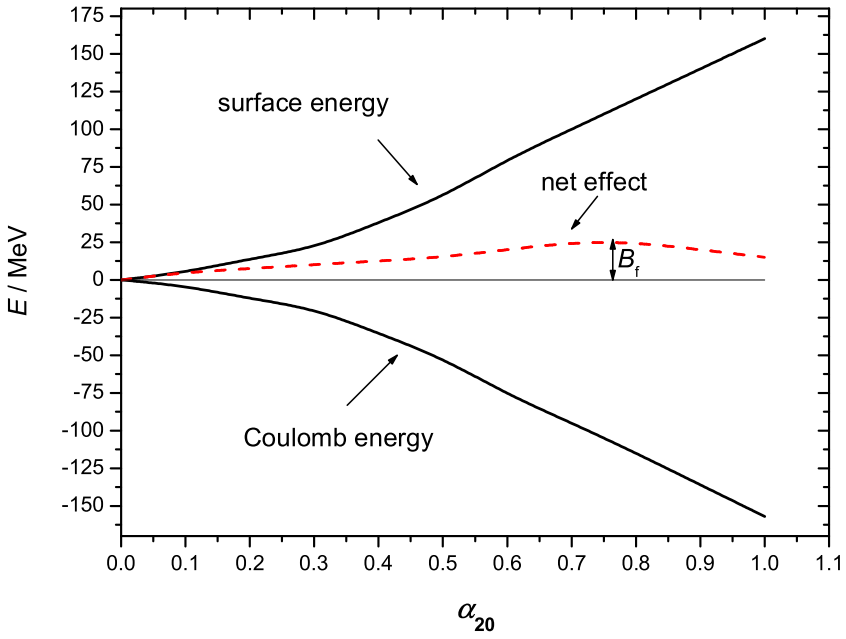

Figure 2.2: Sketch for the illustration of the fission barrier in the liquid drop model. The binding energy of the nucleus is plotted as a function of the quadrupole deformation α_{20}. The contributions of the surface and the Coulomb energy are plotted as solid black lines. The sum energy is plotted as dashed red line. The fission barrier B_f is defined as the maximum height of the sum potential. It defines the scission point.

shell structure and lead to deformation, which causes the magic numbers based on calculations for spherical nuclei to be not longer relevant. Due to deformation new magic numbers, representing so-called deformed shell closures, can be found. For the protons a deformed shell-closure is then reached for $Z = 100$, which is in the vicinity of the nobelium masses studied within this thesis. For the neutrons the neutron number $N = 152$ is found to be a shell closure.[4] Comparatively long half-lives in the region of nobelium support the theoretical results. The next deformed shell closure is predicted at $Z = 108$ (which corresponds to the element hassium) and $N = 162$ [Paty1991, Möll1992, Möll1994].

Figure 2.4 shows the binding energy of the nuclide ^{254}No as a function of the quadrupole deformation based on calculations with the Skyrme-Hartree-Fock method [Erle2009]. For a spherical shape of the nucleus ($\alpha_{20} = 0$) a maximum in binding energy[5] can be observed. The nucleus will thus - according to this model calculation - try to adopt another (non-spherical) shape to minimize its energy. The minimum is in this case found for $\alpha_{20} \approx 0.3$, which describes a prolate nuclear shape. Also

[4] For this reason the nuclide ^{254}No could to some extent be regarded to be analogue to a semi-magic nucleus.

[5] Note that the binding energy is defined due to Eq. (2.2) as negative quantity.

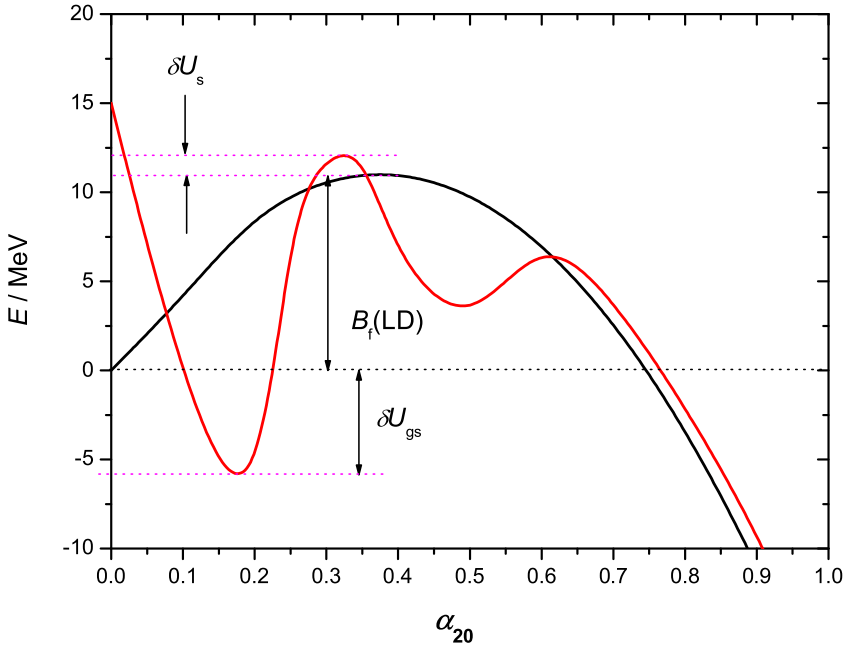

Figure 2.3: Sketch for the comparison of the sum of surface and Coulomb energy for the liquid drop model (solid black line) and the macroscopic-microscopic model (solid red line). The binding energy of the nucleus is plotted as a function of the quadrupole deformation α_{20}. After including shell corrections a stable energy minimum can be obtained for deformations larger than zero. The shell effect at the ground state δU_{gs}, the shell effect at the saddle point δU_s and the fission barrier B_f due to the liquid drop model are marked.

oblate shapes (described by $\alpha_{20} < 0$) are for the ^{254}No nucleus more favorable than the spherical shape. The nucleus in the potential minimum performs oscillations around the optimum shape. The magnitude of these oscillations is determined by the ground state energy, which is represented by the red line. In Fig. 2.4 it is also visible that the energy minimum at $\alpha_{20} \approx 0.3$ is only a local minimum. For higher deformations even smaller energies can be obtained. A transition of the nucleus to these high deformations would result in a decay of the nucleus by spontaneous fission. The half-life of the nucleus due to spontaneous fission is determined by the thickness and the height of the potential barrier.

One can conclude from the theoretical calculations that the stability of the considered nobelium isotopes $^{252-254}$No is mainly caused by deformation, which is resulting from the rearranged shell structure. The potential barrier is in all cases high enough to suppress spontaneous fission and thus make α decay more favorable.

Also for higher Z nuclides stable configurations are found if deformation is taken into account. Figure 2.5 shows the potential barrier of the darmstadtium isotope ^{270}Ds. Also here the minimum of the binding energy is not obtained for a spherical

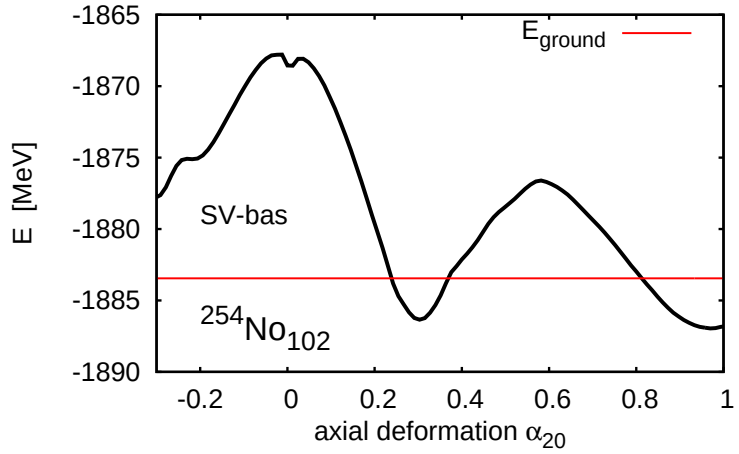

Figure 2.4: The binding energy of ^{254}No as a function of the deformation parameter α_{20} calculated with the Skyrme-Hartree-Fock BCS method (SV-bas parametrization). The red line represents the ground state energy (courtesy of Jochen Erler, University of Erlangen).

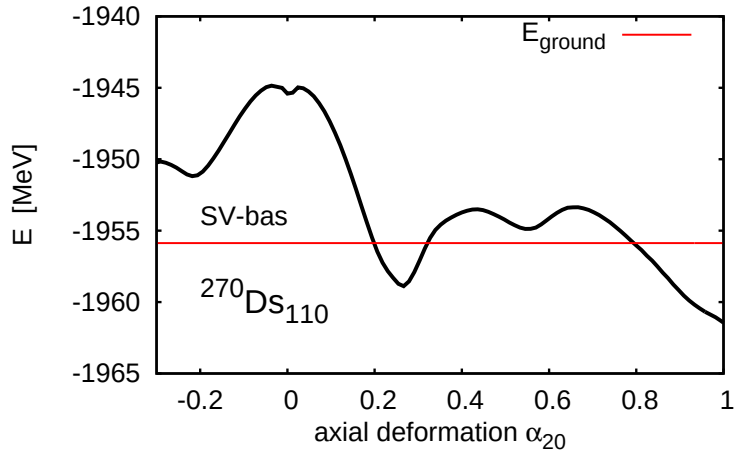

Figure 2.5: The binding energy of ^{270}Ds as a function of the deformation parameter α_{20} calculated with the Skyrme-Hartree-Fock BCS method (SV-bas parametrization). The red line represents the ground state energy (courtesy of Jochen Erler, University of Erlangen).

shape but for a prolate one. The next shell closures are expected to be at $Z \approx 120$ and $N = 184$ according to microscopic calculations [Cwio2005, Bend1999, Bend2001, Bend2003] and at $Z \approx 114$ and $N = 184$ according to macroscopic-microscopic calculations [Möll1994, Smol1995]. These nuclides are expected to have spherical shapes again. Figure 2.6 shows the deformation for heavy and superheavy nuclides due to calculations with the FRDM (see Sec. 2.2.4). Spherical shell closures are

expected for Z=82, 114 and N=126, 184. The region of highly deformed nuclides is between Z=90 to 110 and N=140 to 165.

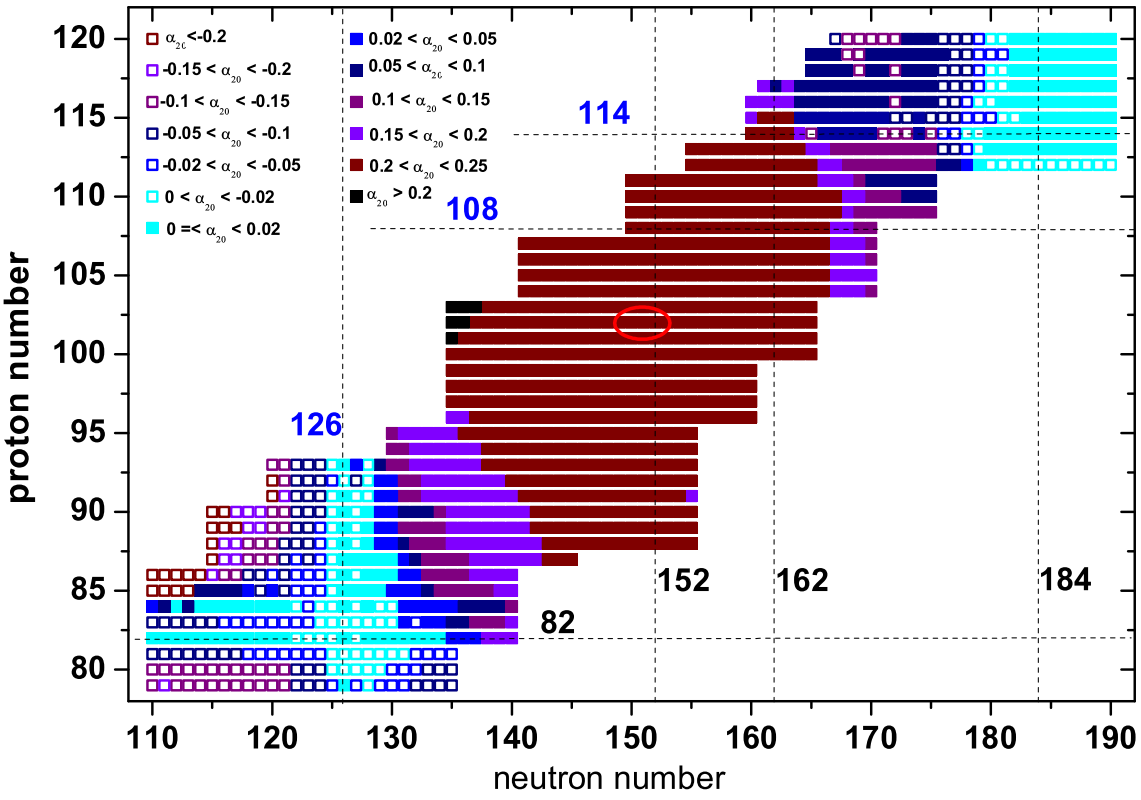

Figure 2.6: The nuclear deformation in the region of heavy and superheavy nuclides is illustrated. The results are taken from [Möll1995]. α_{20} is the quadrupole deformation. $\alpha_{20} > 0$ describes prolate, $\alpha_{20} < 0$ oblate and $\alpha_{20} = 0$ spherical shapes. The nobelium nuclides presented in this work are marked with a red circle.

Since the shell effects are of high importance in the region of the heavy elements, the consistency of the results of a theoretical model with the experimental data yield important information about the predictive power of this model. The masses in the region of nobelium are at present already known with comparatively small uncertainties, but none of them has been measured directly. The first direct mass measurements on transuranium elements have been carried out in this work. They provide an important independent confirmation of the previously only indirectly obtained mass values. Like this the determination of the mass is also possible if the detailed structure of the level scheme is unknown. Furthermore direct mass measurements provide accurate input data for new theoretical calculations.

3 The high-precision Penning trap mass spectrometer SHIPTRAP

SHIPTRAP is a high-precision mass spectrometer which was built to perform direct mass measurements on heavy and superheavy elements. It is installed behind the velocity filter SHIP (Sec. 3.1) where nuclei are produced by fusion evaporation reactions and separated from the primary beam. The reaction products are then stopped in a gas cell (Sec. 3.2) and extracted to an RFQ cooler and buncher (Sec. 3.4), where they are accumulated and ejected as short bunches. The ions are then transported to a double Penning trap system (Sec. 3.4) where the mass measurement takes place. For the detection of the ions a set of silicon and MCP detectors (Sec. 3.5) is used. This chapter will describe the different parts of the SHIPTRAP setup (see Fig. 3.1) and its operation.

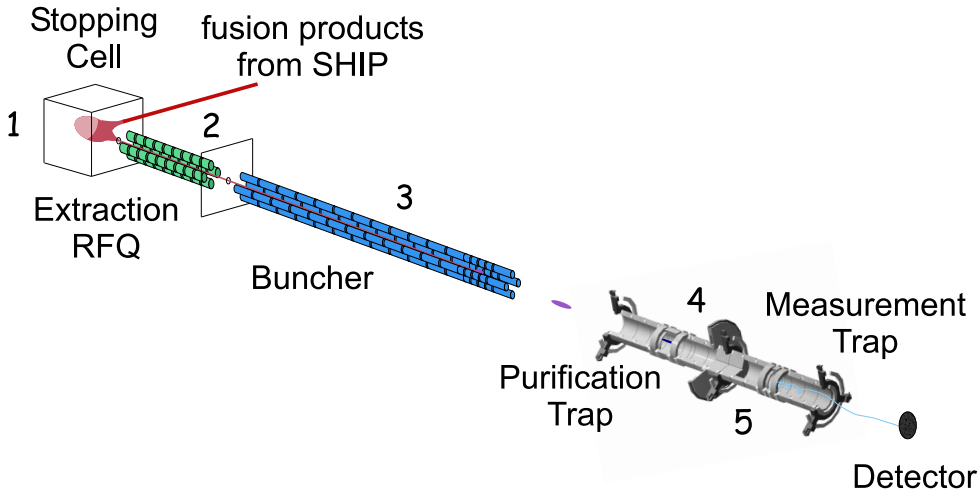

Figure 3.1: An overview over the SHIPTRAP setup is given. The individual parts are the gas cell (1), the extraction RFQ (2), the RFQ buncher (3), the purification trap (4) and the measurement trap (5). Details are given in the text.

3.1 The velocity filter SHIP

The velocity filter SHIP (Separator for Heavy Ion reaction Products) was designed to obtain a rapid and efficient separation of the reaction products from fusion-evaporation reactions [Münz1979, Hofm2000]. The primary beam for these experiments is typically produced in a 14-GHz-ECR (electron cyclotron resonance) ion source of the CAPRICE (Compacte A Plusieurs Résonances Ionisantes Cyclotron)

type [Gell1992], which can deliver all kinds of ions up to uranium, and then injected into the UNILAC (UNIversal Linear ACcelerator), where it is accelerated to Coulomb barrier energies on the order of 4 to 5 MeV/u. Typical beam intensities are about 1 $\mu A_{particle}$.

The reaction products are produced in cold-fusion reactions by reacting the ions from UNILAC in the mass range of $A = 40$ to 80 with a rotating target of, for example, lead or bismuth mounted on a wheel. The beam is delivered in pulses of 5.5 ms length with a repetition rate of 50 Hz. The target thickness is typically about 0.5 mg/cm^2. The wheel rotates with a frequency of 1125 turns per minute.

The fusion products are separated from the primary beam using a double Wien filter [Münz1979] consisting of a combination of electric and magnetic fields which are perpendicular to each other and to the beam axis. The net force on an ion is given by the relation

$$m\vec{a} = q(\vec{E} + \vec{v} \times \vec{B}). \tag{3.1}$$

Evidently for

$$|\vec{v}| = \frac{|\vec{E}|}{|\vec{B}|} \tag{3.2}$$

the force is zero for all charge states q. The reaction products are thus separated according to their velocity $|\vec{v}|$ regardless their charge state q.

The fusion products are produced with energies of a few 100 keV/u, which is significantly different from the primary beam particles. The background by the primary beam in the focal plane is typically in the order of 1 Hz.

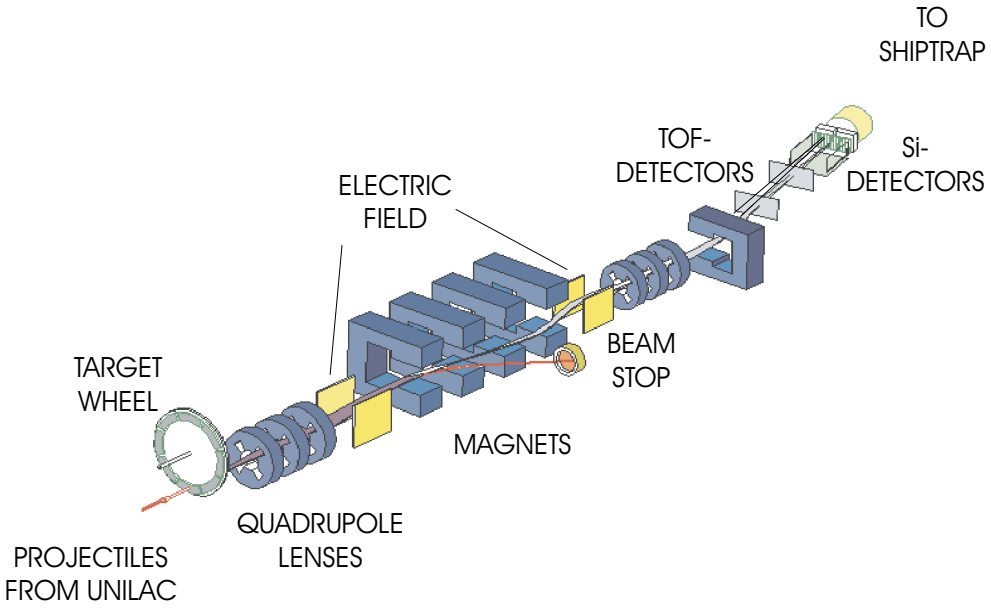

Figure 3.2: A sketch of the velocity filter SHIP. The beam from the UNILAC first hits a target wheel and is then directed to the beam stop. The reaction products are separated due to their velocity by a special combination of electric and magnetic fields.

For a rough mass identification a time-of-flight detector can be used to reduce background from unwanted products and scattered projectiles in the detector. Individual nuclei are identified by the determination of correlated α decays in a position sensitive Si detector, which has an energy resolution of 20 to 25 keV. In addition, germanium detectors are used to measure x-rays or γ-rays, which are correlated with events from the Si detector in a time window of 4 μs. This allows identifying a nuclide due to gamma radiation from the decays of characteristic energy levels in the daughter nucleus.

Passing the target foil results in an energy spread of the particles in the order of 10% to 30%. The energy loss is determined by the place of production within the target foil.

The ions produced at SHIP can be transported to the SHIPTRAP Penning trap system to perform high-precision mass measurements. Therefore it is necessary to replace the Si detector of the SHIP experiment mentioned above by a beamline which guides the ions to a gas stopping cell. The SHIPTRAP setup consists of three main parts: A gas cell, an RF buncher and the Penning traps. In the following these three parts are explained.

3.2 The gas cell

The nuclei coming from SHIP at an energy of a few ten MeV are stopped in a gas cell (see Fig. 3.3), which is filled with high-purity He gas at a pressure of typically 50 mbar [Neum2006]. An entrance window with a thickness of about 2 mg/cm^2 and an open diameter of 60 mm separates the gas cell from the transfer line vacuum. Al, Ti or Ni are normally chosen as window materials. This window acts as a degrader. In an ideal case the window foil thickness is chosen such that the high energetic reaction products are decelerated and stopped in the center of the extraction region defined by the electrode cage (see Fig. 3.3). The energy loss and the corresponding range can be calculated using the TRIM code [TRIM] for example.[1] However, in practise the thickness cannot be calculated with sufficient accuracy. Due to the energy spread of the beam and the range straggling experimentally fine tuning is needed. For this reason an additional set of mylar degraders is installed in the transfer line in front of the gas cell. The degrader foils are mounted on a movable feedthrough and can be exchanged in a simple way. This makes it possible to optimize the proper degrader thickness for each nuclide during an experiment.

Inside the gas cell an electrode system consisting of a DC voltage cage and a funnel are mounted. In this way an electric field along the extraction axis is generated to drag the ions towards the exit nozzle. The cage consists of a set of five ring electrodes with a diameter of $d = 131$ mm where a DC voltage gradient - normally starting at about 200 V and decreasing to about 100 V - is applied. The funnel is made of 40 concentric ring electrodes, which decrease linearly in diameter starting from $d = 131$ mm behind the DC voltage cage to $d = 5$ mm in front of the nozzle. The funnel

[1] This program only allows calculations for ions until $Z = 92$. For heavier elements the energy loss has to be extrapolated. Furthermore the program assumes an ideal homogeneity of the foil, which is not given in reality.

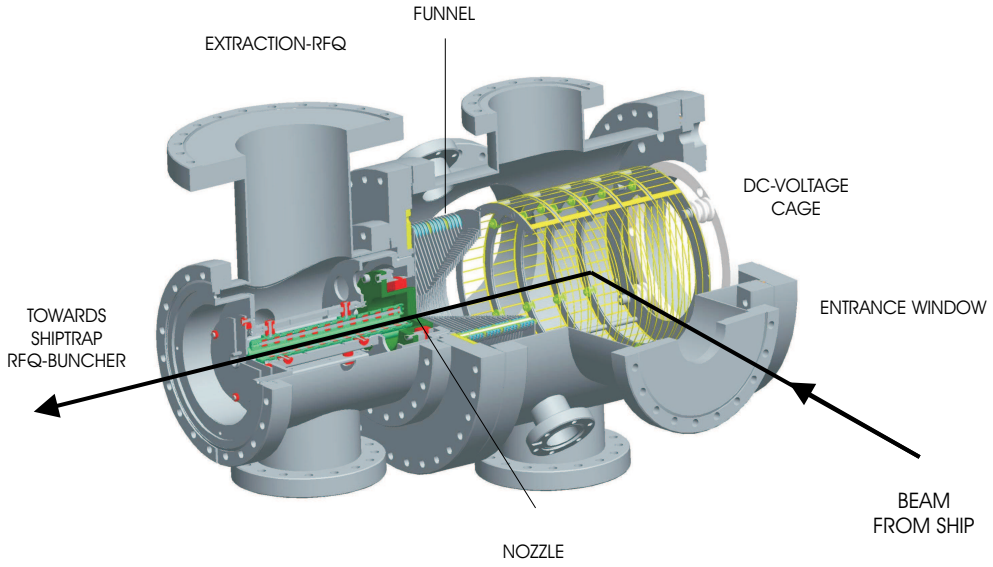

Figure 3.3: A sketch of the SHIPTRAP gas cell. The total length is about 60 cm. The arrow is symbolizing the trajectory of the ions which are coming from SHIP. Further details are given in the text.

electrodes have a thickness of 1 mm and are mounted in a distance of 1 mm to each other. At the funnel a DC gradient from 30 V to 20 V is applied to move the ions into the direction of the nozzle ($U_{nozzle} \approx 19$ V) which has a diameter of 0.6 mm. At the funnel an additional RF (radio-frequency) provides a repulsive force to avoid losses while the ions are focussed onto the nozzle.

High DC gradients are favorable to obtain high efficiencies, since they provide for a fast extraction from the gas cell. For typical gradients on the order of 10 V/cm the ions are extracted within a few ms to prevent molecule formation and recombination of ions and electrons. For the same reason a very high purity on the ppb level of the He buffer gas is crucial. To achieve this the helium gas[2] is purified using a zeolith-filter immersed in liquid nitrogen. The gas cell is constructed in accordance with UHV standards and baked to about 120°C before each experiment. After two days or more of baking a residual gas pressure of better than 10^{-9} mbar can be reached in the cell.

Arriving at the nozzle the ions are extracted from the gas cell by the helium gas flow. The angle between the directions of injection and extraction of the ion beam is 90°. The voltage difference between the last segment of the funnel and the nozzle is very sensitive and has therefore to be optimized very carefully. The nozzle voltage has a direct influence on the drift velocity of the ions, which has to be the same as the drift velocity of the helium gas.

After passing the nozzle the ions are transported by an RFQ structure which consists of four parallel cylindrical rods, each of 18 cm length. To apply the proper DC gradient each of the rods is in beam direction 12 times segmented. In this way the ions are transported to the RFQ buncher. The time the ions need to pass the extraction RFQ is in order of 1 ms. The RF settings of the funnel and the two RFQ

[2]Usually He 6.0 is used, which has a purity of 99.9999%

Table 3.1: The amplitudes and frequencies of the RF excitations in the funnel, the extraction RFQ structure and the buncher are shown for an A/q ratio of about 130.

	funnel	extraction RFQ	buncher
amplitude / V_{pp}	200	350	100
frequency / kHz	850	1000	720

structures are shown in Tab. 3.1. A turbo molecular pump with 1000 l/s pumping speed (for N_2) is mounted to the vacuum chamber in which the extraction RFQ structure is placed to pump away the helium gas from the gas cell. The pressure in the extraction RFQ region is about 10^{-2} mbar.

The total efficiency of the gas cell is defined by the number of ions leaving the gas cell via the extraction RFQ structure divided by the number of ions entering the window foil. It can be written as

$$\epsilon_{GC} = \epsilon_{stop} \cdot \epsilon_{extr}, \tag{3.3}$$

where ϵ_{stop} is the stopping and ϵ_{extr} the extraction efficiency. ϵ_{stop} could not be determined directly in an experiment. The value obtained from simulations is about 40% for low pressures (50 mbar and smaller) and 75% for high pressures (90 mbar and higher). ϵ_{extr} was determined to be between 15% (for high pressures) and 30% (for low pressures) by using a calibrated ^{223}Ra ion source [Elis2007]. The total efficiency ϵ_{GC} was also determined experimentally to be around 12% [Neum2006, Elis2007]. The value for ϵ_{stop} deduced from these two experimental values is thus in agreement with the value determined from simulations.

3.3 The RFQ buncher

The ions which are extracted from the gas cell are transported to an RFQ cooler and buncher [Rodr2003]. Here the ions are further cooled and short bunches are created.

The RFQ cooler and buncher consists of four cylindrical electrode rods with a length of about one meter. Each rod is axially segmented into 34 parts to apply a DC voltage (see Fig. 3.4). The voltages applied to the different segments of the buncher start with +2 V at the first segment after the injection and decrease slowly to a minimum at the 33$^{\text{rd}}$ segment of about -12 V. The last segment is connected to a voltage switch, which can change the voltage between two values (see Fig. 3.4). If the default value of +2 V is applied the buncher is closed. After the accumulation the voltage of segment 34 is switched to -80V, which is represented by the dashed line in Fig. 3.4. Additionally the 31$^{\text{st}}$ segment is switched to +50 V to achieve narrow bunches of about 500 ns width.

In addition to the static DC potential, which confines the ions in axial direction, the radial confinement in the RFQ is provided by an RF field that is applied to

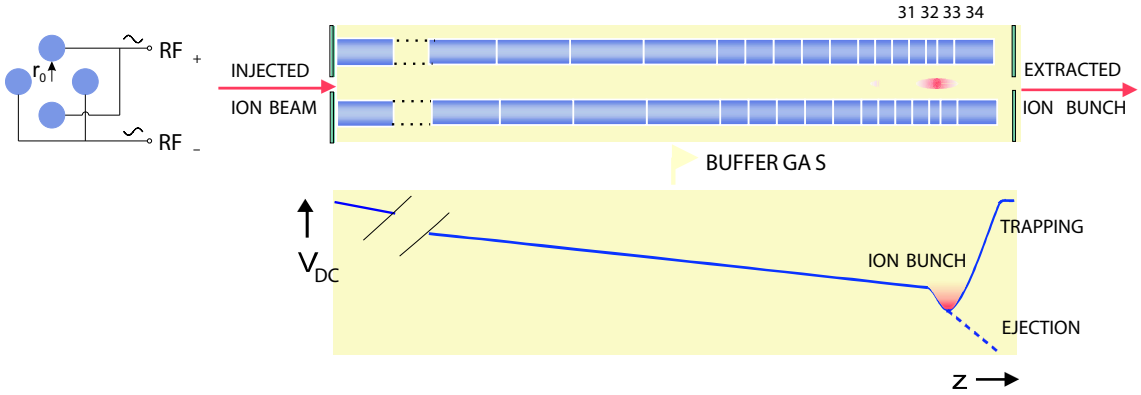

Figure 3.4: A sketch of the RFQ buncher (top) and the axial potential profile (bottom). The buncher consists of four cylindrical electrodes which are segmented to create the proper potential.

diagonally opposing rods. The sum potential can thus be expressed in the following way:

$$\Phi(t) = U_0 + U_{RF} \cdot \cos \omega_{RF} t, \tag{3.4}$$

with U_0 and U_{RF} being the DC and RF voltages applied to the buncher electrodes and ω_{RF} the frequency of the quadrupolar driving field. The stability of the ion motion for a given m/q is determined by the q value, which is given by the formula [Daws1995]

$$q = \frac{2eU_{RF}}{mr_0^2\omega_{RF}^2}, \tag{3.5}$$

where e is the elementary charge, m the mass of the ions and r_0 the distance between the center of the buncher and one electrode[3]. The q value is normally chosen to be around 0.4 in order to obtain stable confinement.

The ions entering the RFQ buncher from the gas cell lose kinetic energy in collisions with helium gas atoms at a pressure of about $5 \cdot 10^{-3}$ mbar and are accumulated in the potential minimum (segment 33). The cooling time is about 3 ms [Rodr2003]. After a typical buncher storage time of 1-2 s, which is determined by the length of the measurement cycle, the ions are ejected in ion bunches with a bunch width of about 500 ns [Wern2008].

In the buncher it is also possible to remove unwanted ions by mass-selective cleaning. This can be done by a dipolar excitation at the ions' secular frequency applied to segment 32. A mass resolving power of about 50 can be obtained [Rodr2003].

3.4 The Penning traps

After the ions are ejected from the buncher they are directed by several einzel lenses and deflectors to a double Penning trap system (see Fig. 3.5), which is placed in a 7-T super-conducting magnet. The first Penning trap is called preparation trap (PT). Here, a mass-selective buffer gas cooling is performed (see Sec. 3.4.4) [Sava1991].

[3]The electrodes are mounted symmetric around the center of the buncher, see Fig. 3.4

In the second Penning trap, the measurement trap (MT), the mass measurement takes place (see Sec. 3.4.5). This chapter first describes the theoretical basics of a Penning trap in general (see Sec. 3.4.1) and then shortly summarizes possible sources of imperfections (see Sec. 3.4.2). Then different excitations which are necessary for the preparation of the ions and the frequency determination are discussed (see Sec. 3.4.3).

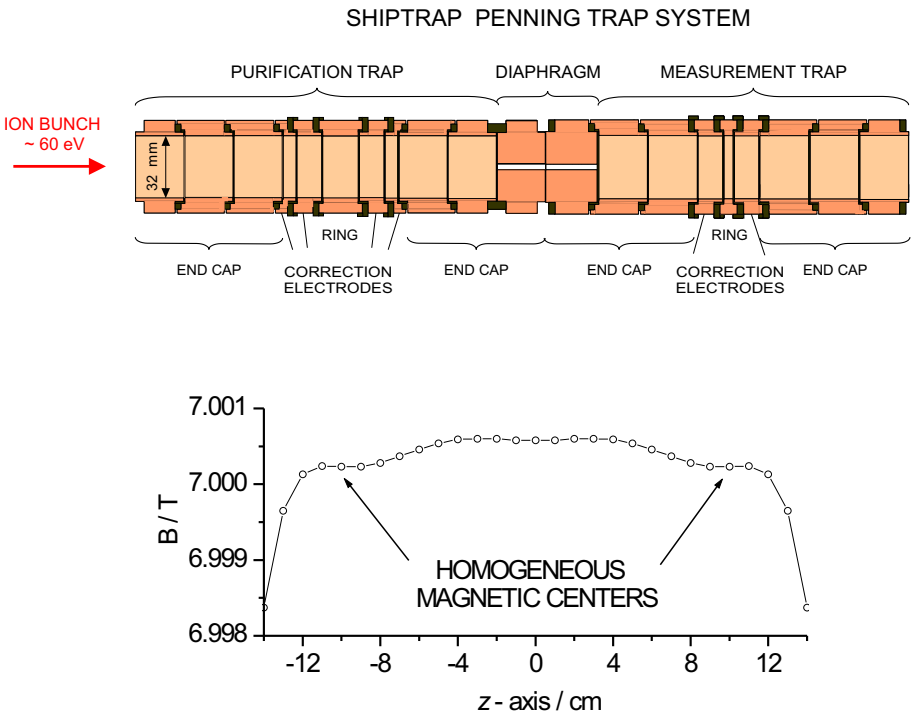

Figure 3.5: The Penning trap system at SHIPTRAP is shown. The ions are first captured in the preparation trap (PT) were a mass selective buffer gas cooling (see Sec. 3.4.4) can be performed. The isobarically cleaned ions are then transferred to the measurement trap (MT) via a diaphragm with a diameter of 1 mm. Here the frequency determination (see Sec. 3.4.5) is taking place.

3.4.1 Principle of a Penning trap

A Penning trap is an ideal tool to confine charged particles in three dimensions and to perform measurements on them. One application - which is described in this work - is the determination of the stored particles' mass by measuring their cyclotron frequency with the time-of-flight resonance method (see Sec. 3.4.5) [Gräf1980]. This chapter explains the principle of a Penning trap and the possibility to manipulate the ions within by applying excitation and cooling mechanisms. These mechanisms are necessary to prepare the ions for the frequency determination in a proper way.

The theory of a Penning trap is described on the basis of the ideal Penning trap. Deviations from this ideal case due to inhomogeneities of the electric and magnetic field or due to coulomb interactions of several ions stored in the trap at the same time are discussed separately (see Sec. 3.4.2).

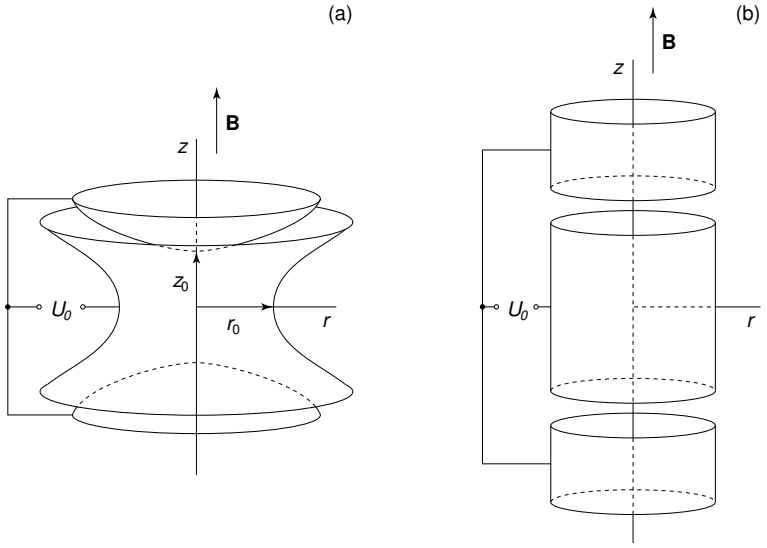

Figure 3.6: The assemblies of two different types of Penning traps are shown: The hyperbolical trap (a) and the cylindrical trap (b). The ions are injected parallel to the magnetic field. To capture the ions the DC voltage U_0 is applied between the ring electrode and the upper and lower end cap.

A charged particle with the charge-to-mass ratio q/m and the velocity $\vec{v}$ is deflected in a magnetic field $\vec{B}$ due to the Lorentz force $\vec{F_L} = q\vec{v} \times \vec{B}$ if it has a velocity component perpendicular to the magnetic field. The motion of this particle is in the general case a spiral. As a projection to the plane perpendicular to the magnetic field we obtain a circular motion with the frequency

$$\omega_c = 2\pi\nu_c = \frac{q}{m} \cdot B. \tag{3.6}$$

This equation is obtained by equating the expressions for the Lorentz force and the centrifugal force. Applying a magnetic field only allows the storage of the ions in two dimensions. For a three dimensional storage a weak electric quadrupolar field is added to the strong magnetic field. A detailed description of this so-called Penning trap configuration - named after F.M. Penning - can be found in [Brow1986]. Figure 3.6 shows the two principal configurations of a Penning trap. In general a Penning trap consists of a ring electrode with an inner diameter of $2r_0$ and two end caps with a distance z_0 to the trap center each. In the case of the hyperbolical trap (Fig. 3.6(a)) the electrodes are approaching the shape of the equipotential surfaces. In the case of the cylindrical trap both end caps and ring electrodes have cylindrical shape. To come close the ideal harmonic potential it is here necessary to extend the trap by additional so-called *correction electrodes* (see Fig. 3.5) where the proper correction voltages have to be applied. The z-axis is chosen in the direction of the magnetic field, which should also be the common axis of rotation of the electrodes (trap axis). The origin $(x, y, z) = 0$ is situated in the center of the ring electrodes (trap center). The electric potential in cylindrical coordinates is described in the following way:

$$U(z, r) = \frac{U_0}{2d^2}\left(z^2 - \frac{r^2}{2}\right). \tag{3.7}$$

d is the characteristic trap parameter which is defined by the minimum of the axial z_0 and radial r_0 distances to the electrodes as:

$$d^2 = \frac{1}{2}\left(z_0^2 + \frac{r_0^2}{2}\right). \tag{3.8}$$

The electric field $\vec{E} = -\nabla U$ can be written as

$$\vec{E} = \frac{U_0}{2d^2}(x, y, -2z). \tag{3.9}$$

Here, the relation $r^2 = x^2 + y^2$ was used.

The three-dimensional motion of a particle in a Penning trap can be described by Newton's equation of motion:

$$m\vec{a} = q \cdot \vec{E} + q \cdot \vec{v} \times \vec{B}. \tag{3.10}$$

With the help of Eq. (3.9) this can be written in three equations for the three coordinates x, y and z:

$$\ddot{x} = \frac{qU_0}{2md^2}x + \frac{qB}{m}\dot{y} \tag{3.11}$$

$$\ddot{y} = \frac{qU_0}{2md^2}y - \frac{qB}{m}\dot{x} \tag{3.12}$$

$$\ddot{z} = -\frac{qU_0}{md^2}z. \tag{3.13}$$

The motion in z-direction is decoupled from the radial motions and is only dependent on the electrostatic potential $E_z = -U_0 z/d^2$. If the initial condition $q \cdot U_0 > 0$ is fulfilled the ions perform a harmonic oscillation parallel to the z-axis as a consequence of the electrostatic potential. The characteristic eigenfrequency can be determined with the ansatz $z = z_0 e^{-i\omega_z t}$ to be

$$\omega_z = \sqrt{\frac{qU_0}{md^2}}\ . \tag{3.14}$$

The equations of motion can thus be written as

$$\ddot{x} - \omega_c\dot{y} - \frac{1}{2}\omega_z^2 x = 0 \tag{3.15}$$

$$\ddot{y} + \omega_c\dot{x} - \frac{1}{2}\omega_z^2 y = 0 \tag{3.16}$$

$$\ddot{z} + \omega_z^2 z = 0. \tag{3.17}$$

To determine the coupled motions in the xy-plane the complex variable $u = x + iy$ is introduced [Kret1991]. With the help of these variables the two linear differential equations (3.15, 3.16) can be written in only one complex differential equation[4]:

$$\ddot{u} + i\omega_c\dot{u} - \frac{1}{2}\omega_z^2 u = 0. \tag{3.18}$$

[4]This expression is obtained by adding Eq. (3.15) to i-times Eq. (3.16) and using $u = x + iy$, $\dot{u} = \dot{x} + i\dot{y}$ and $\ddot{u} = \ddot{x} + i\ddot{y}$

Using the ansatz $u = u_0 e^{-i\omega t}$ leads to:

$$\omega^2 - \omega_c \omega + \frac{1}{2}\omega_z^2 = 0, \tag{3.19}$$

with the two characteristic eigenfrequencies

$$\omega_\pm = \frac{1}{2}\left(\omega_c \pm \sqrt{\omega_c^2 - 2\omega_z^2}\right). \tag{3.20}$$

ω_+ is called reduced or modified cyclotron frequency, ω_- is the magnetron frequency. From the equations (3.14) and (3.20) we obtain in the case of an ideal Penning trap the following expression for the eigenfrequencies:

$$\omega_c = \omega_+ + \omega_-. \tag{3.21}$$

In a more general case with distorted fields the eigenfrequencies still fulfill the invariance theorem [Gabr2008]

$$\omega_c^2 = \omega_+^2 + \omega_-^2 + \omega_z^2 \ . \tag{3.22}$$

Fig. 3.7 shows a schematic view of the motion of one ion in a Penning trap as a superposition of its three eigenmotions. From the constraint that the expression

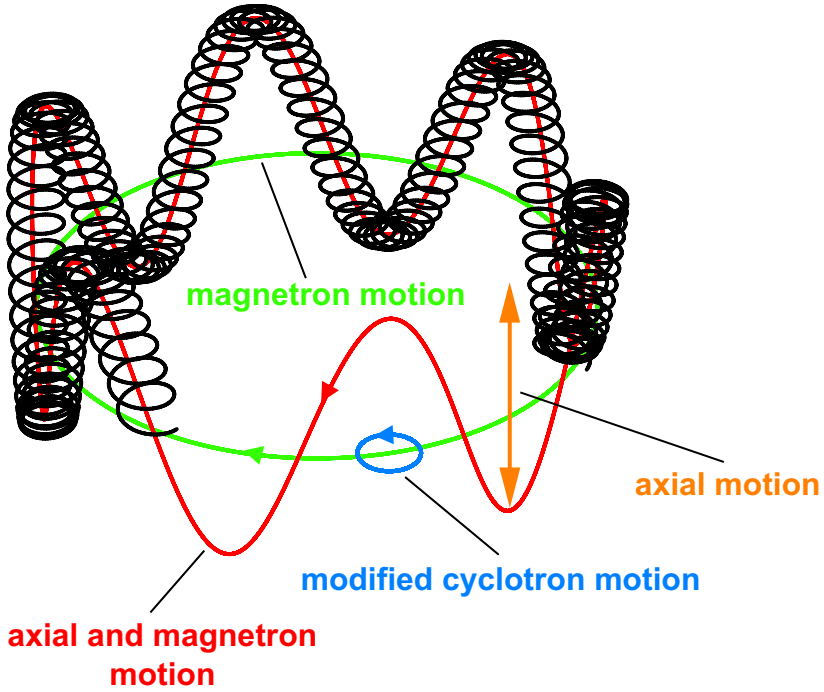

Figure 3.7: Schematic view of the characteristic motion of an ion in a Penning trap (assembly see Fig. 3.6). It is a superposition of three eigenmotions: One oscillation parallel to the z-axis, one fast, modified cyclotron motion and one slow, azimuthal precession around the trap center which is called magnetron motion. Cyclotron motion and magnetron motion are both in the radial xy-plane.

under the square root in Eq. (3.20) has to be positive, the stability criterion for the magnetic field strength can be obtained:

$$\omega_c^2 > 2\omega_z^2 \tag{3.23}$$

or

$$B > \sqrt{2\frac{m}{q}\frac{U_0}{d^2}}, \tag{3.24}$$

respectively. Using the frequency

$$\omega_1 := \sqrt{\omega_c^2 - 2\omega_z^2} \tag{3.25}$$

the eigenfrequencies can be identified as the reduced cyclotron frequency

$$\omega_+ = \frac{1}{2}\left(\omega_c + \omega_1\right) \tag{3.26}$$

and the magnetron frequency

$$\omega_- = \frac{1}{2}\left(\omega_c - \omega_1\right). \tag{3.27}$$

The frequencies ω_+ and ω_- of the two radial motions can be obtained by performing an approximation for the frequency ω_1. Therefore Eq. (3.25) is written in the form

$$\omega_1 = \omega_c \left(1 - \frac{2\omega_z^2}{\omega_c^2}\right)^{\frac{1}{2}}, \tag{3.28}$$

which can be approximated for $\omega_c \gg \omega_z$ to be

$$\omega_1 \approx \omega_c \left(1 - \frac{1}{2} \cdot \frac{2\omega_z^2}{\omega_c^2}\right). \tag{3.29}$$

Thus, one obtains

$$\omega_1 \approx \omega_c - \frac{\omega_z^2}{\omega_c}, \tag{3.30}$$

which leads together with Eq. (3.6) and Eq. (3.14) to the following two expressions for the radial frequencies:

$$\omega_+ \approx \omega_c - \frac{U_0}{2d^2 B} \tag{3.31}$$

and

$$\omega_- \approx \frac{U_0}{2d^2 B}\ . \tag{3.32}$$

In this equation it is obvious that the magnetron frequency is mass independent to first order. These two frequencies result from the contribution of the additional electric field. Without electric field ω_+ is equal to the free cyclotron frequency ω_c and ω_- is zero.

In the ideal case the three ion motions are decoupled and can be described each by a quantized harmonic oscillator [Kret1999]. In Fig. 3.8 the energy scheme with the

discrete energy states of the single motions - the so-called *Landau levels* - is shown for a spinless particle. The total energy can be obtained as the sum of the energies of the three independent eigenmotions:

$$E = \hbar\omega_+(n_+ + \frac{1}{2}) + \hbar\omega_z(n_z + \frac{1}{2}) - \hbar\omega_-(n_- + \frac{1}{2}) \ . \tag{3.33}$$

The negative contribution of the magnetron motion to the potential means that an increase in the quantum number n_- - which is equal to an increase in the magnetron radius - leads to a lower potential energy. The other eigenmotions have positive contributions.

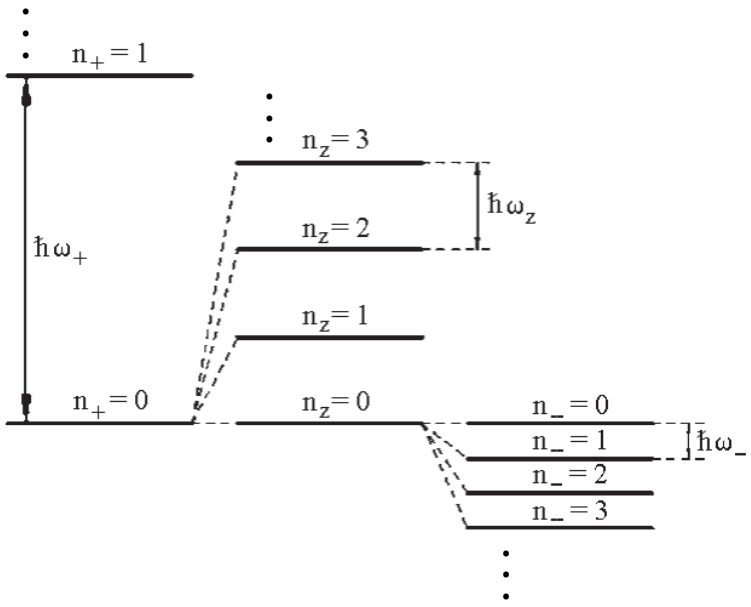

Figure 3.8: Energy scheme of a harmonic oscillator for spinless charged particles in an ideal Penning trap. ω_+ is the reduced cyclotron frequency, ω_z the axial frequency and ω_- the magnetron frequency. The corresponding quantum numbers are called n_+, n_z and n_-.

The Penning trap can be used to perform mass measurements on stable and radioactive nuclides. The mass determination is done via the measurement of the cyclotron frequency. As it is obvious from Eq. (3.6), the cyclotron frequency $\nu_c = \omega_c/2\pi$ is inversely proportional to the mass m of the nuclide. The cyclotron frequency is determined by applying adequate excitations to the ring electrode segments (see Sec. 3.4.3). For the mass measurements performed within this work the SHIPTRAP mass spectrometer (Chap. 3) at the GSI Helmholtzzentrum für Schwerionenforschung in Darmstadt (Germany) was used. A more detailed description of the mass measurement process can be found in Sec. 3.4.5.

3.4.2 The real Penning trap

The equations above describe the undisturbed motion of a single particle in an ideal Penning trap. In this ideal case we suppose three totally decoupled eigenmotions

of a particle captured in the trap. The eigenfrequencies are only dependent on the dimension of the trap, the electric and magnetic field and the mass m and charge q of the stored particle. This explanation turns out to be too simple for a real Penning trap, where several deviations from the ideal geometry due to field inhomogeneities and other imperfections have to be taken into account [Brow1986, Boll1996, Boll2004, Majo2005].

Inhomogeneity of the electric field

The equipotential surfaces of an ideal quadrupolar electric field have the shape of rotational hyperboloids. This should also be the shape of the electrodes creating the electric field. At SHIPTRAP both Penning traps, the preparation as well as the measurement trap, have cylindrical shape. To create a harmonic electric potential additional correction electrodes are used.

Even when using hyperbolic traps there will always occur some deviations from the ideal electric harmonic potential. The fact that the electrodes are not infinite and the end caps have holes for the injection and ejection of the ions always leads to some unavoidable deviations from the ideal shape. Also in this case the electric potential has to be corrected with additional electrodes.

The imperfections of the electric field due to high order coefficients lead to a shift in the free cyclotron frequency ω_c which can be written as [Boll1990]

$$\Delta\omega_c^{elec} = \Omega_c^{elec}\left(\frac{3}{2}\cdot\frac{C_4}{d^2}(r_-^2 - r_+^2) + \frac{15}{4}\cdot\frac{C_6}{d^4}\left[r_z^2(r_-^2 - r_+^2) - (r_-^4 - r_+^4)\right]\right). \quad (3.34)$$

The coefficients C_4 and C_6 are representing the octopole and dodecapole components of the electric field. They have to be taken into account for real traps and can be reduced if the shape of the trap electrodes is getting closer to the ideal hyperbolic shape. The quantities r_+, r_- and r_z are the radii of the three eigenmotions. The parameter Ω_c^{elec} is in first approximation equal to the magnetron frequency ω_-, which means that the whole expression for the frequency shift is mass and charge independent. As obvious from Eq. (3.34) the frequency shift can be reduced by increasing the characteristic trap parameter d and reducing the motion radii of the ions. Favorable are also small trap potentials U_0 and strong magnetic fields B.

An additional cyclotron frequency shift results from a misalignment of the trap axis with respect to the magnetic field. The z-axis of the Penning trap, which is defining the axis of the electric field, should coincide with the axis of the magnetic field. This is very hard to achieve in practice. Deviations from the ideal field shape lead to a weak coupling of the eigenmotions and to a change of the eigenfrequencies. For small tilting angles θ the cyclotron frequency shift can be approximated as [Boll1990]

$$\Delta\omega_c^{tilt} \approx \frac{9}{4}\omega_- \sin^2\theta. \quad (3.35)$$

Also this frequency shift is mass independent. The alignment of the trap has thus to be done very carefully. A tilting angle of $\theta = \pm\, 0.03°$ (resulting from a misalignment of $\pm$ 0.5 mm of the trap section, which has a length of about 1 m at SHIPTRAP) leads to a frequency shift of $\Delta\omega_c^{tilt} \approx \pm 0.6$ mHz, which results in an additional relative uncertainty in the order of 10^{-10} to 10^{-9}, depending on the cyclotron frequency

of the measured ion. Assuming a cyclotron frequency of 1 MHz this leads to a mass excess uncertainty of about 50 eV.

Inhomogeneity of the magnetic field

Since the magnetic susceptibility of the materials used in the setup are not equal to zero, the homogeneity of the magnetic field in the trap center can be disturbed by the presence of trap electrodes, holders, electric cables in the vacuum chamber and the vacuum tube itself. To minimize these disturbing effects the choice of the used materials has to be made very carefully. In particular for the susceptibilities of the trap materials very small values have to be chosen. Another reason is the use of shim coils for the construction of the magnet. Typical superconducting solenoids provide a field homogeneity of better than 1 ppm over a volume of 1 ccm.

The cyclotron frequency shift due to high order coefficients of the magnetic field is given by [Brow1986]

$$\Delta\omega_c^{magn} \approx \beta_2\omega_c(r_z^2 - r_-^2). \tag{3.36}$$

The odd contributions to $\Delta\omega_c^{magn}$ cancel due to symmetry reasons. In contrary to the frequency shifts due to electric field imperfections this frequency shift is dependent on the free cyclotron frequency ω_c.

Furthermore, the magnetic field is decreasing permanently over the time. This so-called *flux creep* phenomenon [Ande1962, Ande1964] is well understood and can be approximated by a linear decrease. Other fluctuations of the magnetic field are resulting from temperature and pressure changes within the magnet. To get rid of these fluctuations a temperature and pressure stabilization system - which is based on a PID regulation - has been developed for SHIPTRAP [Droe2009].

Most of the effects described above increase with higher amplitudes of the ion motions. Hence it is necessary to cool the trapped particles (see Sec. 3.4.4).

Ion-ion interaction

The considerations above are only valid for one single particle in the trap. If there are more ions captured they will interact with each other due to the Coulomb force. The more ions are stored in the trap the stronger is this interaction. Especially the effects of these interactions on the real cyclotron frequency ν_c are of interest, since ν_c is used for mass determination (see Sec. 3.4.5).[5]

If several ions are stored in the trap the resulting space charges create an additional electric field. This leads to shifts of the eigenfrequencies of the stored particles. For the case that only ions of one ion species are stored in the trap it can be shown that only the frequencies ν_+ and ν_- are shifting for an increasing number of ions, the frequency ν_c, however, stays constant[6] [Stur2007]. In this case only a line broadening

[5] In the previous sections the frequencies of the ion motions were written as ω_c, ω_+, ω_-, ω_z, which is more convenient for the derivation of the equations of motion. Now the notation is changed to ν_c, ν_+, ν_- and ν_z, since these are the frequencies one can actually measure.

[6] This statement is only correct if no excitation or dipole excitation, respectively, is applied to the ions in the trap. By applying a quadrupolar exciation (see Chap. 3.4.3) - which is necessary for the mass determination with the TOF-ICR method (see Chap. 3.4.5) - the cyclotron frequency ν_c is also changed. This change can be corrected by applying z-class analysis [Kell2003].

of the resonance curve due to the change of the electrostatic potential is observed.

If particles of different masses are captured at the same time both effects, a line broadening and a shift of ν_c, occur. In this case the behavior depends on the mass difference of the ion species, or on their frequency difference, respectively. If the difference of the resonance frequencies is smaller than the FWHM (Full Width at Half Maximum) of the resonance curve no information over the exact frequency values can be made. The only observable is the center-of-mass frequency of the single resonances. In the case that the two species can be resolved a resonance frequency shift to lower frequencies is observed [Boll1992]. A more detailed description of the ion-ion interaction can be found in [Köni1991].

3.4.3 Excitation of the ion motions in a Penning trap

Apart from the storage of ions it is also possible to perform a selective manipulation of the ion motion in a Penning trap. The most common methods of ion excitation are the dipolar and the quadrupolar excitation. To perform a dipolar excitation an azimuthally twofold-segmented ring electrode has to be used (see Fig. 3.9(a)). It is used for the excitation of one eigen motions. The quadrupolar excitation (see Fig. 3.9(b)) is used to couple two different motions. In case of an excitation at the sum frequency ν_c (Eq. (3.21)) magnetron and cyclotron motion are coupled and continuously converted into each other.

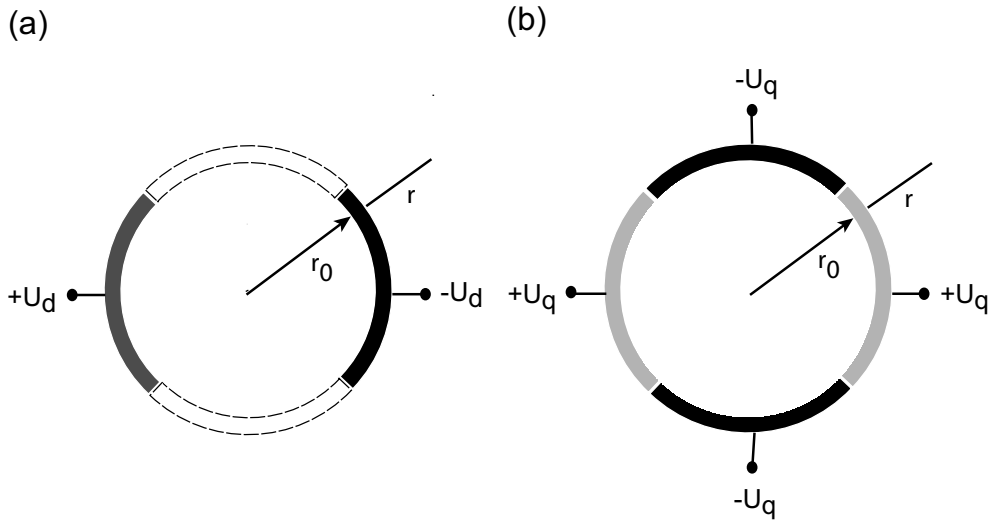

Figure 3.9: The radial segmentation of the ring electrode (topview) to apply an alternating electromagnetic field. (a) shows the case of dipolar excitation: a radio frequency is applied at two opposite segments of the ring electrode in order to create a dipolar field. A quadrupolar field is created by applying a radio frequency signal of the same phase at two opposite segments of a four-segmented ring electrode (b).

Dipolar excitation

One possibility to excite the ions in the trap is a dipolar excitation. If the frequency of a dipolar excitation coincides with a resonance frequency of the trapped ion, its amplitude is increased continuously during the time in which the excitation is applied. Taking advantage of the fact that the magnetron motion of the ions is in first order mass independent (see Eq. (3.32)) all ions in the trap can be excited simultaneously by applying a radio-frequency signal at the frequency ν_- to the ring electrodes. On the other hand it is possible to selectively remove a certain ion species from the trap by exciting it at the reduced cyclotron frequency ν_+. This possibility is used for the mass selective cleaning of contaminant ions (see Sec. 3.4.4). To create the dipolar field an alternating voltage is applied to two opposite segments of the ring electrode (see Fig. 3.9(a)). Normally a sine voltage is chosen as excitation signal. The electric field which is then created is described by the equation

$$\vec{E_x} = \frac{U_d}{r_0} \cdot \cos\left(2\pi\nu_d t + \Phi_d\right) \cdot \hat{e}_x. \tag{3.37}$$

U_d is the amplitude of the voltage applied to the electrodes at radius r_0, ν_d the excitation frequency and Φ_d the phase. If the radio-frequency signal has the same phase as the ion motion (see Fig. 3.10(a)) a linear increase of the magnetron radius starts right at the beginning of the excitation. If the phase difference is equal to 180° (see Fig. 3.10(b)) the magnetron radius of the ion motion first decreases until zero. After this it continues with a linear increase. Fig. 3.11 shows the magnetron radius for different phases as a function of the excitation time.

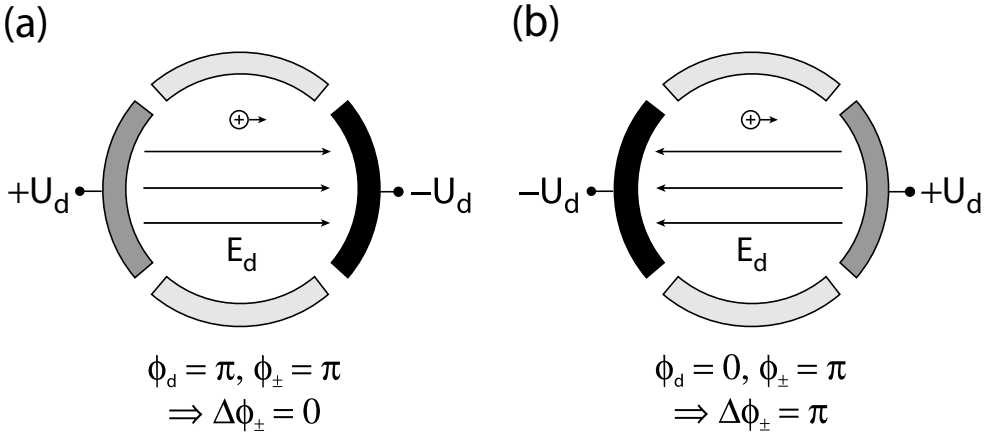

Figure 3.10: The phase between the applied dipole field and the ion motion. In (a) dipole field and ion motion have the same phase, in (b) they have a phase shift of 180°.

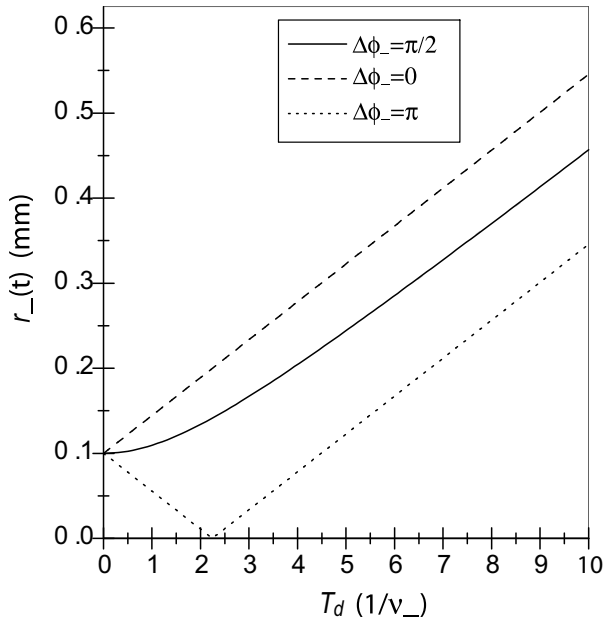

Figure 3.11: The development of the magnetron radius as a function of the dipole excitation time for the phase differences 0, 90° and 180° between the applied dipole field and the ion motion [Blau2003].

Quadrupolar excitation

For a quadrupolar excitation an RF signal is applied to a fourfold-segmented ring electrode (see Fig. 3.9(b)). The same phase of a sinosoidal excitation signal is applied to two opposite segments. The quadrupolar excitation can be described by the following two equations:

$$\vec{E_x} = \frac{2U_q}{r_0^2} \cdot \cos\left(2\pi\nu_q t + \Phi_q\right) \cdot y\hat{e}_x \tag{3.38}$$

and

$$\vec{E_y} = \frac{2U_q}{r_0^2} \cdot \cos\left(2\pi\nu_q t + \Phi_q\right) \cdot x\hat{e}_y. \tag{3.39}$$

A coupling of the two radial motions is achieved if the excitation frequency is chosen in the way that it corresponds to the sum frequency of the radial eigenfrequencies:

$$\nu_c \equiv \nu_+ + \nu_- = \nu_q \tag{3.40}$$

This enables a continuous conversion between magnetron motion and modified cyclotron motion (see Fig. 3.12). After a certain time T_{conv}, which is given by

$$T_{conv} = \frac{4\pi r_0^2 B}{U_q}, \tag{3.41}$$

one motion is fully converted into the other one [Boll1990]. In the case of a non-resonant excitation ($\nu_q \neq \nu_c$) with the same excitation time, the conversion is not complete [Köni1995]. The radial energy E_r fulfils the equation [Brow1986]:

$$E_r \propto \nu_+^2 r_+^2(0) - \nu_-^2 r_-^2(0) \approx \nu_+^2 r_+^2(0), \tag{3.42}$$

since

$$\nu_+ \gg \nu_-. \tag{3.43}$$

Thus, a resonant coupling of magnetron motion and modified cyclotron motion leads to a maximum increase of the radial energy and the magnetic moment.

Quadrupolar excitation with the cyclotron frequency ν_c is mass-selective and can thus be used for mass-selective buffer gas cooling (see Chap. 3.4.4) [Sava1991] and for the determination of the cyclotron frequency with the time-of-flight resonance method (see Chap. 3.4.5) [Köni1995]. At SHIPTRAP also octopolar excitation was tested successfully [Elis2007a]. The advantage of this excitation is that the frequency $2\nu_c$ can be excited, which leads to a smaller relative uncertainty for the same measurement time.

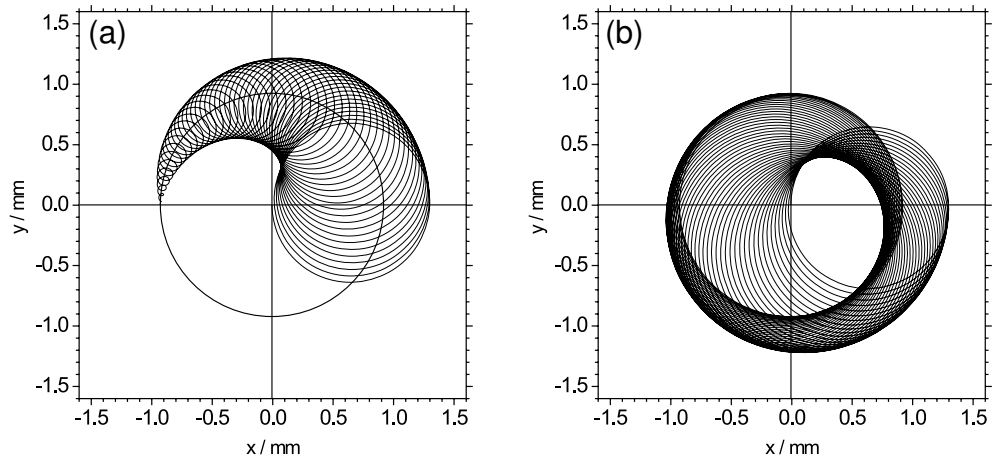

Figure 3.12: The conversion from magnetron motion to modified cyclotron motion by applying a quadrupolar field with the cyclotron frequency $\nu_c = \nu_+ + \nu_-$. At the starting point the ion performs a pure magnetron motion which is drawn as a black circle at the origin. (a) shows the first and (b) the second half of the conversion.

3.4.4 Buffer gas cooling of the stored ions

The buffer gas cooling is used to reduce the amplitude of the ions which are stored in the trap. Like this the uncertainty of position and energy of an ion is minimized. It also helps to reduce frequency shifts due to inhomogeneities of the electric and magnetic field. Furthermore, it provides the possibility to minimize the amplitude of the axial motion in order to obtain a narrow time-of-flight distribution. At SHIPTRAP the mass-selective buffer gas cooling is applied in the preparation trap to remove unwanted ions. Like this, in an ideal case, only ions of one species are transferred to the measurement trap.

Ions of the mass m and the velocity $\vec{v}$ loose kinetic energy due to collisions with molecules of a light buffer gas. This effect can be described by introducing a velocity dependent damping force

$$\vec{F} = -\delta \cdot m \cdot \vec{v} \tag{3.44}$$

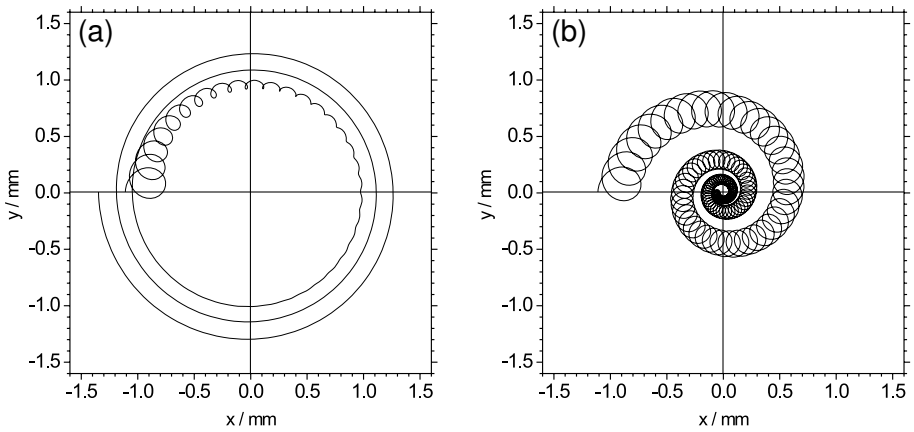

Figure 3.13: The radial ion motion in a Penning trap filled with buffer gas in a plane perpendicular to the magnetic field. The center of the trap is marked by the horizontal and the vertical line. (a) Due to the velocity dependent damping the cyclotron radius is reduced very quickly and the magnetron radius increases slowly. The last effect leads to a loss of the ions. (b) An additional quadrupolar excitation at $\nu_c = \nu_+ + \nu_-$ leads to a coupling of the two radial motions and thus causes a slow decrease of the cyclotron and the magnetron radius. Since ν_c is mass dependent it is possible to center only one ion species [Sava1991].

with the damping coefficient

$$\delta = \frac{q}{m} \cdot \frac{1}{M_{ion}} \cdot \frac{p/p_N}{T/T_N}. \tag{3.45}$$

The pressure p and the temperature T of the buffer gas are chosen in units of the normal pressure p_N and the normal temperature T_N. M_{ion} is the reduced mobility of the ions in the gas. In general inert gases are used as buffer gas. Due to their high ionization potential they show smaller losses due to charge exchange. The damping causes a decrease of the amplitudes of modified cyclotron motion and axial motion. The magnetron radius, however, increases due to the negative potential energy of the magnetron motion. For too long excitation times or too high amplitudes this leads to a loss of the ions. By coupling the magnetron motion to one of the other two motions this ion loss can be avoided.

If quadrupolar excitation is performed at the real cyclotron frequency ν_c the two radial motions - modified cyclotron motion and magnetron motion - are coupled and are continuously converted into each other. Due to Eq. (3.44) the modified cyclotron motion is damped much faster than the magnetron motion since ν_+ is much bigger than ν_-. This is illustrated in Fig. 3.13 (a). The damping leads to a loss of energy of the ion, which results in a reduction of the radius of the ion motion.

If the excitation frequency matches the cyclotron frequency $\nu_c = qB/(2\pi m)$ of an ion with mass m only particles with this mass will be centered. This mass-selective centering [Sava1991] of only one ion species is shown in Fig. 3.13(b). The ejection of the stored ions through an orifice behind the end cap of the preparation trap (see Fig. 3.5) offers the possibility to select single ion species. Figure 3.14 shows the

number of ejected ions from the preparation trap as a function of the quadrupolar excitation frequency. In this way each of the four isobars $^{147}Er^+$, $^{147}Ho^+$, $^{147}Dy^+$ and $^{147}Tb^+$ can be excited and detected separately.

The resolving power is defined as the quotient of the excitation frequency (in this case the cyclotron frequency ν_c) and the FWHM of the resonance peak $\Delta\nu_c$:

$$R = \frac{\nu_c}{\Delta\nu_c}. \tag{3.46}$$

It is mainly determined by the buffer gas pressure, the excitation amplitude and the excitation time. These three parameters are, however, correlated. The product of excitation amplitude and excitation time has to be chosen such that one full conversion from magnetron into cyclotron motion is obtained. Since the peak width $\Delta\nu_c$ is inversely proportional to the excitation time long excitation times are favorable to obtain a high resolution. However, in the case of the preparation trap, the decrease of the peak width is limited by the buffer gas pressure. Thus, the latter is the most important parameter limiting the resolving power in the purification trap, which is about $R = 10^5$ at SHIPTRAP. Another limiting parameter for the excitation time is the half-life of the nuclide.

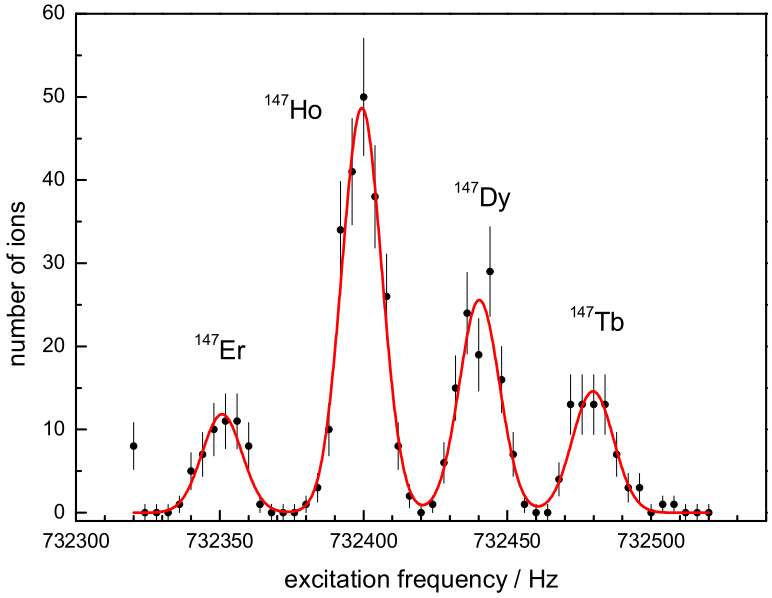

Figure 3.14: The number of ions is plotted as a function of the quadrupolar excitation frequency in the preparation trap. If the excitation frequency matches the cyclotron frequency of a certain ion its magnetron motion is converted into cyclotron motion. Due to its higher frequency the cyclotron motion is cooled and thus the ions are centered. In this way a mass-selective cooling can be performed. Here the four isobars ^{147}Er, ^{147}Ho, ^{147}Dy and ^{147}Tb were resolved with a mass resolving power of $5 \cdot 10^4$.

3.4.5 Mass measurement in a Penning trap

A Penning trap provides the possibility to perform high-precision mass measurements. The method presently used at SHIPTRAP makes use of the so-called time-of-flight ion cyclotron resonance detection technique, which is explained in the following section. With this method the cyclotron frequency of a charged particle can be determined.

The time-of-flight ion cyclotron resonance detection technique

The time-of-flight ion cyclotron resonance detection technique [Gräf1969, Gräf1980] is a very accurate way to determine the cyclotron frequency. In contrary to the mass-selective buffer gas cooling (see Fig. 3.14) it is not based on measurements of the count rate, but makes use of the energy difference of resonant and non-resonant ions, which manifests itself in a time-of-flight difference. With this method relative mass uncertainties of about 10^{-10} can be reached for stable nuclides [Frit2001, Sold2008]. For short-lived exotic nuclei a relative uncertainty of a few parts in 10^{-9} was demonstrated [Boll2006]. The resolving power at SHIPTRAP is about 10^6. With a cyclotron frequency of $\nu_c = 1$ MHz and an excitation time of $T_{exc} = 1$ s this allows the resolution of isomers with excitation energies of about 100 keV [Roos2004].

The principle of this measurement technique is illustrated for an ion with charge q which is circulating on a circle with radius ρ in a magnetic field $\vec{B}$ with frequency ω. The current I and the magnetic dipole moment created by the ion can then be written as

$$I = q\frac{\omega}{2\pi} \tag{3.47}$$

and

$$\vec{\mu} = I \cdot \hat{a} \ , \tag{3.48}$$

respectively. $\hat{a}$ represents the normal vector to the plane of the ion motion. The potential energy of the magnetic dipole moment $\vec{\mu}$ in the magnetic field $\vec{B}$ is given by the expression

$$E_{pot} = -\vec{\mu} \cdot \vec{B} \ . \tag{3.49}$$

In the Penning trap $\vec{\mu} = (0, 0, \mu)$ and $\vec{B} = (0, 0, B)$ are antiparallel. Thus, the potential energy of the ion in the magnetic field can be written as

$$E_{rad} = \mu B = \frac{1}{2} q\omega r^2 B \ . \tag{3.50}$$

The trapped ion is first excited with ν_- to the radius r_-.[7] After the magnetron excitation the ions are excited with the excitation frequency ν_{exc}, which is chosen in the vicinity of the expected cyclotron frequency ν_c. Then the ion is ejected from

[7] This radius should be as large as possible to obtain a big TOF-effect, which is defined by: TOF-effect/% $= 100(1 - TOF[\text{res}]/TOF[\text{baseline}])$, where TOF[res] is the mean time of flight of the resonant ions and TOF[baseline] is the time of flight of the non-resonant ions. It is, however, limited by the fact that ions with too big radii are deflected by the outer magnetic field lines and are thus not focused on the detector. Small radii are also favorable because of field inhomogeneities. A typical value for the radius after magnetron excitation is $r_- = 0.7$ mm.

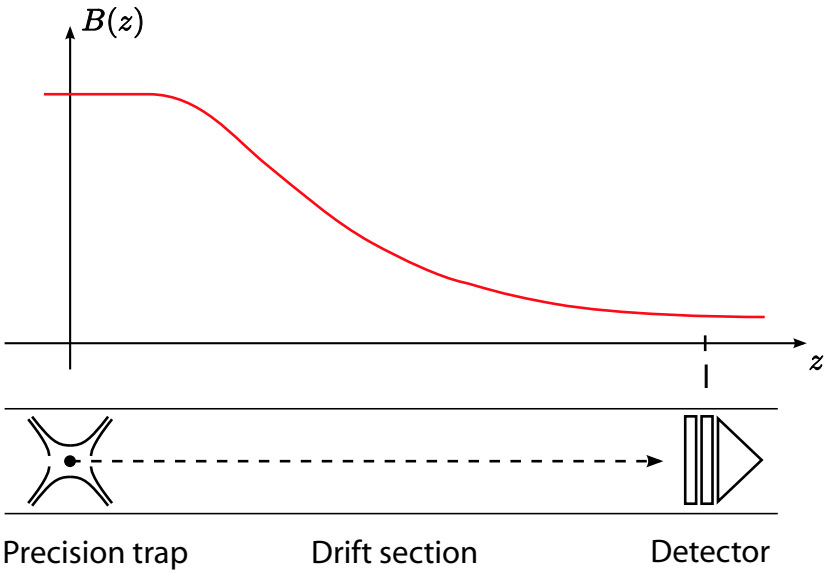

Figure 3.15: Magnetic field gradient from the Penning trap to the MCP or Channeltron detector. In the case of SHIPTRAP the distance l is about one meter.

the Penning trap by lowering the potential of the end cap and their time of flight from the trap to a detector is measured. At SHIPTRAP the distance from the measurement trap to the detector is about one meter. In this section the magnetic field is decreasing from 7 T to approximately zero (see Fig. 3.15). The magnetic moment $\vec{\mu}$ of the ion is then coupled to the magnetic field gradient $\frac{\partial \vec{B}}{\partial z}$ resulting in a force on the ion described by

$$\vec{F} = \vec{\mu} \cdot \frac{\partial \vec{B}}{\partial z} \ . \tag{3.51}$$

This force is converting the radial energy of the ion into axial energy. The axial energy is directly linked to the velocity of the ion in z direction and hence with the time of flight to the detector, which can be written as

$$T(\omega_q) = \int_0^l \sqrt{\frac{m}{2(E_0 - qU(z) - \mu(\omega_q)B(z))}} \, dz \ , \tag{3.52}$$

where E_0 is the initial axial energy of the ion, $U(z)$ the voltage and $B(z)$ the magnetic field. A short time of flight can thus be identified with a high radial energy and vice-versa. The time-of-flight ion cyclotron resonance detection technique is taking benefit from this correlation. The time of flight is determined for different excitation frequencies ν_{exc} and a typical result for ^{133}Cs is plotted in Fig. 3.16.

If the excitation frequency ν_{exc} is equal to the cyclotron frequency ν_c, the slow magnetron motion is fully converted into the fast cyclotron motion[8]. In this case the

[8]The amplitude U_{exc} of the excitation is determined for fixed excitation time T_{exc} in the way that one full conversion from magnetron to cyclotron motion is reached if the excitation frequency is equal to the cyclotron frequency ($\nu_{exc} = \nu_c$).

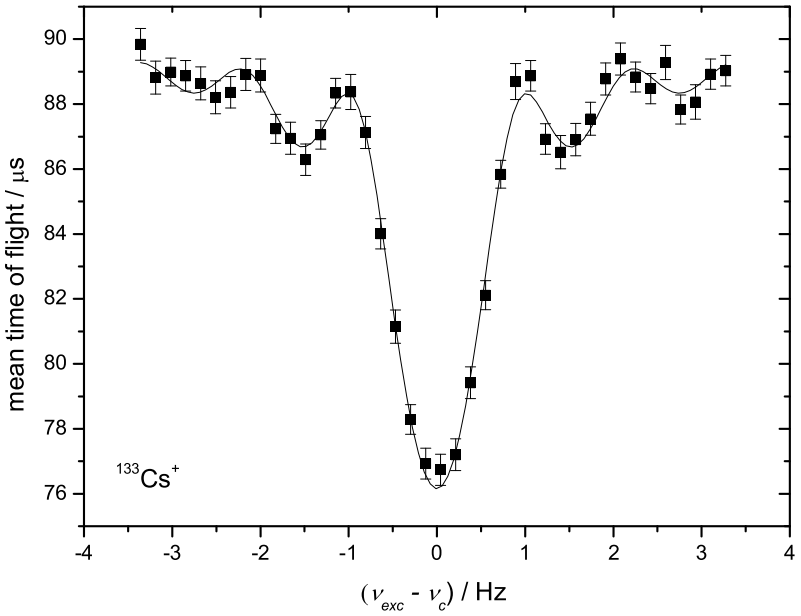

Figure 3.16: Time-of-flight resonance of $^{133}Cs^{+}$. The mean time of flight is plotted as a function of the excitation frequency ν_{exc}. The black line is a fit of the theoretical line-shape to the experimental data points [Köni1995]. The excitation time was chosen to be T_{exc} = 900 ms. The cyclotron frequency was ν_c = 809334.619(17) Hz.

radial energy of the ion is at maximum. Thus one expects a time-of-flight minimum for resonant ions.

The frequency range in which the time-of-flight spectrum is recorded depends on the excitation time T_{exc} and is normally chosen in the way that two sidebands are visible on each side of the resonance dip.

Normally the time of flight is measured for about 40 different excitation frequencies ν_{exc}. This measurement cycle is repeated until approximately 500 ions are recorded. Then the mean time of flight is plotted as a function of the excitation frequency ν_{exc}. The theoretical line-shape of this time-of-flight resonance curve is well-known [Köni1995]. It is given by the Fourier transform of the rectangular excitation pulse. This is the reason why not only the central peak, but also several sidebands are observed. From the fit of the theoretical curve to the data one obtains the cyclotron frequency ν_c and its uncertainty. The statistical uncertainty of the frequency determination from a time-of-flight resonance is connected to the number N of detected ions and the excitation time T_{exc} [Kell2003]:

$$\sigma_{stat}(\nu_c) \propto \frac{1}{\sqrt{N} \cdot T_{exc}}. \tag{3.53}$$

The resolving power is given by the Fourier limit: $R \approx T_{exc} \cdot \nu_{exc}$, which means that longer excitation times are favorable. The excitation time is, however, limited

by the pressure in the measurement trap and the half-life of the ion of interest. In practice excitation times of 900 ms or 1.2 s are realistic if the half-life is long enough.

Apart from the excitation with one single rectangular pulse it is also possible to split the excitation signal into two or more pulses doing a so-called *Ramsey excitation* [Geor2007]. Then a smaller uncertainty in the frequency determination can be obtained for the same excitation time. This method was successfully tested at ISOLTRAP (ISOLDE/CERN), where it was possible to obtain a comparable accuracy with much shorter measurement time compared to the normal rectangular excitation pulse. It is, however, difficult to apply if isobaric contaminations or isomers are expected.

Mass determination

As already mentioned in Sec. 3.4.1 the mass m is directly linked to the cyclotron frequency ν_c (see Eq. (3.6)). Every cyclotron frequency ν_c measured in a Penning trap can thus be identified with a certain charge-to-mass ratio q/m if the magnetic field B is known. The B field in a super-conducting magnet is, however, not constant but approximately linearly decreasing with time due to flux-creep [Ande1962, Ande1964] and in addition shows fluctuations due to temperature and pressure changes. The problem can be solved by calibrating the B-field using well-known reference masses. The cyclotron frequency $\nu_{c,ref}$ of a reference mass m_{ref} is then measured before and after the measurement of the cyclotron frequency ν_c of the ion of interest. From these two frequency values $\nu_{c,ref,1}$ and $\nu_{c,ref,2}$ the cyclotron frequency $\nu_{c,ref,0}$ at the time of the measurement of the cyclotron frequency ν_c of the ion of interest is interpolated. It is then assumed that the interpolated frequency $\nu_{c,ref,0}$ gives information on the magnetic field B at the time of the measurement ν_c. By equating the two equations

$$\nu_c = \frac{1}{2\pi} \cdot \frac{n \cdot e}{m_{atom} - n \cdot m_e} \cdot B \tag{3.54}$$

and

$$\nu_{c,ref,0} = \frac{1}{2\pi} \cdot \frac{n_{ref} \cdot e}{m_{atom,ref} - n_{ref} \cdot m_e} \cdot B \tag{3.55}$$

over B one obtains the following expression for the mass of the ion of interest:

$$m_{atom} = \frac{n}{n_{ref}} \frac{\nu_{c,ref}}{\nu_c} (m_{atom,ref} - n_{ref} \cdot m_e) + n \cdot m_e. \tag{3.56}$$

The charge of the ion of interest is written as n times the elementary charge e and the charge of the reference ion as n_{ref} times e. One has to take into account that for an ion with the charge n the measured frequency ν_c corresponds to the mass $m_{atom} - n \cdot m_e$. The binding energies of electrons can be neglected since they are about two orders of magnitude smaller than the uncertainties of the mass determination for radionuclides.

At SHIPTRAP ^{85}Rb and ^{133}Cs are normally used as reference masses since their literature values have very small uncertainies[9]. They are obtained from an off-line

[9] According to [Audi2003] the absolute uncertainty of ^{85}Rb is 11 eV and the one of ^{133}Cs is 22 eV.

ion source which is placed in the transfer section behind the buncher and are always measured as singly charged ions.

3.5 The detectors

As already mentioned above it is necessary to use a detector at the SHIPTRAP experiment to perform measurements with the time-of-flight ion cyclotron resonance technique (see Sec. 3.4.5). For this purpose one MCP or Channeltron detector is sufficient. For the beam tuning, however, it is very helpful to implement an additional set of detectors to the setup. Apart from MCP detectors (see Sec. 3.5.2) and a Channeltron (see Sec. 3.5.3), which has the same working principle as an MCP detector, silicon detectors (see Sec. 3.5.1) are used.

This chapter gives a short overview over the working principle and the dedicated function of the detectors used at SHIPTRAP. The emphasis is put on a position sensitive delay-line detector (see Sec. 3.5.4) which was tested in the context of this thesis.

3.5.1 Silicon detectors

The silicon detectors at SHIPTRAP are used to detect α particles from radioactive decays. From the energies of these α decays one can draw conclusions to the nuclide which was decaying.

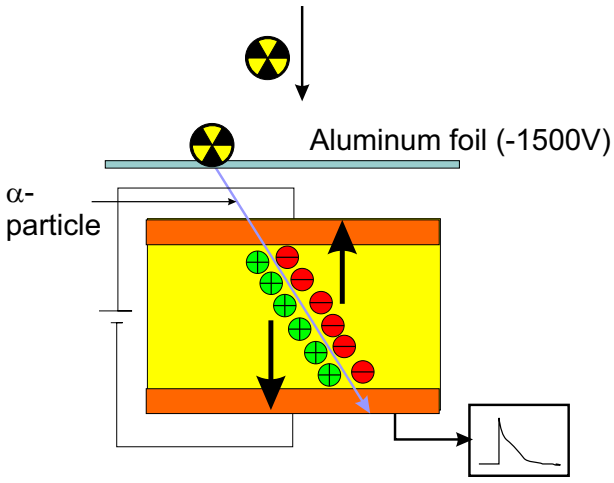

Figure 3.17: The working principle of a silicon detector is illustrated. The α particles which are impinging the detector from an aluminium foil create electron-whole pairs. These can be measured as a voltage pulse.

The detector consists of the semi-conductor silicon, which has a band gap of 3.4 eV. If α particles - which have energies in the order of several MeV - hit the detector, electron-whole pairs are produced and detected by measuring a voltage drop which is proportional to the energy of the α particle (see Fig. 3.17). This decay energy is characteristic for a certain nuclide and provides a simpler way for the identification

than a time-of-flight measurement. Silicon detectors are used at different positions for tuning of the radioactive beam from SHIP.

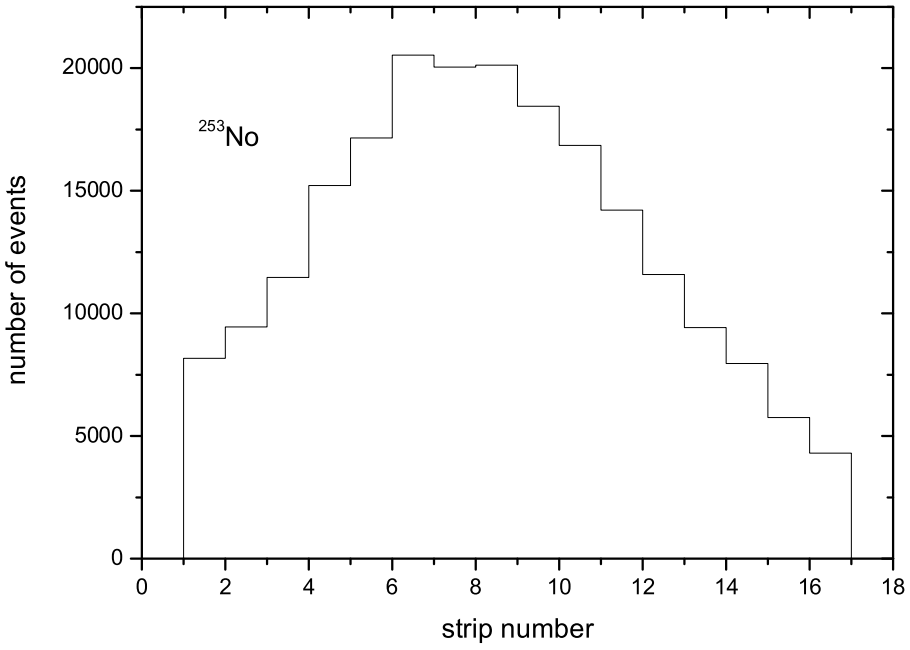

Figure 3.18: Spatial distribution of the α decays of ^{253}No in the silicon strip detector of SHIP. The number of events for each strip is shown.

The first silicon detector in the SHIPTRAP setup is mounted in front of the gas cell entrance window. It consists of 16 different strips and delivers thus also an information on the beam position. Figure 3.18 shows a spectrum from this so-called silicon-strip detector for the nobelium isotope ^{253}No. This spectrum was taken with a detector of SHIP.

The other three silicon detectors are not position-sensitive and are mounted behind the buncher (Si1), as well as in front of (Si2) and behind (Si3) the superconducting magnet. Si1 is very important for the optimization of the gas cell settings. Before every beam time they are calibrated with a ^{223}Ra recoil ion source ($T_{1/2}$ = 11.4 d) installed inside the gas cell which delivers the decay products ^{219}Rn, ^{215}Po and ^{211}Pb.

An absolute efficiency of the SHIPTRAP setup can also be determined by using silicon detectors. For this purpose a ^{223}Ra source of known activity is mounted to the gas cell and the activity of the individual silicon detectors is measured. The total efficiency is then calculated according to

$$\epsilon_{tot} = \epsilon_{GC} \cdot \epsilon_{buncher} \cdot \epsilon_{trans} \cdot \epsilon_{traps} \cdot \epsilon_{det}. \tag{3.57}$$

The efficiency of the gas cell is about 12% (see Sec. 3.2 and [Elis2007]). The efficiencies of the buncher $\epsilon_{buncher}$, the transfer ϵ_{trans} and the traps ϵ_{traps} have been

determined to be in the order of 50%. The detector efficiency is depending on the kind of detector which is used for recording the time-of-flight ion cyclotron resonance and is 30% for an MCP detector (see Sec. 3.5.2) and 90% for a Channeltron detector (see Sec. 3.5.3). The total efficiency is thus in the order of 0.5-2%.

3.5.2 MCP detectors

A micro-channel plate consists of an assembly of small channels with a diameter of about 10 μm which are made of a high resistive material[10]. The distance of two channels is about 15 μm. They are parallel to each other and typically have an angle of about 8° to the axis perpendicular to the surface. The thickness of a plate is about one to two millimeters and the resistance is in the order of some hundred MΩ.

In operation a voltage difference of 1000 V or more is applied across the micro-channel plate. If a particle enters a channel it will - due to the special geometry - hit the wall of the channel and emit an electron which is accelerated by the potential gradient thus starts a cascade of secondary electrons. These electrons lead to a current signal at the anode. To obtain a sufficiently large number of events (a cascade contains about 10^4 electrons) normally two micro-channel plates are added together. In this so-called Chevron configuration the signal at the anode is big enough to be detected.

For optimum working conditions a voltage gradient of about 1 to 1.5 kV over each MCP is chosen. Since the detection efficiency of the MCP is increasing with the energy of the detected ions, high voltages at the front plate are favorable. At SHIPTRAP the voltages of the MCP detectors are applied with a voltage divider as shown in Fig. 3.19. The front voltage (F) is applied in front of the first detector plate and is in the order of -3100 to -3300 V. The back voltage (B), which is in the order of -1500 V, is applied between the first and the second plate. It is also possible to apply a voltage to the anode (A), which is placed behind the second detector plate. In this case the signal is taken from the output. The other possibility - which is common at SHIPTRAP - is to take the signal directly from the anode of the MCP. In this case the output A of the voltage divider is not connected to the anode of the MCP.

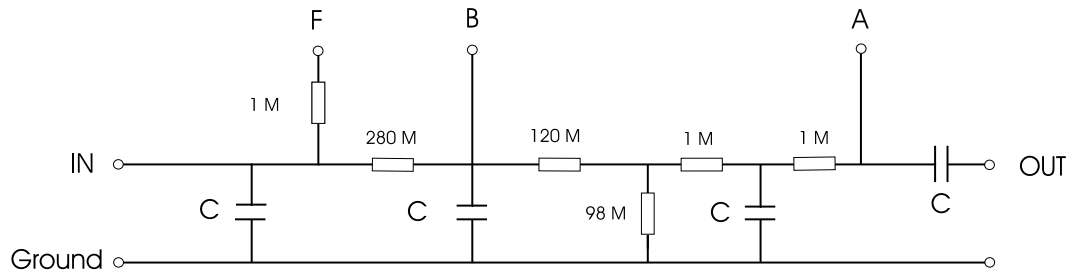

Figure 3.19: A sketch of the voltage divider to apply voltages to an MCP detector is shown. The input voltage is typically -3100 to -3200 V.

[10]Normally MCPs made of lead glass are chosen. In this material the normally used CaO is partly replaced by PbO, which leads to a high density and a high resistance.

Table 3.2: Comparison of characteristic parameters of Channeltron and MCP detector.

	Channeltron	MCP
Efficiency	90%-100%	25%-35%
Typical gain at 2.5 kV	$5 \cdot 10^7$	$5 \cdot 10^7$
Impedance	40 - 120 MΩ	66 - 400 MΩ
Working pressure	10^{-6} mbar	10^{-6} mbar
Dark count rate	< 0.05 Hz/cm^2	2 Hz/cm^2
Max. count rate	10^6	10^7 - 10^8 Hz
Pulse width / dead time	$\sim$ 25 ns	$\sim$ 2 ns
Rise time	$\sim$ 5 ns	$\sim$ 0.5 ns
Aperture plate size (radius)	5.6 mm	5 - 25 mm

The MCP signal is transferred to a multi-channel-scaler (MCS), which is triggered by a certain switch pulse. Like this the MCP detectors can be used to identify ions due to their time of flight. They are mounted on movable linear feedthroughs at the same stages as the silicon detectors: behind the buncher (MCP1), in front of (MCP2) and behind (MCP3) the magnet.

3.5.3 The Channeltron

The Channeltron has the same working principle as an MCP detector. It has only one big channel which is bent to guarantee that the ion hits the wall and creates an electron cascade as in the case of the MCP. The advantage is that nearly every ion which is entering the Channeltron creates an electron cascade. In the case of the MCP about 70% of the ions are lost because they hit the surface between two channels.

To attract the ions towards the Channeltron a voltage of -4000 V is applied to the entrance electrode. The Channeltron itself is operated at a voltage of -2000 V.

The characteristic parameters of Channeltron and MCP detector are compared in Tab. 3.2. Due to the higher detection efficiency it is in general more favorable to use the Channeltron instead of an MCP detector. Especially at SHIPTRAP, were nuclides with very low yields are being measured, it is crucial to make use of any gain factor which increases the overall efficiency. For this reason the Channeltron is mounted behind the MCP3. The MCP3 is mounted on a movable linear feedthrough and can be replaced by a lens in order to transport the ions to the Channeltron.

3.5.4 The position sensitive MCP detector

To obtain more detailed information about the ion motions in the Penning trap a position sensitive detector was tested at SHIPTRAP. A commercial delay-line detector (DLD40 from the company RoentDek Handels GmbH [Jagu2002, Roen]) was found suitable for this purpose. First experiments on Penning traps using this detectors were performed in the context of the diploma thesis of Georg Eitel [Eite2008, Eite2009].

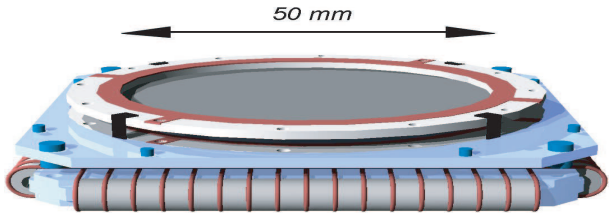

Figure 3.20: Layout of the delay-line detector.

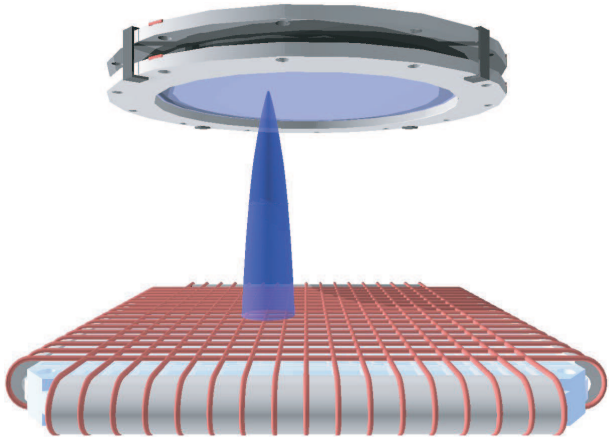

Figure 3.21: The operation principle of the delay-line detector is illustrated. The electron cascade from the anode is detected by a pair of wires to determine the position of the ion [Czas2004].

A sketch of the delay-line detector is shown in Fig 3.20. It consists of two microchannel plates (active diameter = 42 mm) which are isolated from each other with ceramic rings, the delay-line anode and one plate for fixation [Lamp1987, Czas2004]. The working principle of the MCP is described in Sec. 3.5.2. The additionally mounted delay-line anode provides information about the position of the detected particles. It consists of two pairs of wires which are wound on a ceramic core perpendicular to each other in x and y direction (see Fig 3.21). The anode is set on a potential of about +300 V with respect to the MCP output. The electron cascade from the MCP produces electric signals in the wires which propagate along the delay-line wires with the velocity v_{cable}[11]. Since the propagation velocity in one cable

[11] The propagation velocity in the wire is in the order of $2 \cdot 10^8$ m/s, which is 2/3 of the speed of light.

is constant the runtime of a signal gives information about the covered distance. The position in x direction can then be determined from the difference of the runtimes t_{x1} and t_{x2} of two signals in opposite direction according to

$$x = \frac{1}{2} v_{cable}(t_{x1} - t_{x2}). \tag{3.58}$$

The position in y direction is determined analogue. The runtimes are measured with a time-digital converter of the type TDC8HP which has a time resolution of 25 ps. The position resolution is determined by the time resolution and the uncertainty of the propagation velocity in the cable v_{cable}. For a single event a spatial resolution of 70 μm can be reached [Roen09]. The detector efficiency is about 30 to 40 % for low energetic ions.

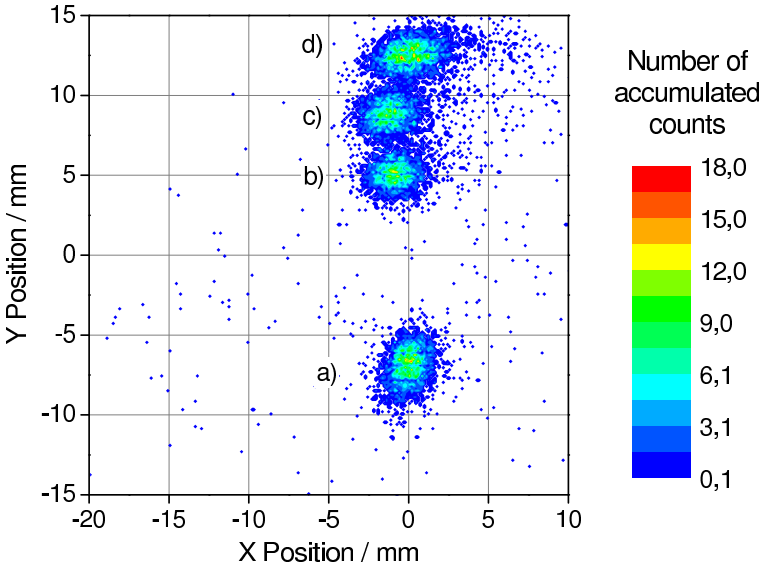

Figure 3.22: x-y-position measurement of the ejected ions from the Penning trap. The data has been recorded with the delay-line detector for different magnetron excitation times: (a) $T_{exc} = 0$, (b) $T_{exc} = 50$ ms, (c) $T_{exc} = 70$ ms and (d) $T_{exc} = 90$ ms.

In order to perform tests with trapped ions the delay-line detector was mounted at the SHIPTRAP setup behind MCP3 (see Fig. 3.1). The magnetic field at this position is smaller than 10 mT and thus does not influence the detection process.

Variation of the magnetron excitation time

In a first test ^{133}Cs ions from the reference ion source were centered in the measurement trap and excited by a dipolar RF field with an amplitude $V_{exc} = 0.4$ V at the magnetron frequency $\nu_- = 1355$ Hz. The excitation time T_{exc} was varied between zero and 100 ms. Cyclotron excitation was not applied. The total storage time in the measurement trap was kept constant in all cases in order to extract all ions at the same phase. The data acquisition of the delay-line detector was triggered by the ejection of the ions from the measurement trap. The time between two

measurements was one second.[12]

Figure 3.22 shows the picture obtained with the delay-line detector for four different magnetron excitation times. For each excitation time the data acquisition was performed for 20 minutes. The average count rate was around two ions per shot. If no magnetron excitation is applied the ions remain at their center position (a). It is obvious that the center of the detector does not coincide with the center of the beam. This is due to a small misalignment of the trap section. This misalignment could be corrected with a deflector which is mounted behind the magnet. This was, however, not done in this measurement.

With increasing excitation time T_{exc} the ions are moved away from their center position (a) to the positions (b) to (d). As expected theoretically (see Fig. 3.11) the radius r_- of the ion motion is increasing linearly with the excitation time T_{exc}.

Figure 3.22 is monitoring the ion cloud at a certain phase, which is kept constant as mentioned above. This is the reason why the ion clouds for the four different excitation times T_{exc} are in good approximation placed on a line. If the phase was varied between each measurement one would for excitation times T_{exc} larger than zero obtain circles around the center position (a).

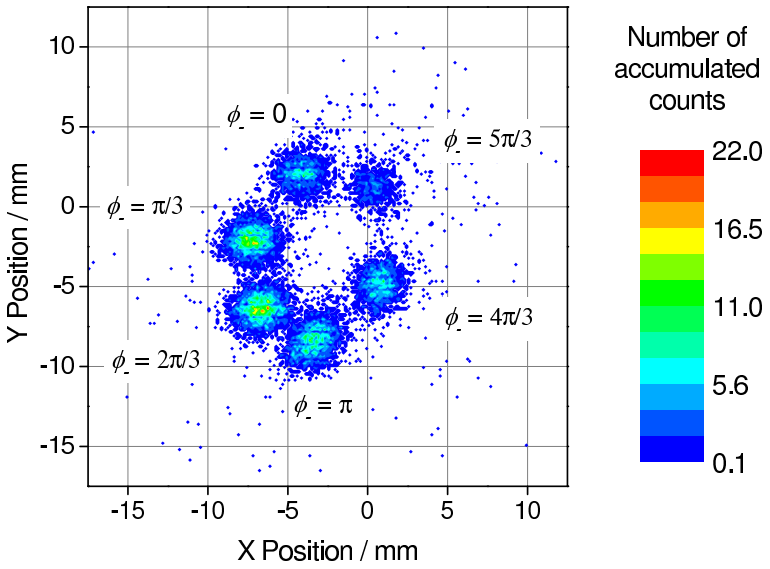

Figure 3.23: Ions recorded with the delay-line detector for six different magnetron phases Φ_-. The ejections of the ions from the measurement trap was delayed for different time intervals in order to vary the magnetron phase at the time of ejection.

[12] The measurement cycle will be explained in Sec. 4.2 using the example of the nobelium beamtime in 2008.

Monitoring the magnetron phase

The second measurement was performed with the aim to detect the positions of the ions for different magnetron phases. For this purpose the excitation time T_{exc} was kept constant to 50 ms. In this way all the ions are excited to the same radius of motion r_-. After the magnetron excitation a waiting time T_{wait} was introduced. This waiting time T_{wait} was varied in six steps from zero to $1/\nu_- = 738$ μs, which is the period of one magnetron motion. Within this time one revolution of the ions around their center position is expected. Since the time steps are shorter than one period it is possible to detect ions with different magnetron phases.

The crucial criterion for the position of an ion on the delay-line detector is its magnetron phase at the ejection time. Ions in different phases are thus found on different positions on the detector. In this way it is possible to monitor the magnetron phase of the ions by detecting their position. The result of this measurement is shown in Fig. 3.23. The dependence of the count rate on the magnetron phase is probably a result of a small asymmetry in the electromagnetic field between the measurement trap and the delay-line detector.

In this experiment the resolution for the magnetron radius was $\Delta r_- = 0.19$ mm and the phase resolution at a magnetron radius of $r_- = 1.2$ mm was $\Delta\phi_- = 8°$.

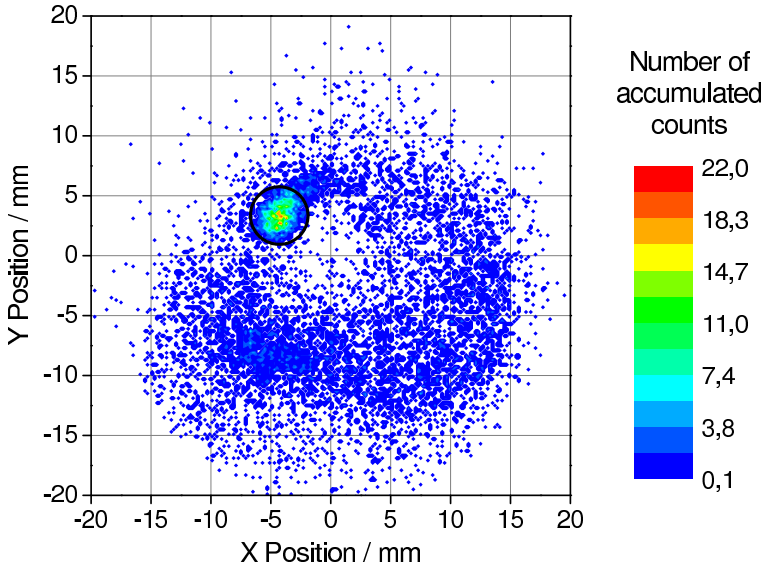

Figure 3.24: Spectrum taken with the delay-line detector for separation of $^{85}Rb^+$ and $^{87}Rb^+$. The two isotopes are excited at the resonance frequency of $^{85}Rb^+$. The spot enclosed with a black cycle corresponds to $^{87}Rb^+$ ions, which have a small radial energy since they are not excited and thus still perform magnetron motion.

Isotope separation

In a third measurement the two rubidium isotopes $^{85}Rb^+$ and $^{87}Rb^+$ were stored simultaneously in the measurement trap. This was achieved by exciting both species at their cyclotron frequencies in the preparation trap. This excitation was performed with a dipolar RF field which leads to a simultaneous centering of the two isotopes. After the transfer to the measurement trap the two isotopes were excited to the same magnetron radius by dipolar excitation. The excitation was performed at the magnetron frequency $\nu_- = 1337$ Hz with an excitation time of $T_{exc} = 50$ ms. Then the ions were excited with a quadrupolar RF field with the cyclotron frequency of $^{85}Rb^+$, $\nu_c(^{85}Rb^+) = 1.266$ MHz. The cyclotron excitation was performed with an excitation time of $T_{exc} = 100$ ms. In this way the $^{85}Rb^+$ ions were converted from magnetron into cyclotron motion, while the $^{87}Rb^+$ ions - which are not excited - remained performing pure magnetron motion. After the cyclotron excitation the ions were ejected from the measurement trap. The result is shown in Fig. 3.24.

In case of the $^{87}Rb^+$ one expects a small spot oscillating around the center position with the magnetron frequency ν_-. Since the total storage time is kept constant the $^{87}Rb^+$ ions are ejected with fixed magnetron phase. The $^{85}Rb^+$ ions are, however, oscillating with the cyclotron frequency ν_c, which is three orders of magnitude higher than the magnetron frequency and has a period of less than one μs. This is shorter than the rising time of the HV switches used to open the measurement trap. The information about the cyclotron phase thus gets lost during the extraction process. For this reason the ions are expected to be spread over a circle around the center. Hence, the small spot with a high amount of events in Fig. 3.24 is assigned to consist mainly of $^{87}Rb^+$ ions, while the background is identified as $^{85}Rb^+$ ions.

The evidence for this assumption can be obtained from a time-of-flight analysis. Figure 3.25 shows two clearly separated peaks with a time-of-flight difference of about 15 μs. The peak with the longer time of flight is corresponding to the ions in the small spot, the peak with the smaller time of flight to the cyclotron excited ions. This is in agreement with the previous assumption since the $^{85}Rb^+$ ions are performing cyclotron motion and thus have a shorter time of flight. The non-excited $^{87}Rb^+$ which are performing magnetron motion have a higher time of flight.[13]

Furthermore, the intensity ratio of the two peaks is in agreement with the natural abundance ratio of the two rubidium isotopes (^{85}Rb: 72.2%, ^{87}Rb: 27.8%). It is thus proved that it is possible to identify different isotopes due to an analysis of the position distribution of an ion ensemble.

One benefit of this method is the identification of contaminant ions while taking a time-of-flight resonance curve (see Sec. 3.4.5). In a time-of-flight resonance it is not possible to distinguish two ion species of approximately the same mass since their time of flight is similar and the time-of-flight resolution is too small. The delay-line detector can thus be a very useful tool to identify a contamination by evaluating a position resolved spectrum. This was also demonstrated with the two rubidium isotopes $^{85}Rb^+$ and $^{87}Rb^+$.

[13] If both species were not excited one also would expect a difference in time of flight due to the different mass. This difference can, however, not be resolved for ions extracted from the measurement trap.

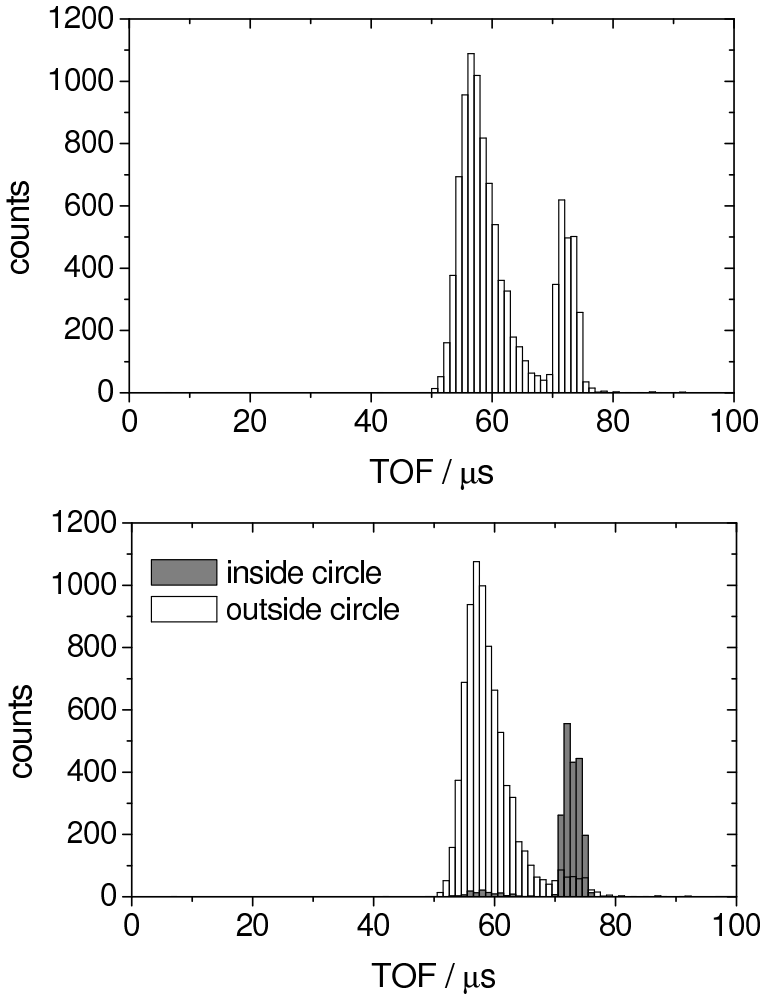

Figure 3.25: The time-of-flight spectrum corresponding to Fig. 3.24 is shown. (a) shows the overall time-of-flight distribution and (b) the time-of-flight distributions for the ions inside (grey bars) and outside (white bars) the marked area. The peak with the smaller time of flight corresponds to $^{85}Rb^{+}$ and the peak with the higher time of flight to $^{87}Rb^{+}$.

As in the previous measurement both isotopes were transported to the measurement trap. Then a time-of-flight resonance curve was taken for $^{85}Rb^{+}$, while $^{87}Rb^{+}$ remained unexcited. The resonance curve of $^{85}Rb^{+}$ is shown in Fig. 3.26(top). The TOF-effect (see Sec. 3.4.5) is determined to be 16%. Figure 3.27 shows the corresponding picture from the delay-line detector which is similar to Fig. 3.24.[14] The non-excited ions are located around the position (x = -2 mm, y = 16 mm). After setting a cut window for all events in a diameter of 10 mm around this position and recalculating the mean time of flight, the TOF-effect is increased to 22% (see Fig. 3.26(bottom)). By neglecting the ions in the spot not only the $^{87}Rb^{+}$ ions get lost, but also about 50% of the $^{85}Rb^{+}$ ions (the ones which were not excited).

[14]The only difference between Fig. 3.24 and Fig. 3.27 is that in the first case the $^{85}Rb^{+}$ ions are excited with a fixed excitation frequency ν_{exc} which is equal to the cyclotron frequency ν_c of $^{85}Rb^{+}$. In the second case this excitation frequency ν_{exc} is varied in the vicinity of $\nu_c(^{85}Rb^{+})$, as requested for a time-of-flight resonance (see Sec. 3.4.5).

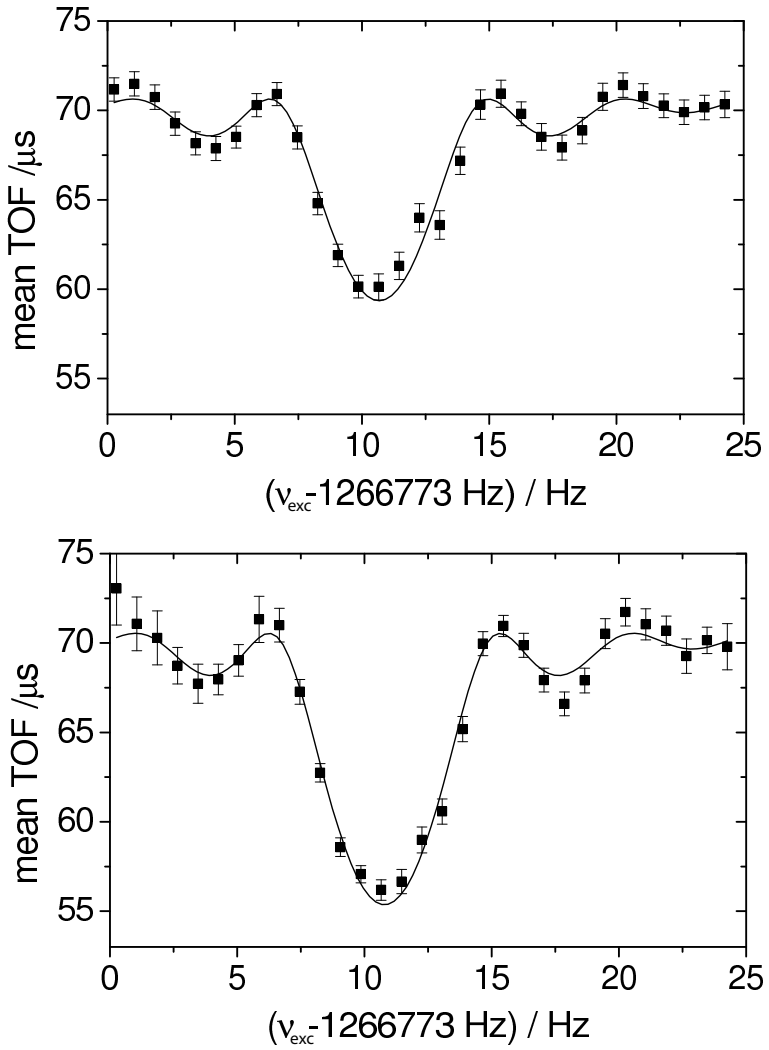

Figure 3.26: The time-of-flight resonance for $^{85}Rb^{+}$ with additionally trapped $^{87}Rb^{+}$ acting as a contamination is shown for all recorded events (top) and with neglecting the events in the black circle of Fig. 3.27 (bottom). The solid line is a fit of the theoretical line shape to the experimental data. The increase in the time-of-flight contrast is obvious.

The uncertainty of the cyclotron frequency determination decreases, however, by almost 40%, corresponding to a factor of two in statistics and thus a factor of two in measurement time, which is a big improvement.

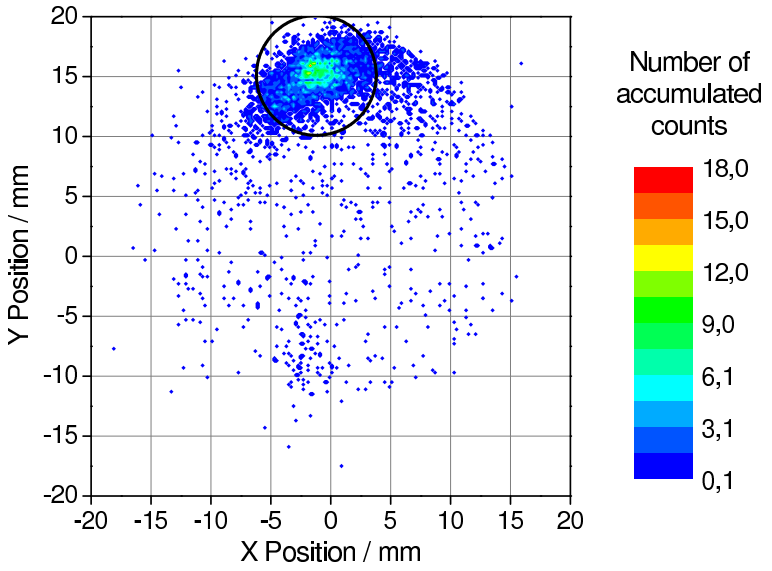

Figure 3.27: Spectrum recorded with the delay-line detector in a TOF-ICR measurement with $^{85}Rb^{+}$ ions and $^{87}Rb^{+}$ ions trapped simultaneously in the measurement trap. The black circle marks the events that are neglected in the time-of-flight analysis of the resonance shown in Fig. 3.26(b).

4 Mass measurements on nobelium and lawrencium

The SHIPTRAP facility (see Chap. 3), which provides the possibility to perform direct mass measurements with the time-of-flight cyclotron resonance method (see Sec. 3.4.5), has delivered valuable results for radionuclides with mass numbers between $A \approx 80-150$ since 2005 [Raha2005, Raut2006]. The achieved relative precision was in the range of a few 10^{-8}. The focus was then set on heavier masses with the aim to demonstrate that despite the very low production rates in this region a high precision in mass determination can still be reached.

During a SHIPTRAP experiment in August 2008 the masses of the three nobelium isotopes ^{252}No, ^{253}No and ^{254}No have been measured directly for the first time. With this experiment the Penning trap method could be established in the region of very heavy elements, which could before not be addressed with this mass measurement technique. It was possible to perform studies on species with a production rate of one ion per second and less. Besides the quest for information on the island of stability this is a remarkable achievement in terms of extending the limits of Penning trap mass spectrometry.

In addition this experiment provides an independent confirmation and improvement of previous mass values based on the determination of α-decay energies. The results of this experiment also influence the mass values of several other nuclides in the region of superheavy elements, which are linked to them via α-decay chains.

This chapter first gives an overview of the mechanism in which the nobelium isotopes are produced (see Sec. 4.1). In addition a description of the measurement cycle at SHIPTRAP is given (see Sec. 4.2). After the discussion of the new results obtained with SHIPTRAP (see Sec. 4.3) the previous mass determination on nobelium from α-decay energies are presented (see Sec. 4.4) and compared to the new ones (see Sec. 4.5). The new results are also compared to the theoretical predictions (see Sec. 4.6). A first mass measurement on the next heavier element lawrencium is described in Sec. 4.7.

4.1 The production of superheavy elements

The cross sections for the production of superheavy elements are extremely low, for example about one atom per week for $Z = 112$ with a production cross section of about 1 pb. For $92 < Z \leq 100$ nuclides can still be produced in high flux reactors by successive neutron capture and subsequent β^- decay. The limit of this production method is set by the half-life of ^{258}Fm due to spontaneous fission, which is $T_{SF} = 0.3$ ms, and the β^- decay branches, which are negligible compared to other

decay channels for all known fermium isotopes. Thus, to produce elements with $Z \geq 100$ one has to use other production mechanisms. The only applicable method to exceed $Z = 100$ is the use of complete fusion reactions. The choice of projectile and target is crucial for the production cross section and has to be optimized for each nuclide. The theoretical description of the production process of superheavy elements is briefly discussed in Sec. 4.1.1. Experimental results, especially for the reactions for the production of the nuclides investigated in this thesis, are then given in Sec. 4.1.2.

4.1.1 Theoretical description of the production of SHE

The cross section σ_x for the production of a certain nucleus can be written as [Ogan2007]

$$\sigma_x(E_x) = \sigma_{CN}(E_x) \cdot P_x(E_x), \tag{4.1}$$

where σ_{CN} is the cross section for the formation of the compound nucleus and P_x the probability of its survival. Both are functions of the excitation energy E_x of the compound nucleus and the angular momentum. The total energy before the collision is given by the ground state energies of projectile and target, M_P and M_T, and the energy E_{beam} of the projectile beam[1]. The total energy after the collision consists of the ground state energy of the compound nucleus M_{CN} and its excitation energy E_x. By equating the expressions for the total energies before and after the collision one obtains

$$M_P + M_T + E_{beam} = E_x + M_{CN}. \tag{4.2}$$

The Coulomb barrier B_C is defined as the beam energy for which the fusion probability is 50%. The corresponding excitation energy is called $E_{x,min}$. Due to the classical conception $E_{x,min}$ can be regarded as minimum excitation energy which is obtained if the beam energy E_{beam} is equal to the Coulomb barrier B_C:

$$M_P + M_T + B_C = E_{x,min} + M_{CN}. \tag{4.3}$$

By defining the Q value as $Q = M_{CN} - (M_P + M_T)$ the minimum excitation energy of the compound nucleus can be expressed as

$$E_{x,min} = B_C - Q. \tag{4.4}$$

The minimum excitation energy $E_{x,min}$ is thus dependent on the ground state masses of the projectile and target nuclides.

In reality fusion is also observed for $E_{beam} < B_C$, however with steeply decreasing fusion probability resulting in a smaller cross section σ_{CN}. For $E_{beam} > B_C$ the cross section σ_{CN} is increasing. The limiting factor is, however, the survival probability $P_x(E_x)$. It is decreasing rapidly for high excitation energies E_x, which are the result of high beam energies E_{beam}. The compound nucleus dissipates its excitation energy by emission of particles or γ rays. In the region of heavy nuclei prompt fission dominates as the compound nucleus decay mode already at low excitation energies resulting in a survival probability $P_x(E_x) \ll 1$. Since the probability to

[1]The beam energy is here defined in the center of mass system.

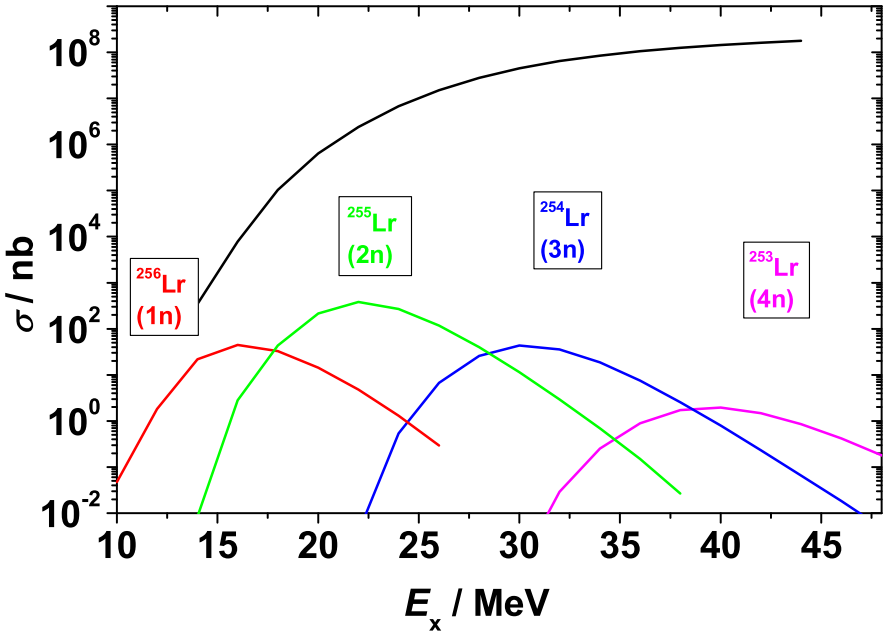

Figure 4.1: The fusion process is illustrated due to the example of the calculated cross sections for the reaction ^{48}Ca+^{209}Bi resulting in the lawrencium isotopes $^{253-256}$Lr. The calculations have been performed with HIVAP [Reis1992]. The cross sections are plotted as a function of the excitation energy E_x of the nucleus. The black line represents the fusion cross section σ_{CN}, which is increasing with the excitation energy E_x. This value, however, has to be multiplied with the survival probability $P_x(E_x)$. The resulting cross sections σ_x for the individual reaction products are plotted with different colours.

decay by prompt fission is increasing rapidly with increasing excitation energies the maximum production cross sections for heaviest nuclei are governed by a delicate balance between fusion probability and fission probability. The maximum of the production cross section is usually located at $E_x < E_{x.min}$.

Figure 4.1 shows calculated cross sections for the reaction ^{48}Ca+^{209}Bi as an example. Although the cross section σ_{CN} for the formation of the compound nucleus is increasing with increasing excitation energy E_x the production cross sections σ_x of the several lawrencium isotopes are decreasing for high excitation energies E_x.

The increased stability of the superheavy elements is explained by increased spontaneous fission half-lives due to increased shell effects (see Chap. 2). The height of the fission barrier of the compound nucleus is thus a crucial parameter in the production of superheavy elements.

A combination of beam and target nuclei with closed neutron or proton shells also leads to a decrease in E_x. Furthermore, superheavy elements need a much higher neutron excess $N - Z$ than lighter ions. This can be explained by the increasing

Coulomb repulsion of the protons which results in a drastic decrease of the spontaneous fission half-life T_{SF}. Fusion products from stable projectiles and targets will thus always have a comparatively small neutron excess. Using neutron-rich unstable projectiles could overcome this problem, but has the disadvantage that it is very difficult to reach high beam currents. One good choice for a projectile nuclide is ^{48}Ca which is a neutron rich stable nuclide with 20 protons and 28 neutrons. For the production of nobelium lead has then to be chosen as a target. The maximum cross sections are observed for the evaporation of one to three neutrons (see Sec. 4.1.2). For even higher Z the cross sections are decreasing very rapidly with Z - at least in cold fusion reactions.

4.1.2 Production of nobelium isotopes at SHIP

The nobelium isotopes which are discussed in this work were produced at SHIP (see Sec. 3.1) using ^{48}Ca as projectile and the lead isotopes $^{206-208}$Pb in molecular combination with sulfur as target. For each nobelium isotope the optimum reaction to obtain the highest cross section had to be determined experimentally. This was done by measuring the excitation function for the given reaction [Gägg1989, Belo2003].

The excitation function is the dependence of the cross section σ_x as a function of the excitation energy E_x or the beam energy E_{beam}, respectively. It is obvious that the energy E_{beam} of the projectile beam is directly influencing the excitation energy E_x of the nucleus and is therefore a characteristic parameter for the formation of the nucleus.

Figure 4.2 shows the excitation functions for the reaction ^{48}Ca+^{208}Pb. In this case the nobelium isotope ^{254}No is produced with a cross section of about 1.8 μb for the evaporation of two neutrons. The other two isotopes, ^{253}No and ^{255}No, have in this case cross sections which are about one order of magnitude lower than the one of ^{254}No. Obviously this reaction is only optimal for the production of the isotope ^{254}No. With other projectile-target combinations it is possible to produce also other nobelium isotopes with cross sections that are higher than the ones with the reaction ^{48}Ca+^{208}Pb. To obtain the isotope ^{253}No with comparably high count rate one has to chose the reaction ^{48}Ca+^{207}Pb. Also for ^{252}No the 2n channel was found to be the optimum. In this case ^{206}Pb has to be used as a target. The target has thus to be changed for each nobelium isotope one wants to obtain. In principle all four stable lead isotopes can be used as targets.[2]. The cross section for the production of nobelium is, however, decreasing with decreasing neutron number N. The highest cross section of 1.8 μb is obtained for the reaction ^{48}Ca+^{208}Pb. In this case projectile and target are both doubly-magic nuclei.

Apart from the reactions using ^{48}Ca as projectile also other reactions are thinkable, e.g. using carbon beam and a curium target. However, in this case the recoil energy is very small and only a small part of the evaporation residues would enter the gas cell window foil. In addition, the reaction calcium on lead delivers a higher cross section.

[2]The natural abundances of the four stable lead isotopes are: ^{204}Pb: 1.4(1)%^{206}Pb: 24.1(1)%, ^{207}Pb: 22.1(1)% and ^{208}Pb: 52.4(1)%

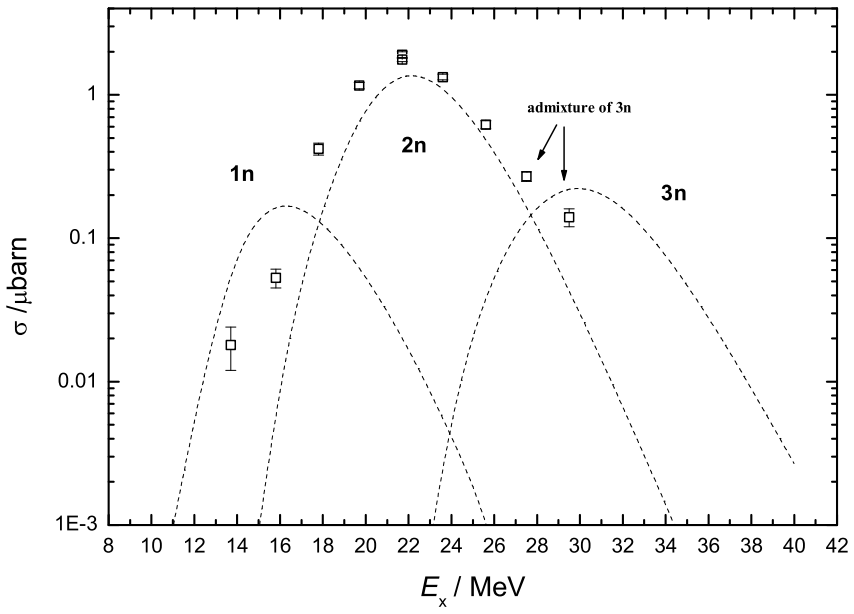

Figure 4.2: The excitation function for the reaction ^{48}Ca+^{208}Pb resulting in the nobelium isotopes $^{253-255}$No is shown for one, two and three evaporated neutrons. The white squares are experimental data points measured at SHIP and give the sum cross section for all three nobelium isotopes. The dashed lines are theoretical calculations with HIVAP. The maximum cross section for ^{254}No (1.8 μb) is experimentally obtained for an excitation energy of 21.7 MeV. This energy value is referring to reaction products that are produced in the center of the target.

For the production of the element lawrencium (which has the proton number $Z = 103$) with ^{48}Ca beam bismuth (Bi_2O_3) has to be chosen as a target. Since bismuth has only one stable isotope[3] the number of lawrencium isotopes which can be produced with a sufficiently high cross section ($\sigma > 100$ nb) is limited to only one. Figure 4.3 shows the excitation function for the reaction ^{48}Ca+^{209}Bi. Like in the case of the production of nobelium the maximum cross section is obtained for the 2n channel, corresponding to the isotope ^{255}Lr. The neighbouring isotopes are produced with cross sections which are about one order of magnitude lower. A possibility for the production of further lawrencium isotopes using a bismuth target is choosing ^{44}Ca or ^{46}Ca as projectiles. In these cases, however, the cross sections are also much lower.

After determining the optimum target nuclide and beam energy E_{beam} for the production of a certain nobelium isotope, it is necessary to find the right settings of the velocity filter. The nobelium ions are produced with a certain energy distribution. The energy of a nuclide is dependent on the place in the target foil where it was produced. In addition, due to scattering in the target and neutron emission, not all

[3]The isotope ^{209}Bi has a half-life of 19 $\cdot 10^{18}$ years and can thus be regarded as nearly stable.

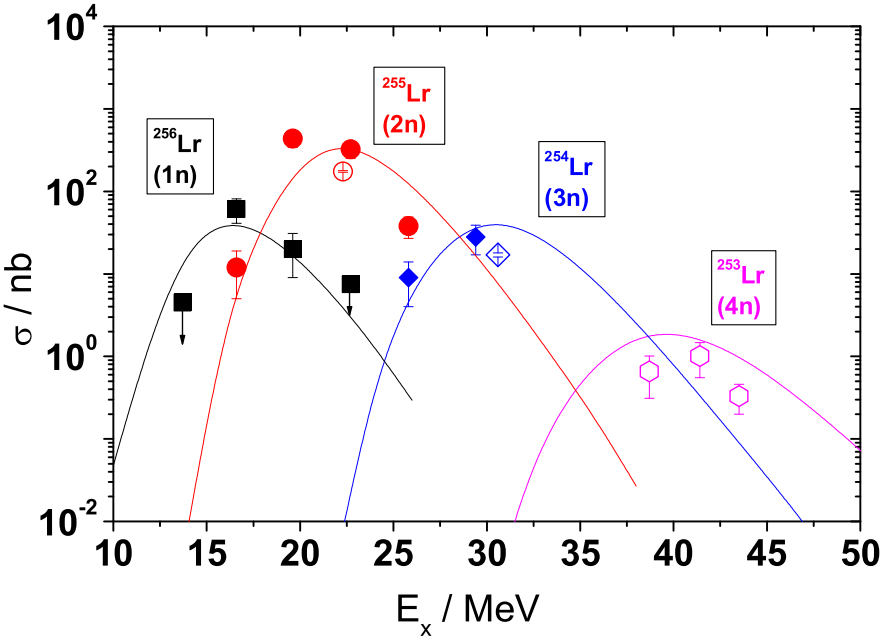

Figure 4.3: The excitation function for the reaction ^{48}Ca+^{209}Bi resulting in the lawrencium isotopes $^{253-256}$Lr is shown for one, two, three and four evaporated neutrons. The experimental data points measured at SHIP are represented by squares, circles, diamonds and hexagons, respectively. The filled data points have been measured in 1989 [Gägg1989], the open ones are recent measurements. The solid lines are theoretical calculations with HIVAP. The maximum cross section for ^{255}Lr (450 nb) is experimentally obtained for an excitation energy of 19.6 MeV, which may have been a fluctuation due to poor statistics. According to recent measurements aiming at investigations of the decay properties of the lawrencium isotopes $^{254-256}$Lr [Anta2008] the value of 22.5 MeV is chosen, which leads to a cross section of about 200 nb.

the nuclides have the same direction. Since the velocity filter has a limited angular and velocity acceptance the settings cannot be chosen in a way that all nobelium nuclides are transported to the SHIPTRAP stopping cell. It is necessary to determine the velocity distribution of the nobelium nuclides and then choose the settings to transport the maximum number of nuclides. The mean velocity can be expected around the velocity v_{CN} of the compound nucleus, which has to be corrected for the energy loss in the target. This was verified experimentally for ^{254}No (see Fig. 4.4).

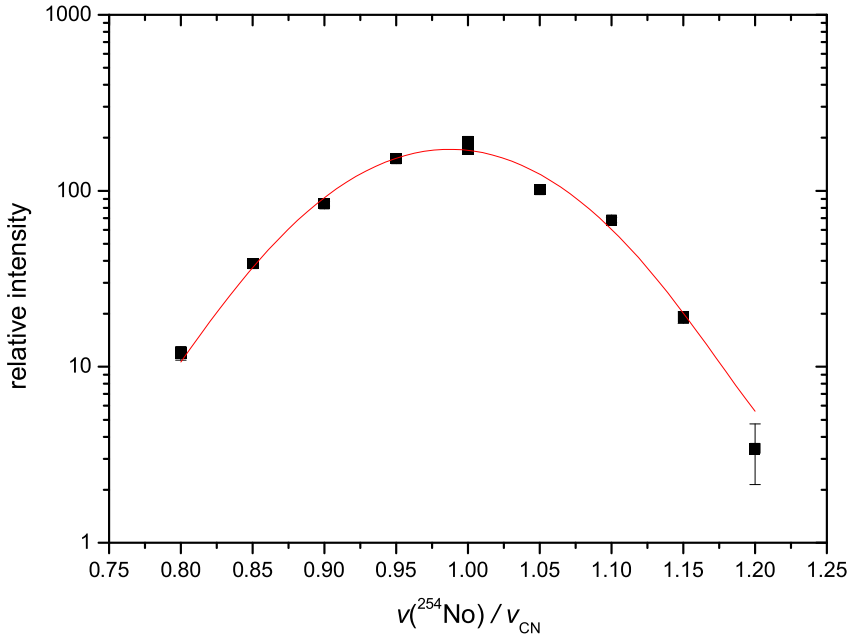

Figure 4.4: The velocity distribution of the nobelium isotope ^{254}No measured at SHIP is shown. The number of events are plotted as a function of the velocity ratio $v(^{254}\mathrm{No})/v_{CN}$. The point at maximum intensity was measured twice.

4.2 The nobelium mass measurement procedure

The nobelium isotopes were decelerated in the gas cell which was kept at a pressure of 50 mbar. A titanium foil with a thickness of 2.5 μm was chosen as entrance window. In addition a mylar foil with a thickness of 1.5 μm was added in front of the gas cell entrance window with a distance of about 30 cm to the titanium foil for optimum stopping. The nobelium nuclides were extracted from the gas cell mainly as doubly-charged ions. The DC and RF voltages used during the beamtime are shown in Tab. 4.1. The helium pressure in the buncher was chosen to be 5 $\cdot 10^{-3}$ mbar, the helium pressure in the PT was 1.5 $\cdot 10^{-6}$ mbar. The nobelium ions were detected behind the measurement trap with a Channeltron detector to make use of its high detecting efficiency close to 100%.

The timing cycle is shown in Fig. 4.5 starting with the pulse (30 μs) for extracting the ions from the RFQ buncher. After a delay of about 50 μs the ions reach the preparation trap, which is opened for a length of 30 μs to let the ions enter the trap. During a waiting time of 200 ms the axial motion of the ions is cooled by collisions with the buffer gas. Then the ions are excited with a dipolar RF field at the magnetron frequency for 25 ms. The subsequent quadrupolar excitation at the cyclotron frequency ν_c with a duration of 200 ms is applied for centering the ions due to buffer gas cooling (see Sec. 3.4.4). After an additional waiting time of

Table 4.1: The DC and RF voltages of gas cell and buncher used during the nobelium beamtime in August 2008.

GC DC 1	210 V
GC DC 2	180 V
GC DC 3	150 V
GC DC 4	120 V
GC DC 5	90 V
Funnel DC max	40 V
Funnel DC min	30 V
Funnel RF amplitude	200 V_{pp}
Nozzle	19 V
Extraction RFQ DC max	12 V
Extraction RFQ DC min	3 V
Extraction RFQ RF amplitude	320 V_{pp}
Buncher linear slope DC max	2 V
Buncher linear slope DC min	-10 V
Buncher segment 31 and 32 DC	-11 V switched 60 to V
Buncher segment 33 DC	-12 V
Buncher segment 34 DC	2 V switched to -80 V
Buncher RF amplitude	100 V_{pp}

10 ms, which is introduced for cooling the remaining cyclotron motion, the ions are transferred to the measurement trap by switching the exit voltages of the PT and the entrance voltages of the MT simultaneously down for about 40 μs. After the ions are trapped in the MT they are again excited for 20 ms with dipolar excitation at the magnetron frequency to a typical motional radius of 0.7 mm. The subsequent cyclotron excitation time was varied during the experiment. In most of the cases T_{exc} = 900 ms was chosen. After the cyclotron excitation an additional waiting time is introduced which has to be adjusted in order to extract with the correct magnetron phase. With the last pulse of 200 μs the MT is opened to eject the ions from the trap and the multi-channel-scaler (MCS) is triggered.

For the isotope with the highest yield, ^{254}No, from about 1 ion per second entering the gas cell, about one to two ions per minute were detected with the Channeltron detector corresponding to an overall efficiency of 1-2%. Thus, measurement times of two to four hours for recording one time-of-flight cyclotron resonance were required.

$^{133}Cs^{+}$ was chosen as reference mass since its q/m ratio is about the same as the one of the doubly-charged nobelium ions. The frequencies were measured with the time-of-flight ion cyclotron resonance detection technique (see Sec. 3.4.5). Figure 4.6 shows the devolution of the cyclotron frequency of $^{133}Cs^{+}$ as a function of time during the experiment. One can clearly see periodical oscillations that are due to temperature changes inside the bore of the magnet between day and night. The nobelium isotopes were measured as doubly charged ions. Figure 4.7 shows a time-of-flight resonance of $^{254}No^{2+}$ as an example. The increased q/m ratio leads to a

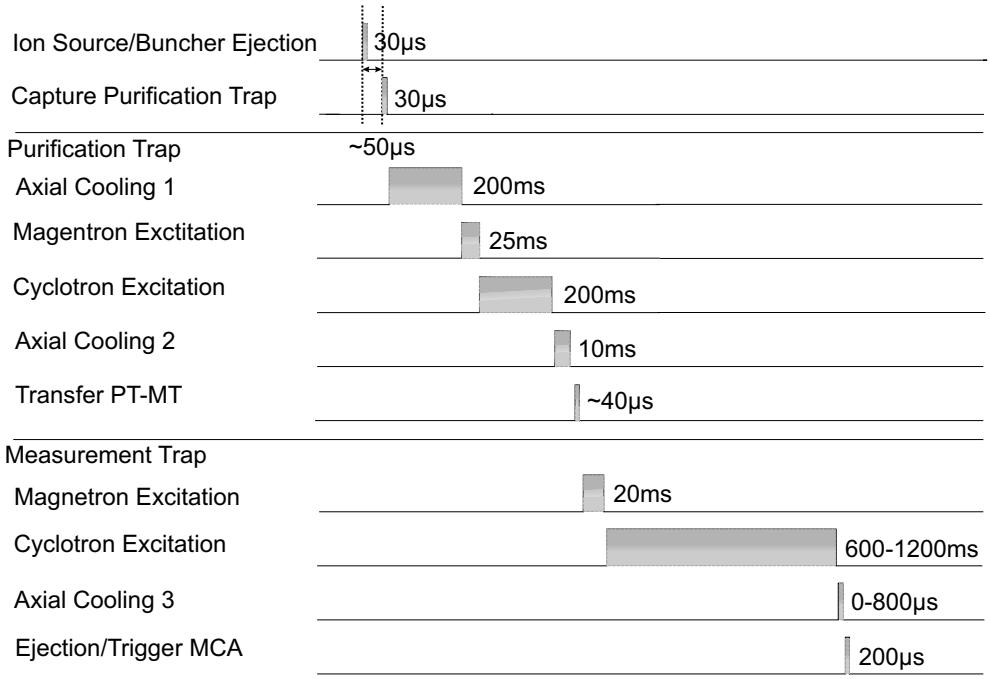

Figure 4.5: The measurement cycle at SHIPTRAP for the nobelium beamtime is illustrated. Further details are given in the text.

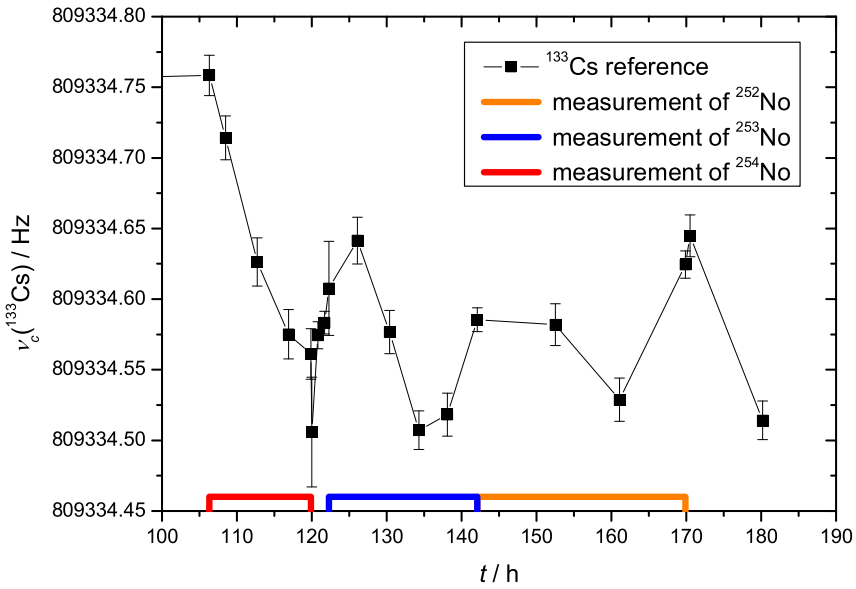

Figure 4.6: Variation of the cyclotron frequency of $^{133}Cs^{+}$ due to magnetic field fluctuations during the nobelium beamtime are shown. The time periods when the resonances of the three nobelium isotopes were taken are marked with different colours.

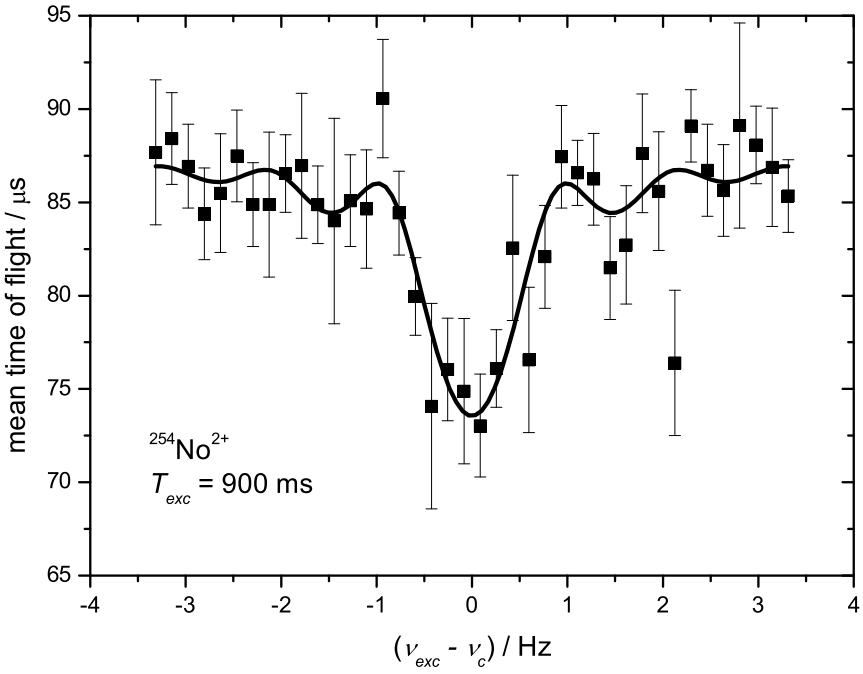

Figure 4.7: Time-of-flight resonance of $^{254}No^{2+}$ taken during the beamtime of August 2008. The excitation time is $T_{exc} = 900$ ms. The solid line is a fit of the theoretical line shape to the experimental data points [Köni1995]. The cyclotron frequency was determined to be $\nu_c = 846665.281(51)$ Hz.

higher cyclotron frequency and thus to a smaller relative uncertainty of the mass determination for the same measurement time in comparison to singly charged ions.

4.3 Results of the mass measurement on nobelium isotopes

The data analysis was performed according to the methods described in [Kell2003]. Before and after every nobelium measurement a time-of-flight resonance of the reference ion ^{133}Cs was taken. Every measurement - nobelium or caesium - is characterized by the point of time it was taken. This time t_i $(i = 1, 2)$ is determined as the mean value of the starting time and the end time:

$$t_i = \frac{t_{i,end} + t_{i,start}}{2}. \tag{4.5}$$

t_1 and t_2 are the times of the ^{133}Cs measurements which were taken before and after the nobelium measurement. t_m is the time when the nobelium measurement was taken. The cyclotron frequency $\nu_{c,ref}(t_m)$ of the reference ion at the time t_m is then linearly interpolated from the two measured cyclotron frequencies $\nu_{c,ref}(t_1)$

and $\nu_{c,ref}(t_2)$ according to

$$\nu_{c,ref}(t_m) = (\nu_{c,ref}(t_2) - \nu_{c,ref}(t_1)) \cdot \frac{t_m - t_1}{t_2 - t_1} + \nu_{c,ref}(t_1). \tag{4.6}$$

Its uncertainty is given by the expression

$$\delta\nu_{c,ref}(t_m) = \sqrt{\left(\delta\nu_{c,ref}(t_1) \cdot \frac{t_2 - t_m}{t_2 - t_1}\right)^2 + \left(\delta\nu_{c,ref}(t_2) \cdot \frac{t_m - t_1}{t_2 - t_1}\right)^2}. \tag{4.7}$$

The frequency ratio r between the reference mass and the mass of interest is

$$r = \frac{\nu_{c,ref}(t_m)}{\nu_c} \tag{4.8}$$

with the statistical uncertainty

$$\delta r_{stat} = r \cdot \sqrt{\left(\frac{\delta\nu_{c,ref}(t_m)}{\nu_{c,ref}(t_m)}\right)^2 + \left(\frac{\delta\nu_c}{\nu_c}\right)^2}. \tag{4.9}$$

The uncertainty is corrected by the time dispersion of the magnetic field $\frac{\delta B}{B} \cdot \frac{1}{\delta t} = 7 \cdot 10^{-9}/h$.[4] The residual uncertainty of a single measurement is then given by

$$\delta r_{res} = \sqrt{\delta r_{stat}^2 + \left((t_2 - t_1) \cdot \frac{\delta B}{B} \cdot \frac{1}{\delta t} \cdot r\right)^2}. \tag{4.10}$$

The weighted average of n measurements is given as:

$$\overline{r} = \frac{\sum_n r_n/\delta r_{res,n}^2}{\sum_n 1/\delta r_{res,n}^2} \tag{4.11}$$

with a statistical uncertainty

$$\delta\overline{r}_{stat} = \sqrt{\frac{1}{\sum_n 1/\delta r_{res,n}^2}}. \tag{4.12}$$

This uncertainty is corrected by adding a systematic error $\epsilon_{syst} = 4.2 \cdot 10^{-8}$ in the following way:

$$\delta\overline{r}_{total} = \sqrt{\delta\overline{r}_{stat}^2 + (\epsilon_{syst} \cdot \overline{r})^2}. \tag{4.13}$$

For the isotope ^{252}No altogether three resonances were taken, two with $T_{exc} = 200$ ms and one with $T_{exc} = 900$ ms. The results of the individual measurements are shown in Fig. 4.8. Since the production cross section of ^{252}No was very low (about 400 nb) only one ion in five to six minutes could be detected on the Channeltron detector. Because of the low count rate only events with less than three ions per

[4] This value was chosen according to recent measurements.

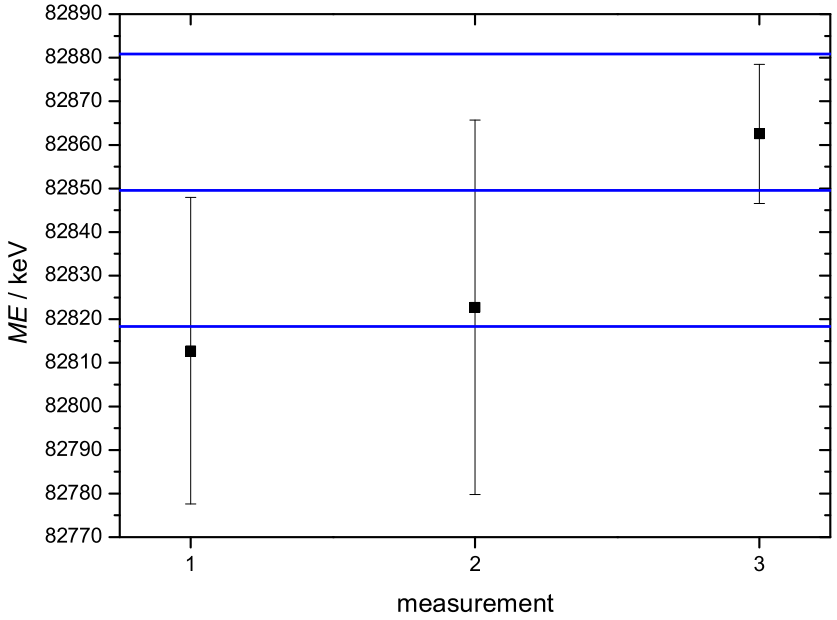

Figure 4.8: The results for the mass excesses of the individual measurements of the nobelium isotope ^{252}No are shown. The blue lines mark the average value and its uncertainty.

shot were taken into account for the fitting of the resonances. Events with more ions per shot are very likely not caused by nobelium ions but by detector noise. The influence of the isomeric contamination can be excluded since the isomeric state in ^{252}No (E_{exc} = 1254 keV) has a half-life of $T_{1/2}$ = 110(10) ms [Suli2007] and thus already decayed during the preparation process. The ground state has a half-life of $T_{1/2}$ = 2.44(4) s. The identification of ^{252}No is thus unambiguous.

The results are shown in Tab. 4.2. The values obtained from the three resonances agree with each other and with the AME value which is based on Q_α measurements (see Sec. 4.4). The frequency ratio was determined to be $\overline{r}$ = 0.94837677(13). This leads to a mass excess of ME = 82849(31) keV. The uncertainty of the reference mass ^{133}Cs with 22 eV [Audi2003] can be neglected.

In the case of the isotope ^{253}No one resonance with T_{exc} = 200 ms and four resonances with T_{exc} = 900 ms were recorded. The cross section was here a factor of two higher than in the case of ^{252}No, namely about 1 μb. The half-life of this isotope is $T_{1/2}$ = 1.62(15) min. The values obtained from the fitting of the five resonances are in perfect agreement with each other (see Fig. 4.9). The frequency ratio is $\overline{r}$ = 0.952144941(51), which leads to a mass excess of ME = 84356(13) keV. The half-lifes of the isomeric states in the isotope ^{253}No are shorter than one ms [Hess2007a]. The isomers are thus already decaying in the buncher and have therefore no influence on the measurement.

The isotope ^{254}No had the highest yield of the three isotopes under investigation

Table 4.2: The results from the measurement on the three nobelium isotopes are shown. The investigated nuclide and its half-life are given in the first and second column. The third and fourth column show the results for the corrected frequency ratio $\overline{r}$ and the mass excess ME obtained from the SHIPTRAP experiment. The uncertainties are obtained as discussed in the text. The fifth column shows the cross section and the last column the number of resonances which were recorded for each isotope.

Isotope	$T_{1/2}$	$\overline{r}$	ME / keV	cross section	resonances
^{252}No	2.44(4) s	0.94837677(13)	82849(31)	400 nb	3
^{253}No	1.62(15) min	0.952144941(51)	84356(13)	1 μb	5
^{254}No	51(10) s	0.955908553(58)	84733(14)	1.8 μb	4

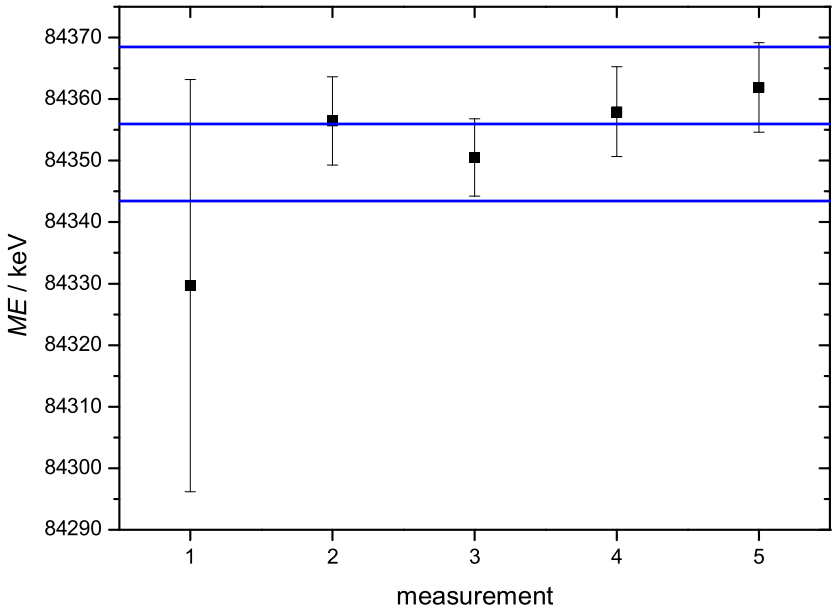

Figure 4.9: The results for the mass excesses of the individual measurements of the nobelium isotope ^{253}No are shown. The blue lines mark the average value and its uncertainty.

with a cross section of about 1.8 μb. This isotope has a long-lived isomeric state with a half-life of $T_{1/2}$ = 266(2) ms [Herz2006]. The half-life of the ground state is $T_{1/2}$ = 51(10) s. Also here one can assume that all the nuclides produced in the isomeric state already decayed during the preparation process, which lasts more than one second. The resonances were taken with a count rate of about one to two ions per minute. Altogether four resonances were taken for this isotope, one with T_{exc} = 200

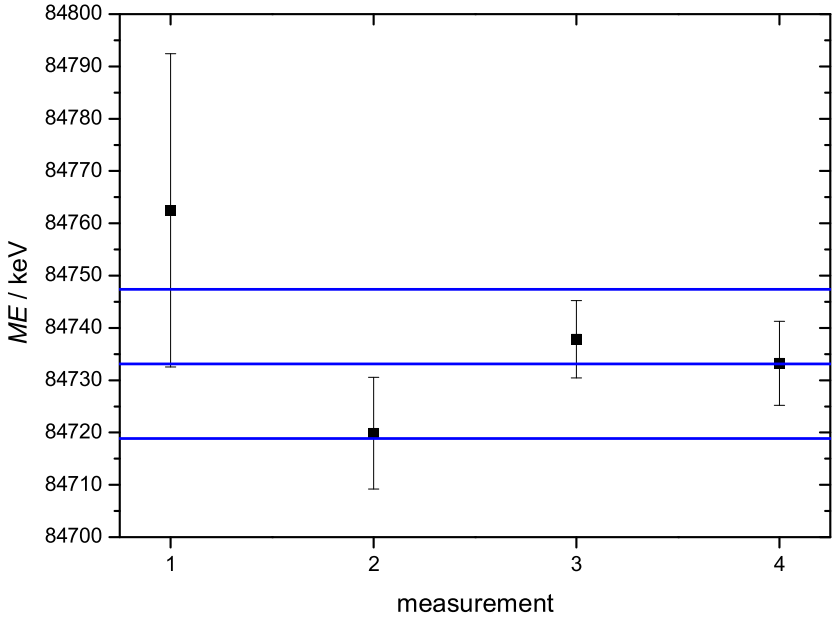

Figure 4.10: The results for the mass excesses of the individual measurements of the nobelium isotope ^{254}No are shown. The blue lines mark the average value and its uncertainty.

ms and three with T_{exc} = 900 ms. The values obtained from these four resonances are in agreement with each other (see Fig. 4.10). The residual frequency ratio was found to be $\overline{r}$ = 0.955908553(58). The resulting mass excess of ^{254}No is 84733(14) keV.

4.4 Mass determination of superheavy nuclides by α-decay energies

The determination of the masses of superheavy elements is at present based on the determination of α-decay energies. If a nuclide decays into the ground state of its daughter nuclide the difference of their mass excesses is directly related to the decay energy E_α. If the mother nuclide decays into an excited state of the daughter nuclide the energy level scheme of the latter has to be known to obtain reliable ground state masses. This is illustrated in Fig. 4.11. If the mass of the daughter nuclide is known, the mass of the mother nuclide can be determined and vice-versa. Many heavy nuclides are linked to stable nuclides by α-decay chains. Also the previous mass values of the three nobelium isotopes described in this work were based on α-decay chains. These measurements are discussed in the following.

In a general case the energy difference between mother and daughter nuclide can be obtained by comparing the energy before and after the decay. In the case of an

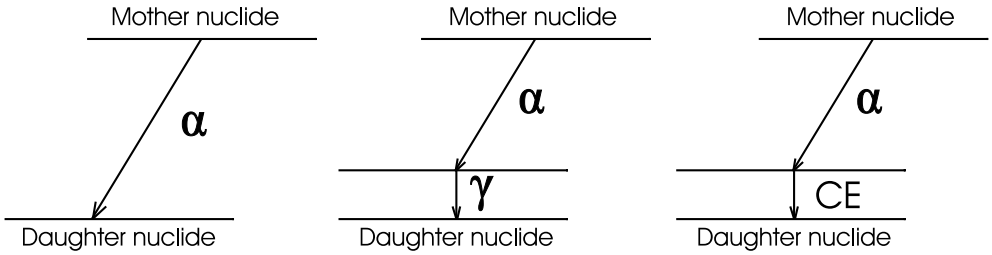

Figure 4.11: Sketch of three possible decay modes in an α-decay chain. In even-even nuclides - but sometimes also in other nuclides - the mother nuclide is decaying to the ground state of the daughter nuclide by emission of only one α particle (left). In other nuclides the decay from the mother nuclide populates an excited state of the daughter nuclide. In this case the excited daughter nuclide makes a transition from the excited state to the ground state either by emission of a γ quant (middle) or by transferring the excitation energy to a conversion electron (right).

α-decay the energies can be written as

$$M_{mother} = M_{daughter} + Q_\alpha + M(^4He). \tag{4.14}$$

The energy difference Q_α is now distributed to the energy of the excited state and - due to momentum conservation - to the kinetic energies of the daughter nuclide and the alpha particle. The Q_α value can thus be written as

$$Q_\alpha = \left(1 + \frac{m_\alpha}{m_{daughter}}\right) E_\alpha + E_{exc}. \tag{4.15}$$

Due to this formula one can determine the mass of a certain nuclide indirectly by measuring its α-decay energy E_α and the mass $m_{daughter}$ and excitation energy E_{exc} of its daughter nuclide.

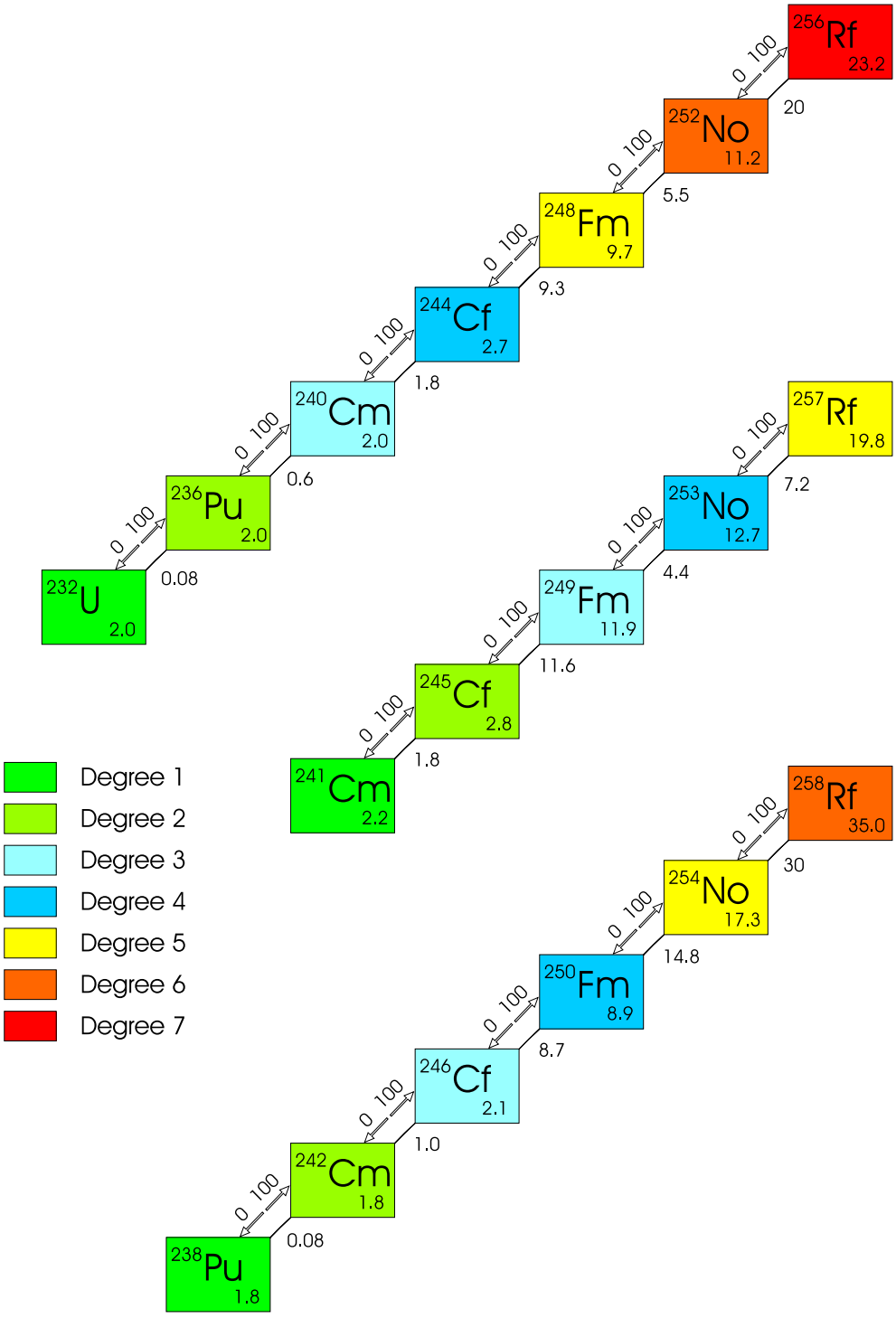

Figure 4.12: The mass determination based on the measurements of the Q_α values is illustrated. The SHIPTRAP data is not implemented yet. In the right lower corner of each box representing a nuclide its mass excess uncertainty is given in keV. On the right side of each line linking two nuclides the uncertainty of the corresponding Q_α value is shown. The two values on the left side of each link indicate how much the data influences each of the two connected nuclides. The degrees of the single nuclides are represented by different colours. Further details are discussed in Sec. 4.5.

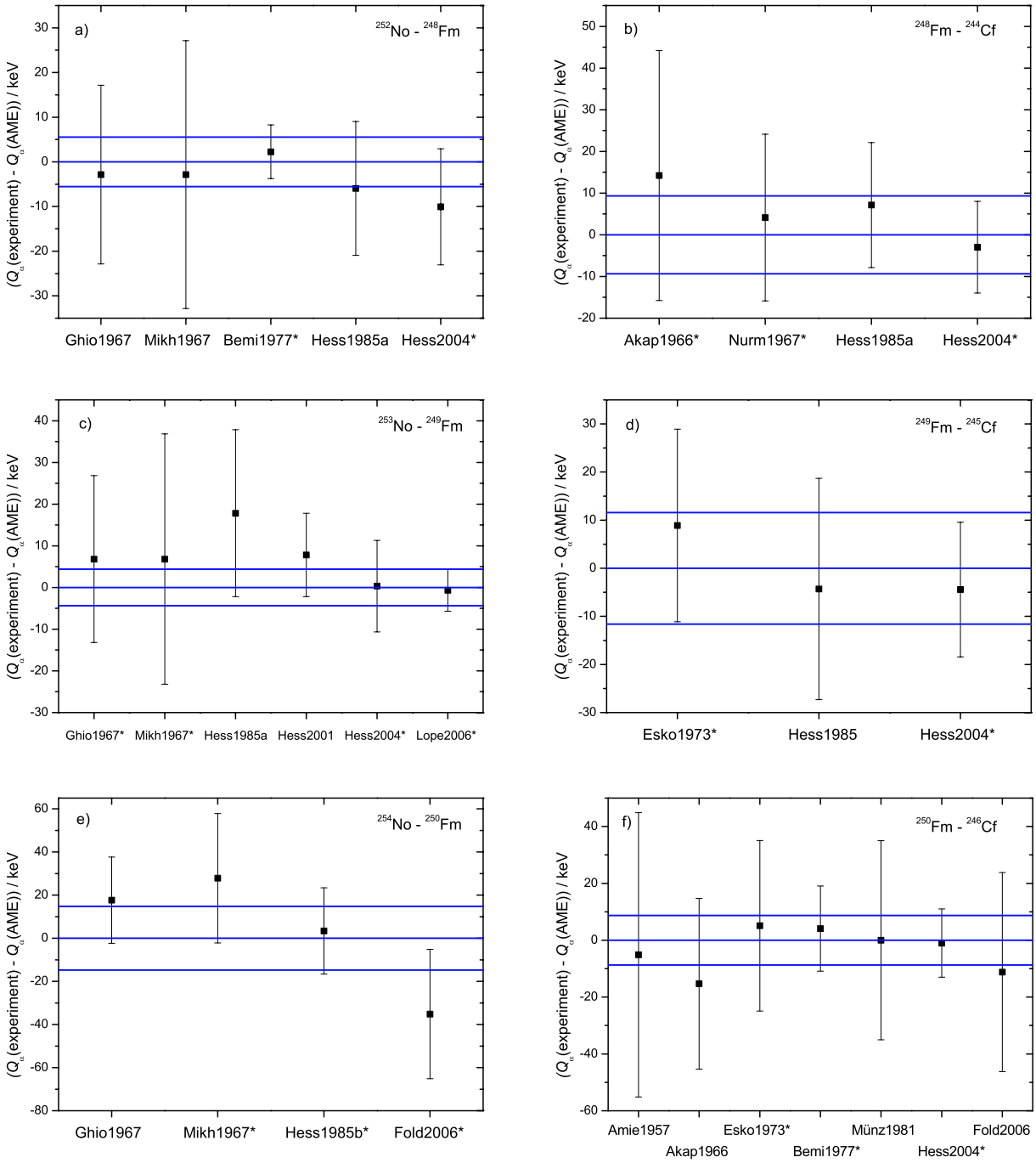

Figure 4.13: The results of the measurements of the Q_α value for the α decay from nobelium to fermium and fermium to californium are shown (black squares) and compared to the AME value (blue lines). The AME value is fixed to zero. The values of the references marked with * were used for the calculation of the AME value.

The mass value of the nobelium isotope ^{252}No was previously based on an α-decay chain ending in ^{232}U (see Fig. 4.12). Since this chain is consisting of even-even nuclei the most intense α-transitions are always occuring between the ground state of the mother nuclide and the ground state of the daughter nuclide. The most critical connections with respect to the mass uncertainty of ^{252}No in this chain are the decays from ^{252}No to ^{248}Fm and from ^{248}Fm to ^{244}Cf since they have relatively large uncertainties compared to the other decays in this chain. The measurements of these two α energies performed until now are shown in the Fig. 4.13(a) and (b), respectively. In both cases there is a very good agreement between the individual measurements. For the determination of the AME value only those data which contribute at least 10% to the final value are used. If there are two or more results obtained from the same experimental setup only the latest one is taken into account. The weight of a single measurement is here inversely proportional to the square of its uncertainty. Thus, in the case of the decay from ^{252}No to ^{248}Fm for instance, only the two values with the smallest uncertainties contribute to the final value. This leads to a Q_α value of 8548.7(5.5) keV for the decay from ^{252}No to ^{248}Fm and 7995.2(9.3) keV for the decay from ^{248}Fm to ^{244}Cf, where three experimental values are taken into account. The uncertainties of the Q_α values of the other decays down to ^{232}U are much smaller and have values of 1.8 keV for the decay from ^{244}Cf to ^{240}Cm, 0.6 keV for the decay from ^{240}Cm to ^{236}Pu and only 0.08 keV for the decay from ^{236}Pu to ^{232}U. The mass excess of the isotope ^{232}U, which is the end point of the α-decay chain, is known with an uncertainty of 1.96 keV. It was determined by the measurement of the energies of the α decay to ^{228}Th and the β^- decay of ^{232}Pa [Bjor1963, Gorm1972]. This uncertainty is mainly determining the uncertainties of the mass excesses of ^{236}Pu (1.96 keV), ^{240}Cm (2.04 keV) and ^{244}Cf (2.7 keV). The uncertainties of the mass excesses of ^{248}Fm (9.7 keV) and ^{252}No (11.2 keV), however, are mainly determined by the rather large uncertainties of the respective Q_α values.

The previous literature value of the isotope ^{253}No was based on an α-decay chain down to ^{241}Cm. The members of this decay chain are nuclides with even Z and odd N. For these nuclei in general the ground state to ground state transition of the α decay is not favored. Thus the excitation energy E_{exc} of the excited state that is populated in the α decay has to be known in each case in order to be able to estimate the Q_α value. Detailed decay schemes can be constructed from alpha-gamma coincidence measurements.

The decay scheme of ^{253}No to ^{249}Fm (see Fig. 4.14) has been studied at SHIP [Hess2004, Hess2007]. The favored α decay was the one from the $9/2^-$ [734] ground state of ^{253}No into the $9/2^-$ [734] state of ^{249}Fm with an E_α value of 8004(5) keV. This state is decaying by three different γ transitions: one transition into the $7/2^+$ [624] ground state (279.7 keV), one into a $9/2^+$ state (222.0 keV) and one into a $11/2^+$ state (151.4 keV). From the decay into the ground state a Q_α value of 8413(11) keV can be deduced. From this and other measurements (shown in Fig. 4.13(c)) an AME value of $Q_\alpha = 8412.2(4.4)$ keV was obtained.

In the case of the decay from ^{249}Fm to ^{245}Cf a mass determination is difficult due to a complicated decay scheme involving several excited states (see Fig. 4.14). Here the α decay from the $7/2^+$ [624] ground state of ^{249}Fm into the $7/2^+$ [624] (55(10) keV) excited state of ^{245}Cf (7520(12) keV) is expected to be followed by an E2 decay into

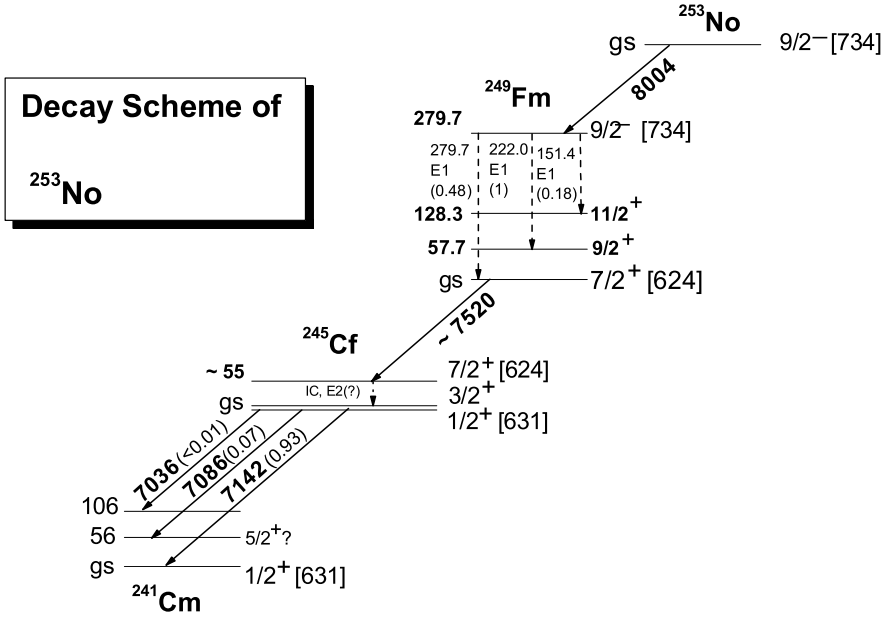

Figure 4.14: Decay scheme of ^{253}No [Hess2009]. The energies are given in keV. The numbers in brackets are the Nilsson levels. Details are given in the text.

a $3/2^+$ state and a subsequent M1 decay into the $1/2^+$ [631] ground state of ^{245}Cf. These decay energies are estimated from a deviation of the α-decay energy measured in [Hess2004] from previous experiments, which was ascribed to the presence of two conversion electrons.[5] γ rays or conversion electrons from the expected transitions $7/2^+$ to $3/2^+$ and $3/2^+$ to $1/2^+$, however, have not been measured so far. The results of the measurements performed on this decay are shown in Fig. 4.13(d). The resulting literature value is 7709.4(11.6) keV.

The Q_α value of the decay from ^{245}Cf to ^{241}Cm is known with an uncertainty of 1.8 keV. The mass excess of the isotope ^{241}Cm, which is at the end of this decay chain, was measured with a precision of 2.15 keV. Based on these two values the mass excess of ^{245}Cf can be determined with an uncertainty of 2.8 keV. The uncertainty of the mass excess of ^{249}Fm is - due to the rather big uncertainty of the Q_α value of the decay from ^{249}Fm to ^{245}Cf - determined to be 11.9 keV. This decay also limits the uncertainty of the mass excess of ^{253}No, which is 12.7 keV.

The mass of ^{254}No is again based on an α-decay chain which is consisting of even-even nuclides, resulting in ground-state to ground-state transitions. The decay chain is ending at the isotope ^{238}Pu.

The Q_α value of the decay from ^{254}No to ^{250}Fm has been measured several times (see Fig. 4.13(e)) and the resulting AME value is 8212.2(14.8) keV. Figure 4.13(f)

[5] If the mother nuclide is implanted into the silicon detector the conversion electrons contribute to the detector signal of the α decay. As consequence the measured value is higher than the α-decay energy. Other experiments where the mother nuclide is implanted into a foil in front of the detector only measure the energy of the α decay. From the difference of these two values the energy of the conversion electrons and thus the excitation energy can be estimated.

shows the results of the measurements of the Q_α value of the decay from ^{250}Fm to ^{246}Cf, which are resulting in an AME value of 7556.0(8.7) keV. The further Q_α values of this decay chain are known with relatively high accuracy as 1.0 keV for the decay from ^{246}Cf to ^{242}Cm and 0.08 keV for the decay from ^{242}Cm to ^{238}Pu.

The mass excess of ^{238}Pu could be measured with an uncertainty of 1.81 keV. Based on this measurement the mass excess uncertainty of ^{242}Cm is 1.81 keV and the one of ^{246}Cf 2.1 keV. Like in the previous two decay chains the mass excess uncertainties of the fermium and nobelium isotopes are limited by the uncertainty of the Q_α measurements: The uncertainty of the mass excess of ^{250}Fm is 8.9 keV and the one of ^{254}No is 17.3 keV.

4.5 Comparison of experimental results

In the AME 2003 [Audi2003] all three nobelium isotopes discussed in this work were known as secondary data. Their masses were determined from α-decay chains ending at a primary nucleus. This is ^{232}U in the case of ^{252}No, ^{241}Cm in the case of ^{253}No, and ^{238}Pu in the case of ^{254}No. Primary nuclides are defined by the fact that their masses are determined from a network of at least two other primary nuclides. Such nuclides obtain in the AME per definition the degree one. If only one primary nuclide is used for the mass determination of a nucleus, the data of this nucleus are called secondary data. Secondary data have different degrees starting from "2" if there is a direct link to a primary nucleus (for example in the case of ^{236}Pu in Fig. 4.12) and increasing with the number of nuclei in a data chain. Generally speaking the degree of a nuclide whose mass is determined using a link to a degree n nuclide is $n + 1$. The degrees of the nuclides of the three decay chains which are relevant in this case are indicated in Fig. 4.12 and Fig. 4.15 by a colour code. In such a data chain the nuclide of lower degree is influencing all the nuclides of higher degree by 100 %. The uncertainty of the mass determination of a nuclide is increasing with its degree since it includes the uncertainties of all lower degree nuclides determining it. To obtain more reliable data it is desirable to get more experimental input to have the possibility to convert more nuclides into primary nuclides.

Figure 4.12 shows the situation before implementing the SHIPTRAP data into the AME. The masses of the members of all three decay chains are based on a primary nuclide whose mass is known with a quite small uncertainy. Thus, the uncertainties of the masses of the higher degree nuclides are mainly limited by the uncertainties of the linking α decays. In all three cases the mass uncertainties of the nuclides up to californium are very small (around two to three keV). Starting from fermium the mass uncertainty increases due to higher uncertainties in the Q_α values. This is also affecting the mass uncertainties of the nobelium isotopes, even though the uncertainties of the Q_α values of the decay from nobelium to fermium are in the first two decay chains smaller than the ones of the decay from fermium to californium. The masses of the nobelium isotopes are, however, still known with an accuracy of about 10 to 20 keV.

Implementing the new mass values of SHIPTRAP determined from the mass ratio to ^{133}Cs - which is a primary data - results in a connection to two different primary

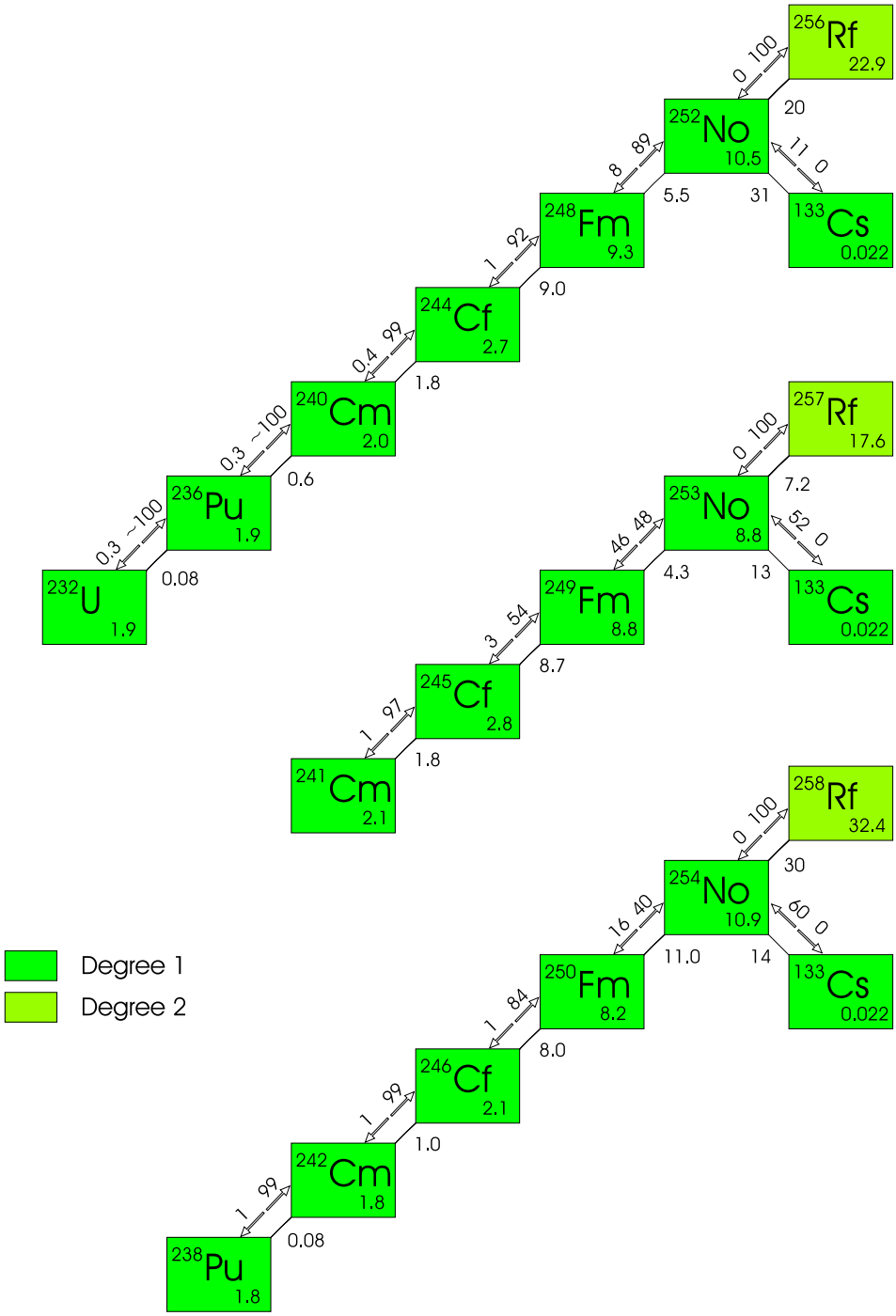

Figure 4.15: The mass determination based on the measurements of the Q_α values and the new implemented SHIPTRAP data is illustrated. In the right lower corner of each box representing a nuclide its mass excess uncertainty is given in keV. On the right side of each line linking two nuclides the uncertainty of the corresponding Q_α value is shown. The two values on the left side of each link indicate how much the data influences each of the two connected nuclides. The degrees of the single nuclides are represented by different colours.

nuclides for each of the three nobelium isotopes. Now all nuclides of this data chain will be influenced by each other and a loop of mutual dependence is achieved. Like this not only the nobelium isotope but every other nuclide in this decay chain will become primary data as well.

Figure 4.15 is showing the three decay chains after adding the SHIPTRAP data. One can see that in all three cases there is a remarkable influence resulting from the link to ^{133}Cs to the nobelium isotopes and its decay products. In the case of the decay chain of ^{252}No the SHIPTRAP value with an uncertainty of 31 keV is contributing 11% to the mass value of nobelium itself and 8.4% to the mass value of its daughter ^{248}Fm. The influence on the lighter decay products is negligible since they are determined more strongly by ^{232}U, which has a much smaller uncertainty and the linking Q_α values have high precisions. The mass excess uncertainty of ^{252}No is reduced from 11.2 keV to 10.5 keV. The mass excess values before and after including the new SHIPTRAP values are summarized in Tab. 4.3.

The result for the isotope ^{253}No has an even bigger influence on the new AME values as it was measured with an uncertainty of only 13 keV. This is the same as the uncertainty of the previous AME value. The contribution of the SHIPTRAP measurement to the new AME value is thus 52%. The uncertainty of the ^{253}No mass excess is so reduced to only 8.8 keV. In addition the mass value of ^{249}Fm is influenced by the new measurement by 46%, which leads to a reduction of its mass excess uncertainty from 12 keV to 8.8 keV. Also the Q_α value of the decay from ^{249}Fm to ^{245}Cf - which was the "weakest point" in the decay chain - is reduced from 12 keV to 8.8 keV. Moreover, it confirms the decay scheme suggested by [Hess2007], where an excitation energy of the ^{245}Cf nucleus of 55(10) keV was assumed. The lighter nuclides are only slightly affected by the implementation of the SHIPTRAP value.

The SHIPTRAP value of ^{254}No has an uncertainty of 14 keV compared to the uncertainty of 17 keV of the value determined from Q_α measurements and is thus mainly determining the new AME value, namely with a contribution of 60%. The mass excess uncertainty of ^{254}No is reduced to 11 keV and the uncertainty of the corresponding Q_α value is reduced from 15 keV to 11 keV. The contribution to the mass excess of the daughter nuclide ^{250}Fm is 16% and the influence on the lighter nuclides can be neglected.

The mass values of the higher Z nuclides in the three decay chains are affected in the same amount as the corresponding nobelium isotopes. They are to 100% determined by the mass value of the nobelium isotopes. In the case of ^{252}No the mass excess values can be deduced from Q_α values up to the hassium isotope ^{264}Hs, which has a mass excess uncertainty of 43 keV. Due to the small influence of the SHIPTRAP value this uncertainty remains unchanged.

The implementation of the new mass excess value of ^{253}No leads to a reduction of the uncertainty of its mother nuclide ^{257}Rf from 20 keV to 18 keV. The decay spectrum of the nuclide ^{261}Sg has also been ambiguously identified [Stre2009] so that the mass excess of ^{261}Sg can also be determined with an uncertainty in the order of 20 keV. This value, however, has not been implemented into the AME yet and is thus not shown in Tab. 4.3. The mass excesses of the nuclides ^{265}Hs and ^{269}Ds are estimated due to systematic trends.

Table 4.3: The influence of the nobelium data obtained at SHIPTRAP on the literature values is given. In the first column the nuclides are listed. The second and third column show the mass excess values for the nuclides as published in [Audi2003] as well as the status shortly before the SHIPTRAP measurements. The latter values are given in column 4. The fifth column shows the AME value after implementing the SHIPTRAP data. The contribution of the SHIPTRAP values to the new AME value is given in column six. The sign # means that the corresponding value is estimated due to systematic trends.

nuclide	AME2003	old AME2009	SHIPTRAP	new AME2009	contrib.
	ME / keV	ME / keV	ME / keV	ME / keV	
^{252}No	82881(13)	82866(11)	82850(31)	82864(11)	11%
^{253}No	84470#(100#)	84360(13)	84356(13)	84357.8(8.8)	52%
^{254}No	84724(18)	84711(17)	84733(14)	84725(11)	60%
^{232}U	34610.7(2.2)	34603.7(2.0)	-	34603.7(1.9)	0.3%
^{232}Pu	38366(18)	42895.7(2.0)	-	42895.7(1.9)	0.3%
^{238}Pu	46164.7(1.8)	46166.2(1.8)	-	46166.3(1.8)	0.7%
^{240}Cm	51725.4(2.3)	51718.4(2.1)	-	51718.4(2.0)	0.4%
^{241}Cm	53703.4(2.2)	53705.1(2.2)	-	53705.2(2.1)	1.5%
^{242}Cm	54805.2(1.8)	54806.7(1.8)	-	54806.73(1.8)	0.7%
^{244}Cf	61479.2(2.9)	61472.2(2.7)	-	61472.2(2.7)	0.7%
^{245}Cf	63386.9(2.9)	63388.6(2.8)	-	63388.6(2.8)	2.6%
^{246}Cf	64091.7(2.1)	64093.2(2.1)	-	64093.3(2.1)	0.9%
^{248}Fm	71906(12)	71892.3(9.7)	-	71891.0(9.3)	8.4%
^{249}Fm	73620#(100#)	73523(12)	-	73521.0(8.8)	46%
^{250}Fm	74074(12)	74074.1(9.0)	-	74077.7(8.2)	16%
^{256}Rf	94236(24)	94221(23)	-	94219(23)	11%
^{257}Rf	95930#(100#)	95829(20)	-	95827(18)	52%
^{258}Rf	96400#(200#)	96329(35)	-	96342(32)	60%
^{260}Sg	106580(40)	106568(38)	-	106568(38)	11%
^{261}Sg	108160#(130#)	108056#(75#)	-	108054#(74#)	52%
^{262}Sg	108420#(280#)	108354#(203#)	-	108367#(203#)	60%
^{264}Hs	119600(40)	119584(43)	-	119584(43)	11%
^{265}Hs	121170#(140#)	121068#(90#)	-	121065#(89#)	52%
^{266}Hs	121190#(280#)	121114#(204#)	-	121128#(204#)	60%
^{268}Ds	133940#(500#)	133289#(303#)	-	133289#(303#)	11%
^{269}Ds	135180#(140#)	135077#(92#)	-	135075#(92#)	52%
^{270}Ds	134810#(290#)	134735#(210#)	-	134749#(210#)	60%

The decay chain of the nuclide ^{254}No is interrupted. The decay from ^{258}Rf to ^{254}No has already been observed and the Q_α value is known with an uncertainty of 30 keV. This is the dominating contribution to the mass excess uncertainty of ^{258}Rf, which could be reduced from 35 keV to 32 keV by implementing the new SHIPTRAP data. The three higher-Z nuclides ^{262}Sg, ^{266}Hs and ^{270}Ds have been observed in the α-decay chain of the latter. For the nuclide ^{262}Sg, however, so far only spontaneous fission has been observed. Hence, these three heavy nuclides are not connected to the rest of the decay chain, which means that it is not possible to obtain reliable information on their masses. An experiment to measure the α decay of ^{262}Sg is planned for the year 2010. If it is possible to measure the α-decay energy of ^{262}Sg the masses of the decay chain members up to ^{270}Ds can be determined.

The new data obtained at SHIPTRAP thus contribute to the new literature values not only of the nobelium isotopes but also of other nuclides connected to them via α-decay chains. In this way the SHIPTRAP results have mentionable impact on mass excess and Q_α values down to fermium and up to hassium. All nuclides in the three decay chains up to the element nobelium are now becoming primary nuclides. The area of nuclides with well-known mass values has for the first time been extended to region of transuranium nuclides and thus moved a step closer to the expected island of stability.

4.6 Comparison of the experimental results with the theoretical predictions

After including the new experimental data of SHIPTRAP into the AME the new literature values are now compared with the results of theoretical calculations. Although the accuracy of the theoretical predictions is far from the accuracy of the measurement, a comparison between both is an indication for the quality of a theoretical model. The three decay chains of the investigated nobelium isotopes already reach to an atomic number Z which is quite close to the one of the expected island of stability. If a model is in good approximation reproducing the experimental mass values of the nuclides in these decay chains it may also give reliable prediction for the nuclides in the region of the island of stability. Furthermore nuclear mass models can give information about systematic trends and predict the influence of effects like for example shell closures and deformation.

From the several theoretical models introduced in Chap. 2 two macroscopic-microscopic models - the finite-range liquid drop model (Sec. 2.2.3) [Möll1995] and the finite-range droplet model (Sec. 2.2.4) [Möll1995] - and two purely microscopic models based on Skyrme interaction (Sec. 2.3) - the SHF-BCS model [Erle2009] and the HFB-17 model [Gori2009] - are chosen for comparison. Figure 4.16 shows a comparison between the results of these four models and the AME values after implementing the new SHIPTRAP data (see column five of Tab. 4.3). For the SHF-BCS model an uncertainty was implemented into the calculation. The results of the other three models are given without uncertainty. Only members of the decay chains of the three nobelium isotopes discussed in this thesis are shown. The heaviest element which is shown is darmstadtium ($Z = 110$).

It is obvious that even for high-Z elements like hassium or darmstadtium the uncertainty of the experimental data are small compared to the deviation between the predictions of the individual mass models. The FRLDM and the microscopic SHF-BCS model obviously provide results which are systematically too high in this region. The results of the FRDM are systematically too low. The best agreement with the experimental data is achieved with the HFB-17 model, which is a remarkable progress for a purely microscopic model.

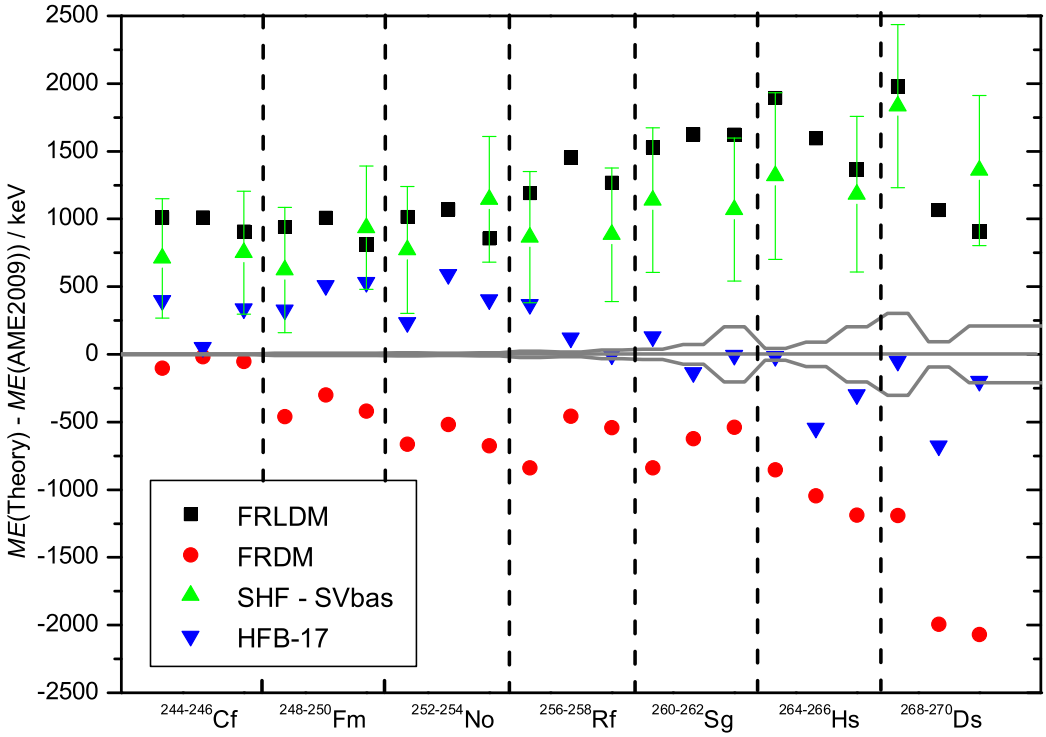

Figure 4.16: The results of several theoretical models are compared with the AME values after implementing the new SHIPTRAP data. The results of the FRLDM and the FRDM are taken from [Möll1995]. Skyrme-Hartree-Fock BCS calculations performed with the SVbas parametrization [Erle2009] and the HFB-17 [Gori2009] have been chosen as examples for recent microscopic models. The corrections for the electron binding energies have been taken from [Rodr2004]. The grey lines represent the experimental values with error bars after implementing the new SHIPTRAP data into the AME.

The theoretical results cannot contribute much to the discussion of the nobelium masses. They can, however, make predictions for heavier unknown nuclides which are probably reliable within a mass excess uncertainty of about 1 MeV. For the identification of an unknown nuclide this is a very helpful indication. The identification

of a nuclide due to α-decay chains is only unambiguous if the chain is ending in a known nuclide. This is not always the case, especially if very neutron-rich nuclides are explored. The identification is then mainly done due to systematic trends in comparison with neighbouring nuclides. Theoretical predictions for the mass and the half-life can act as additional evidence for the identification of an unknown nuclide. Especially reliable predictions for the half-lifes of individual decay modes (mostly α decay, decay by conversion electron and spontaneous fission) are very important.

For the further development of theoretical mass models new mass values are of great importance. The fit parameters of a model have to be adjusted to mass values that are well-known. A model can only be called "global" if it describes the properties of all nuclides comparably well. This is, of course, difficult to achieve. A nuclide with a very small number of nucleons, for example, can hardly be described by a mean-field. On the other hand it is difficult to give reliable results for heavy masses without having nuclides in this region that can act as anchor points. For global mass models it is necessary to have these anchor points spread over the whole nuclear chart. The three nobelium isotopes ^{252}No, ^{253}No and ^{254}No are now finally doubtlessly established as such anchor points in the region of heavy elements. They can be used to adjust the fit parameters of the different mass models to obtain a better agreement between theoretical predictions and experimental results. In this way, for the first time directly measured masses of transfermium elements can be included into theoretical investigations.

4.7 The first direct mass measurement on lawrencium

In April 2009 one isotope of the element lawrencium with $Z = 103$ was measured. The biggest challenge of direct mass measurement in this region of the nuclear chart are of course the low production rates of the nuclei of interest.

The nuclide ^{255}Lr, which has a half-life of $T_{1/2} = 22(4)$ s, is produced in the reaction ^{48}Ca + ^{209}Bi in the 2n channel with a cross section of about 200 nb. This corresponds to about ten ions per minute entering the gas cell. This very low count rate complicated the optimization of the degrader thickness in front of the gas cell. This optimization was done with the silicon detectors since they provide a reliable identification of the lawrencium isotope ^{255}Lr due to its α-decay energy. Additionally, with a silicon detector it is possible to detect all ^{255}Lr atoms regardless of their charge state.

The ^{255}Lr nuclide was entering the traps as both, singly and doubly charged ions. To record the time-of-flight resonance one needs to choose between these two charge states. Thus, one first had to find out which charge state is more numerous. This was done with time-of-flight measurements on the MCP detectors in combination with activity measurements on the silicon detectors.

With this measurement it was observed that there was approximately the same number of ions in both charge states ^{255}Lr^{+} and ^{255}Lr^{2+}, which is the most disadvantageous case and results in a factor of two reduction in the available rate for a mass measurement. A measurement of a time-of-flight resonance for ^{255}Lr^{2+} would have led to a smaller uncertainty because of the higher frequency. It was, however,

decided to take a resonance of $^{255}Lr^{+}$ since for this q/m region a lower background was observed.

Despite the extreme low resulting count rate of only 1 ion per hour entering the Penning traps it was still possible to take a time-of-flight resonance. If all frequency

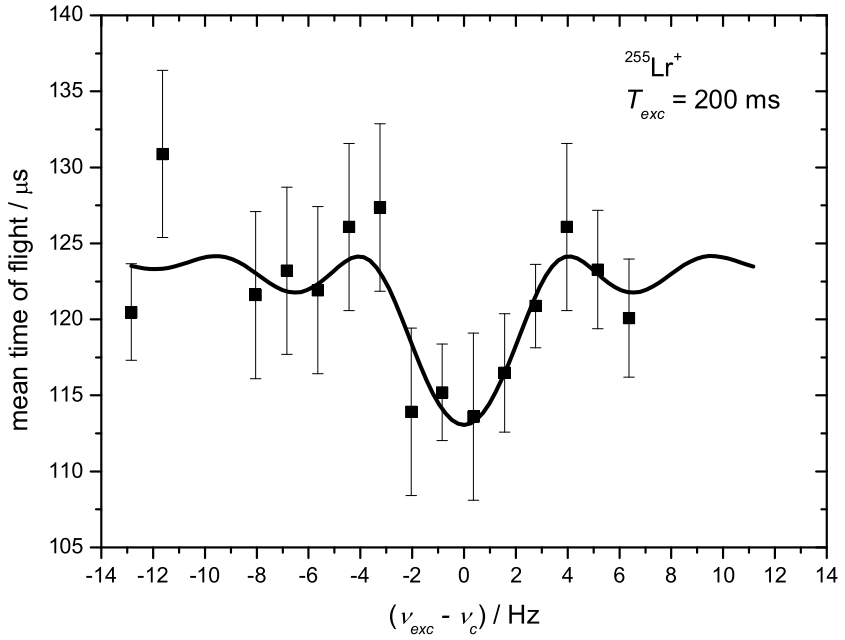

Figure 4.17: The time-of-flight resonance of $^{255}Lr^{+}$ which was obtained during the beamtime in April 2009 is shown. Due to the very low statistics only 21 data points were taken (in six of them no ion was observed). Altogether around 30 ions could be recorded in two days. The solid line is a fit of the theoretical line shape to the experimental data points. The cyclotron frequency was determined to be $\nu_c = 421662.42(45)$ Hz.

scans of $^{255}Lr^{+}$, which were taken in a time interval of about two days, are added one obtains a resonance dip. Due to the low count rate the number of frequency points for this measurement were reduced from normally 41 to 21. Altogether around 30 $^{255}Lr^{+}$ ions were detected. This resonance dip is shown in Fig. 4.17 and proves that it was possible to trap $^{255}Lr^{+}$ ions in the precision trap and to excite them. ^{255}Lr is thus the nuclide with the lowest cross section and the heaviest radionuclide ever trapped in a Penning trap.

Even with this low statistics a mass evaluation is possible, however, with a quite large uncertainty. The relative uncertainty of the frequency determination is $2.0{\cdot}10^{-6}$ which results in a mass excess uncertainty of around 250 keV. In addition to this uncertainty the uncertainty due to magnetic field fluctuations has to be taken into account. Since the measurement time of the resonance was about two days the usually performed linear interpolation of the magnetic field cannot apply here since the time between the calibration measurements was too long. One has to add an uncertainty that corrects for the fluctuations of the magnetic field due to day-night

temperature fluctuations. This additional uncertainty is, however, smaller than the uncertainty due to the poor statistics. This can be estimated from reference measurements performed during other experiments. During the nobelium beamtime of August 2008, for example, the cyclotron frequency of the reference ion $^{133}Cs^{+}$ was varying in a range of 0.3 Hz. This corresponds to a change in the mass excess of about 100 keV. Additionally, a long-lived isomer ($T_{1/2}$ = 22(4) s) [Anta2008] is known for ^{255}Lr. Since it was not resolved the excitation energy of about 50 keV has also to be added quadratically to the uncertainty. It can thus be estimated that the determination of the mass excess of ^{255}Lr was done with an accuracy of about 270 keV, which is in the vicinity of the uncertainty of the AME value [Audi2003] of 200 keV. The AME mass excess value of ^{255}Lr is, however, only estimated from systematic trends. The difference between the AME value and the SHIPTRAP value is around 300 keV, which means that the values are in agreement with each other within their uncertainties.

This very first resonance gives an ideal motivation and starting point for the next experimental run. It marks a further improvement of the SHIPTRAP facility which is now able to perform measurements on nuclides which are produced with production rates of only a few ions per minute.

5 Summary and outlook

In this thesis the first direct mass measurements ever performed on transfermium nuclides were presented and discussed. These measurements have been carried out with the high-precision mass spectrometer SHIPTRAP at GSI (Darmstadt). They mark a first step towards direct mass measurements of superheavy elements with Penning traps.

In chapter 2 of this thesis several mass models were summarized, starting from the liquid drop model until more advanced macroscopic-microscopic and purely microscopic approaches which are still in use today. The results of the single mass models are still deviating a lot from each other as well as to the experimental values, which makes it necessary to obtain more experimental mass values as input data for theoretical calculations.

Our pioneering work demonstrates that Penning traps allow us to obtain accurate mass values even for the very heavy nuclides that are only available with minute production rates. For radionuclides in the lower mass range a relative uncertainty of 10^{-9} can be achieved [Boll2006]. Measurements on transfermium ions, however, impose difficult experimental conditions. The limiting factor is in many cases not the half-life of an atom but the low production rate, which is in the order of only about one ion per second or less for the nobelium isotopes presented here.

The cyclotron frequencies of the nobelium ions were measured with the time-of-flight ion cyclotron resonance detection technique [Gräf1980]. With this technique about hundred ions per resonance are needed to obtain a mass value, which leads to measurement times of several hours.

The mass excesses of the nobelium ions could be determined with uncertainties around 10 to 30 keV. The results confirm previous mass values obtained from Q_α measurements. Despite their low production rates the masses were determined with relative uncertainties of less than 10^{-7}.

Apart from the measurements on nobelium isotopes it was possible to advance even one atomic number higher to the element lawrencium. A first time-of-flight resonance was obtained demonstrating that a mass measurement is still possible. Even from just one measurement lasting two days the mass value of the isotope ^{255}Lr could be determined with an uncertainty of about 300 keV. This result agrees with the AME value which was based only on the estimation of systematic trends. Since ^{255}Lr is an odd-even nucleus the α decays in the decay chain of ^{255}Lr are often going to excited states which are mostly unknown. Thus, the new result presented in this work is very useful to confirm the previously made estimations. The next objective for SHIPTRAP will be to improve this measurement aiming not only at a smaller uncertainty but also on the resolution of the isomeric state. Recording resonances with higher statistics will be possible due to a recently implemented temperature and pressure stabilization system [Droe2009], which reduces the uncertainty of the

magnetic field.

It was thus proved that it is possible at SHIPTRAP to perform detailed studies on superheavy elements with well-defined conditions. The high energetic evaporation residues which were produced at several MeV were decelerated to low energies and were accessible for further investigations. With the help of the Penning traps an isobarically clean ensemble could be obtained on which spectroscopic studies with low background can be performed. The first trap-assisted decay spectroscopy measurement at SHIPTRAP has been performed in September this year [Droe2009]. Here, the nuclides $^{204-207}$Rn and ^{213}Ra were investigated. This method will also be applied to heavier elements and will allow unambiguous identification of the decay scheme of a nuclide and can even give information on the occupation numbers of isomeric state and ground state. The selection due to the q/m ratio can here act as a very helpful tool to distinguish between nuclides whose α-decay energies cannot be resolved with a silicon detector.

The nuclides with higher Z than ^{255}Lr are in principle also accessible with the existing SHIPTRAP setup. Despite even lower cross sections, measurements with the time-of-flight ion cyclotron resonance method are possible if the magnetic field can be kept constant over a long time. To be able to take resonances over a long time it is crucial to guarantee a stable magnetic field since the uncertainty in mass determination is limited by magnetic field fluctuations. These fluctuations are - apart from the decrease due to flux creep - mostly resulting from temperature and pressure changes. For this reason a temperature and pressure stabilization system has been set up at SHIPTRAP which reduces the magnetic field uncertainty by about one order of magnitude [Droe2009]. With these stable conditions it may become possible to record a resonance over time intervals in the order of two days with uncertainties below 10^{-7}.

To further improve the efficiency of SHIPTRAP a new cryogenic gas stopping cell is being developed and will be manufactured soon. With this gas cell it will be possible to obtain a higher gas density at the same pressure since the temperature will be reduced from room temperature to 77 K. This will lead to a smaller stopping distribution and thus to a higher stopping efficiency. In addition the extraction efficiency can be increased due to the fact that it is then possible to apply higher RF amplitudes at the extraction funnel. Furthermore the cleanliness will be improved.

In order to get in the future access to ions with production rates well below 1/second even to one 1/minute, a new non-destructive detection scheme based on the measurement of induced image currents will be implemented at SHIPTRAP. This Fourier transform ion cyclotron resonance (FT-ICR) technique [Kete2006] allows the measurement of the cyclotron frequency with a single trapped ion. The recorded ion signal is amplified with a resonant circuit which has to be tuned to the cyclotron frequency of the ion of interest. The frequency is then obtained by Fourier transformation. In an ideal case one ion is enough to perform a frequency measurement. This is an important advantage compared to the TOF-ICR method, were about hundred ions are needed for a precise frequency determination. A system like this has already been designed and is implemented in the TRIGA-TRAP experiment [Kete2008].

Furthermore, it will be possible in the future to obtain a beam intensity which is a

factor of ten higher than at the moment. This will be achieved by using a new ECR source and a continuous beam. If the beam current used at SHIP is not limited by the melting temperature of the target this is resulting in higher production rates of the nuclides of interest.

Another important project which will be addressed in the future is the connection of SHIPTRAP to the gas-filled TASCA separator. In opposite to SHIP, TASCA has high transmission efficiencies for asymmetric reactions with light projectile beams on actinide targets. It will thus provide the possibility to investigate products from hot-fusion reactions with actinide targets. This will enable the access to more neutron-rich nuclides, which are of interest because they belong to α-decay chains which are directly linked to the nuclides of the expected island of stability.

In the long-term future the Penning trap technique might be crucial for investigations on long-lived nuclides which are belonging to the island of stability. If these nuclides really are close to stability it will be very difficult to detect them via decay chains due to a too long correlation time. In this case Penning traps can provide the - perhaps only - possibility for addressing these exotic species.

Bibliography

[Akap1966] G.N. Akapev, A.G. Demin, V.A. Druin, E.G. Imaev, I.V. Kolesov, Y.V. Lobanov, L.P. Pashchenko, Atomnaya Energiya 21 (1966) 243.

[Amie1957] S. Amiel, A. Chetham-Strode, Jr., G.R. Choppin, A. Ghiorso, B.G. Harvey, L.W. Holm, S.G. Thompson, Phys. Rev. 106 (1957) 553.

[Ande1962] P.W. Anderson, Phys. Rev. Lett. 9 (1962) 309.

[Ande1964] P.W. Anderson, Y.B. Kim, Rev. Mod. Phys. 39 (1964) 39.

[Anta2008] S. Antalic, F.P. Heßberger, S. Hofmann, D. Ackermann, S. Heinz, B. Kindler, I. Kojouharov, P. Kuusiniemi, M. Leino, B. Lommel, R. Mann, K. Nishio, Š. Šáro, B. Streicher, B. Sulignano, M. Venhart, Eur. Phys. J. A 38 (2008) 219.

[Audi2003] G. Audi, A.H. Wapstra, C. Thibault, Nucl. Phys. A 729 (2003) 337.

[Belo2003] A.V. Belozerov, M.L. Chelnokov, V.I. Chepigin, T.P. Drobina, V.A. Gorshkov, A.P. Kabachenko, O.N. Malyshev, I.M. Merkin, Yu.Ts. Oganessian, A.G. Popeko, R.N. Sagaidak, A.I. Svirikhin, A.V. Yeremin, G. Berek, I. Brida, Š. Šáro, Eur. Phys. J. A 16 (2003) 447.

[Bemi1977] C.E. Bemis, R.L. Ferguson, F. Plasil, R.J. Silva, F. Pleasonton, R.L. Hahn, Phys. Rev. C 15 (1977) 705.

[Bend1998] M. Bender. *Exotische Atomkerne im Skyrme-Hartree-Fock-Modell*, Dissertation, Johann Wolfgang Goethe-Universität Frankfurt a.M. (1998).

[Bend1999] M. Bender, K. Rutz, P.-G. Reinhard, J.A. Maruhn, W. Greiner, Phys. Rev. C 60 (1999) 034304.

[Bend2001] M. Bender, W. Nazarewicz, P.-G. Reinhard, Phys. Lett. B 515 (2001) 42.

[Bend2003] M. Bender, P.-H. Heenen, and P.-G. Reinhard, Rev. Mod. Phys. 75 (2003) 121.

[Bjor1963] S. Bjornholm, F. Boehm, A.B. Knutsen, O.B. Nielsen, Nucl. Phys. 42 (1963) 469.

[Blau2003] K. Blaum, G. Bollen, F. Herfurth, H.-J. Kluge, M. Kuckein, S. Heinz, P. Schmidt, L. Schweikhard, J. Phys. B 36 (2003) 921.

[Blau2006] K. Blaum, Phys. Rep. 425 (2006) 1.

[Bloc2007] M. Block, D. Ackermann, K. Blaum, A. Chaudhuri, Z. Di, S. Eliseev, R. Ferrer, D. Habs, F. Herfurth, F.P. Heßberger, S. Hofmann, H.-J. Kluge, G. Maero, A. Martín, G. Marx, M. Mazzocco, M. Mukherjee, J.B. Neumayr, W.R. Plaß, W. Quint, S. Rahaman, C. Rauth, D. Rodríguez, C. Scheidenberger, L. Schweikhard, P.G. Thirolf, G. Vorobjev, C. Weber, Eur. Phys. J. D 45 (2007) 39.

[Bohr1939] N. Bohr and J. A. Wheeler, Phys. Rev. 56 (1939) 426.

[Boll1990] G. Bollen, R.B. Moore, G. Savard, H. Stolzenberg, J. Appl. Phys. 68 (1990) 4355.

[Boll1992] G. Bollen, H.-J. Kluge, M. König, T. Otto, G. Savard, H. Stolzenberg, R.B. Moore, G. Rouleau, G. Audi, ISOLDE Collaboration, Phys. Rev. C 46 (1992) R2140.

[Boll1996] G. Bollen, S. Becker, H.-J. Kluge, M. König, R.B. Moore, T. Otto, H. Raimbault-Hartmann, G. Savard, L. Schweikhard, H. Stolzenberg, ISOLDE Collaboration, Nucl. Instr. Meth. A 368 (1996) 675.

[Boll2004] G. Bollen, Lect. Notes Phys. 651 (2004) 169.

[Boll2006] G. Bollen, D. Davies, M. Facina, J. Huikari, E. Kwan, P.A. Lofy, D.J. Morrissey, A. Prinke, R. Ringle, J. Savory, P. Schury, S. Schwarz, C. Sumithrarachchi, T. Sun, L. Weissman, Phys. Rev. Lett. 96 (2006) 152501.

[Brow1986] L.S. Brown, G. Gabrielse, Rev. Mod. Phys. 58 (1986) 233.

[Cwio2005] S. Cwiok, P.-H. Heenen, W. Nazarewicz, Nature 433 (2005) 705.

[Czas2004] A. Czasch, *Doppelt hoch angeregte Zustände von Helium: Partielle Wirkungsquerschnitte und Winkelverteilungen der Elektronenemession*, Dissertation, Johann Wolfgang Goethe-Universität Frankfurt am Main, Germany (2004).

[Daws1995] P.H. Dawson, *Quadrupole mass spectrometry and its applications*, American Institute of Physics, Elsevier Scientific Publishing Company, New York (1995).

[Dehm1990] H. Dehmelt, Rev. Mod. Phys. 62 (1990) 525.

[Droe2009] C. Droese, *Minimierung des systematischen Fehlers und Hochpräzisionsmassenmessungen an neutronenarmen Rn- und Ra-Isotopen mit SHIPTRAP*, diploma thesis, Ernst-Moritz-Arndt Universität Greifswald (2009).

[Eite2008] G. Eitel, *Aufbau eines ortsauflösenden Ionennachweisdetektors für die Penningfallen-Massenspektrometrie*, diploma thesis, Johannes Gutenberg-Universität Mainz (2008).

[Eite2009] G. Eitel, M. Block, A. Czasch, M. Dworschak, S. George, O. Jagutzki, J. Ketelaer, J. Ketter, Sz. Nagy, D. Rodríguez, C. Smorra, K. Blaum, Nucl. Instr. Meth. A 606 (2009) 475.

[Elis2007] S. Eliseev, M. Block, A. Chaudhuri, Z. Di, D. Habs, F. Herfurth, H.-J. Kluge, J.B. Neumayr, W.R. Plass, C. Rauth, P.G. Thirolf, G. Vorobjev, Z. Wang, Nucl. Instr. Meth. B 258 (2007) 479.

[Elis2007a] S. Eliseev, M. Block, A. Chaudhuri, F. Herfurth, H.-J. Kluge, A. Martín, C. Rauth, G. Vorobjev, Int. J. Mass Spectrom. 262 (2007) 45.

[Erle2009] J. Erler, private communication (2009).

[Esko1973] P. Eskola, Phys. Rev. C 7 (1973) 280.

[Fler1983] G.N. Flerov, G.M. Ter-Akopian, Rep. Prog. Phys. 46 (1983) 817.

[Fold2006] C.M. Folden, S.L. Nelson, Ch.E. Düllmann, J.M. Schwantes, R. Sudowe,P.M. Zielinski, K.E. Gregorich, H. Nitsche, D.C. Hoffman, Phys. Rev. C 73 (2006) 014611.

[Fren1937] J. Frenkel, Phys. Rev. 55 (1937) 987.

[Frit2001] T. Fritioff, C. Carlberg, G. Douyasset, R. Schuch, I. Bergström, Eur. Phys. J. D 15 (2001) 141.

[Gabr2008] G. Gabrielse, Int. J. Mass Spec. 279 (2008) 107.

[Gägg1989] H.W. Gäggeler, D.T. Jost, A. Türler, P. Armbruster, W. Brüchle, H. Folger, F.P. Heßberger, S. Hofmann, G. Münzenberg, V. Ninov, W. Reisdorf, M. Schädel, K. Sümmerer, J.V. Kratz, U. Scherer, M.E. Leino, Nucl. Phys. A 502, (1989) 561.

[Gell1992] R. Geller, P. Ludwig and G. Melin, Rev. Sci. Instrum. 63 (1992) 2795.

[Geor2007] S. George, K. Blaum, F. Herfurth, A. Herlert, M. Kretzschmar, S. Nagy, S. Schwarz, L. Schweikhard, C. Yazidjian, Int. J. Mass Spectrom. 264 (2007) 110.

[Ghio1967] A. Ghiorso, T. Sikkeland, M.J. Nurmia, Phys. Rev. Lett. 18 (1967) 401.

[Gori2009] S. Goriely, N. Chamel, J.M. Pearson, Phys. Rev. Lett. 102 (2009) 152503.

[Gorm1972] J. Gormann, A. Rytz, H.V. Michel, Comptes Rendus Hebdomadaires des Séances de l'Académie des Science, serie B 275 (1972) 291.

[Gräf1969] G. Gräff, E. Klempt, G. Werth, Z. Phys. 222 (1969) 201.

[Gräf1980] G. Gräff, H. Kalinowsky, J. Traut, Z. Phys. 297 (1980) 35-39.

[Herz2006] R.-D. Herzberg, P.T. Greenlees, P.A. Butler, G.D. Jones, M. Venhart, I.G. Darby, S. Eeckhaudt, K. Eskola, T. Grahn, C. Gray-Jones, F.P. Heßberger, P. Jones, R. Julin, S. Juutinen, S. Ketelhut, W. Korten, M. Leino, A.-P. Leppänen, S. Moon, M. Nyman, R.D. Page, J. Pakarinen, A. Pritchard, P. Rahkila, J. Sarén, C. Scholey, A. Steer, Y. Sun, Ch. Theisen, J. Uusitalo, Nature 442 (2006) 896.

[Hess1985] F.P. Heßberger, G. Münzenberg, S. Hofmann, W. Reisdorf, K.H. Schmidt, H.J. Schött, P. Armbruster, Z. Phys. A 321 (1985) 317.

[Hess1985a] F.P. Heßberger, GSI report (1985).

[Hess1985b] F.P. Heßberger, G. Münzenberg, S. Hofmann, Y.K. Agarwal, K. Poppensiecker, W. Reisdorf, K.-H. Schmidt, J.R.H. Schneider, W.F.W Schneider, H.J. Schött, P. Armbruster, B. Thuma, C.-C. Sahm, D. Vermeulen, Z. Phys. A 322 (1985) 557.

[Hess2001] F.P. Heßberger, GSI report (2001).

[Hess2004] F.P. Heßberger, S. Hofmann, D. Ackermann, P. Cagarda, R.-D. Herzberg, I. Kojouharov, P. Kuusiniemi, M. Leino, R. Mann, Eur. Phys. J. A 22 (2004) 417.

[Hess2007] F.P. Heßberger, Eur. Phys. J. D 45 (2007) 33.

[Hess2007a] F.P. Heßberger, Phys. At. Nucl. 70 (2007) 1445.

[Hess2009] F.P. Heßberger, private communication (2009).

[Hofm2000] S. Hofmann, G. Münzenberg, Rev. Mod. Phys. 72 (2000) 733.

[Jagu2002] O. Jagutzki, V. Mergel, K. Ullmann-Pfleger, L. Spielberger, U. Spillmann, R. Dörner, H. Schmidt-Böcking, Nucl. Instr. Meth. A 477 (1-3) (2002) 244.

[Kell2003] A. Kellerbauer, K. Blaum, G. Bollen, F. Herfurth, H.-J. Kluge, M. Kuckein, E. Sauvan, C. Scheidenberger, L. Schweikhard, Eur. Phys. J. D 22 (2003) 53.

[Kete2006] J. Ketelaer, *Developement of a non-destructive Fourier Transform-Ion Cyclotron Resonance detection system for singly charged ions in a cryogenic Penning trap*, Diploma thesis, Johannes Gutenberg-Universität Mainz (2006).

[Kete2008] J. Ketelaer, J. Krämer, D. Beck, K. Blaum, K. Eberhardt, G. Eitel, R. Ferrer, C. Geppert, S. George, F. Herfurth, J. Ketter, Sz. Nagy, D. Neidherr, R. Neugart, W. Nörtershäuser, J. Repp, C. Smorra, N. Trautmann, C. Weber, Nucl. Instr. Meth. A 594 (2008) 162.

[Klug2004] H.-J. Kluge, K. Blaum, C. Scheidenberger, Nucl. Instr. Meth. A 532 (2004) 48.

[Klüp2008] P. Klüpfel *Skyrme's Interaction Beyond the Mean-Field: The DGCM+GOA Hamiltonian of Nuclear Quadrupole Motion*, Dissertation, Friedrich-Alexander-Universität Erlangen-Nürnberg (2008).

[Köni1991] M. König, *Massenspektrometrische Auflösung von Isomer und Grundzustand in einer Penningfalle und Untersuchungen zur Coulombwechselwirkung gespeicherter Ionen*, PHD thesis, Johannes Gutenberg-Universität Mainz (1991).

[Köni1995] M. König, G. Bollen, H.-J. Kluge, T. Otto, J. Szerypo, Int. J. Mass Spec. Ion Process. 142 (1995) 95.

[Kret1991] M. Kretzschmar, Eur. J. Phys. 12 (1991) 240.

[Kret1999] M. Kretzschmar, AIP Conference Proceedings 457 (1999) 242.

[Lamb1987] G.R. Lambertson, *Dynamic Devices - Pickups and Kickers*, AIP Conference Proceedings 153 (1987).

[Lamp1987] M. Lampton, O. Siegmund, R. Raffanti, Rev. Sci. Instrum. 58 (1987) 2298.

[Lope2006] A. Lopez-Martens, K. Hauschild, A.V. Yeremin, A.V. Belozerov, Ch. Briançon, M.L. Chelnokov, V.I. Chepigin, D. Curien, O. Dorvaux, B. Gall, V.A. Gorshkov, M. Guttormsen, F. Hanappe, A.P. Kabachenko, F. Khalfallah, A. Korichi, A.C. Larsen, O.N. Malyshev, A. Minkova, Yu.Ts. Oganessian, A.G. Popeko, M. Rousseau, N. Rowley, R.N. Sagaidak, S. Sharo, A.V. Shutov, S. Siem, A.I. Svirikhin, N.U.H. Syed, Ch. Theisen, Phys. Rev. C 74 (2006) 044303.

[Majo2005] F.G. Major, V.N. Gheorghe, G. Werth, *Charged Particle Traps: Physics and Techniques of Charged Particle Field Confinement* (Springer Series on Atomic, Optical, and Plasma Physics, Vol. 37). Springer, Berlin (2005).

[Mang1975] H.J. Mang, Phys. Rep. 18 (1975) 325.

[Maye1948] M. G. Mayer, Phys. Rev. 74 (1948) 235.

[McMi1949] E. McMillan, P.H. Abelson, Phys. Rev. 57 (1940) 1185.

[Meld1967] H. Meldner, Arkiv för fysik 36 (1967) 593.

[Mikh1967] V.L. Mikheev, V.I. Ilyushchenko, M.B. Miller, S.M. Polikanov, G.N. Flerov, Yu.P. Kharitonov, Atomnaya Energiya 22 (1967) 90.

[Möll1992] P. Möller, J.R. Nix, Nucl. Phys. A 549 (1992) 84.

[Möll1994] P. Möller, J.R. Nix, J. Phys. G 20 (1994) 1681.

[Möll1995] P. Möller, J.R. Nix, W.D. Myers and W.J. Swiatecki, *Nuclear ground-state masses and deformations*, At. Data Nucl. Data Tables 59 (1995) 185.

[Mose1969] U. Mosel, W. Greiner, Z. Phys. 222 (1969) 261.

[Mukh2008] M. Mukherjee, D. Beck, K. Blaum, G. Bollen, J. Dilling, S. George, F. Herfurth, A. Herlert, A. Kellerbauer, H.-J. Kluge, S. Schwarz, L. Schweikhard, C. Yazidjian, Eur. Phys. J. A 35 (2008) 1.

[Münz1979] G. Münzenberg, W. Faust, S. Hofmann, P. Armbruster, K. Güttner, E. Ewald, Nucl. Instr. Meth. 161 (1979) 65.

[Münz1981] G. Münzenberg, S. Hofmann, F.P. Heßberger, W. Reisdorf, K.H. Schmidt, J.H.R. Schneider, P. Armbruster, Z. Phys. A 300 (1981) 107.

[Myer1966] W. Myers and W. Swiatecki, Nucl. Phys. 81 (1966) 1.

[Neum2006] J.B. Neumayr, L. Beck, D. Habs, S. Szerypo, P.G. Thirolf, V. Varentsov, F. Voit, D. Ackermann, D. Beck, M. Block, Z. Di, S.A. Eliseev, H. Geissel, F. Herfurth, F.P. Heßberger, S. Hofmann, H.-J. Kluge, M. Mukherjee, G. Münzenberg, G. Petrick, W. Quint, S. Rahaman, C. Rauth, D. Rodríguez, C. Scheidenberger, G. Sikler, Z. Wang, C. Weber, W.R. Plaß, M. Breitenfeld, A. Chaudhuri, G. Marx, L. Schweikhard, A.F. Dodonov, Y. Novikov, M. Suhonen, Nucl. Instr. Meth. B 244 (2006) 489.

[Nils1969] S.G. Nilsson, C.F. Tsang, A. Sobiczewski, Z. Szymanski, S. Wycech, C. Gustafson, I.-L. Lamm, P. Moeller, B. Nilsson, Nucl. Phys. A 131 (1969) 1.

[Nurm1967] M. Nurmia, T. Sikkeland, R. Silva, A. Ghiorso, Phys. Lett. B 26 (1967) 78.

[Ogan2007] Yu. Oganessian, J. Phys. G: Part Phys. 34 (2007) R165.

[Paty1991] Z. Patyk, A. Sobiczewski, Nucl. Phys. A 533 (1991) 132.

[Poth1990] H. Poth, *Electron Cooling: Theory, Experiment, Application*, CERN-EP/90-04 (1990).

[Raha2005] S. Rahaman, *First on-line mass measurements at SHIPTRAP and mass determination of neutron-rich Fr and Ra isotopes at ISOLTRAP*, PhD thesis, Ruprecht-Karls-Universität Heidelberg (2005).

[Raut2006] C. Rauth, *Direct mass measurements beyond the proton drip-line*, PhD thesis, Ruprecht-Karls-Universität Heidelberg (2006).

[Rein1987] P.-G. Reinhard and K. Goeke, Rep. Prog. Phys. 50, 1 (1987).

[Reis1992] W. Reisdorf, M. Schädel, Z. Phys. A 343 (1992) 47.

[Ring1980] P. Ring and P. Schuck, *"The Nuclear Many-Body Problem"*, Springer, Heidelberg (1980).

[Rodr2003] D. Rodríguez Rubiales, *An RFQ buncher for accumulation and cooling of heavy radionuclides at SHIPTRAP and high precision mass measurements on unstable Kr isotopes at ISOLTRAP*, PhD thesis, University of Valencia (2003).

[Rodr2004] G.C. Rodrigues, P. Indelicato, J.P. Santos, P. Patté, F. Parente, Atomic Data and Nucl. Data Tables 86 (2004) 117.

[Roen] RoentDek Handels GmbH, Kelkheim Ruppertshain, http://www.roentdek.de.

[Roen09] RoentDek Handels GmbH, MCP Delay Line Detector Manual, version 9.17.205.2 (2009).

[Roos2004] J. Van Roosbroeck, C. Guénaut, G. Audi, D. Beck, K. Blaum, G. Bollen, J. Cederkall, P. Delahaye, A. De Maesschalck, H. De Witte, D. Fedorov, V.N. Fedoseyev, S. Franchoo, H.O.U. Fynbo, M. Górska, F. Herfurth, K. Heyde, M. Huyse, A. Kellerbauer, H.-J. Kluge, U. Köster, K. Kruglov, D. Lunney, V.I. Mishin, W.F. Mueller, Sz. Nagy, S. Schwarz, L. Schweikhard, N.A. Smirnova, K. Van de Vel, P. Van Duppen, A. Van Dyck, W.B. Walters, L. Weissmann, C. Yazidjian, Phys. Rev. Lett. 92 (2004) 112501.

[Sava1991] G. Savard, St. Becker, G. Bollen, H.-J. Kluge, R.B. Moore, Th. Otto, L. Schweikhard, H. Stolzenberg, U. Wiess, Phys. Lett. A 158 (1991) 247.

[Scha2001] H. Schatz, A. Aprahamian, V. Barnard, L. Bildsten, A. Cumming, M. Ouellette, T. Rauscher, F.-K. Thielemann, M. Wiescher, Phys. Rev. Lett. 86 (2001) 3471.

[Schw1990] W. Schwab, *Experimente zur Elektronenkühlung am Niederenergie-Antiprotonen-Speicherring (LEAR)*, PhD thesis, KfK 4673 (1990).

[Seab1946] G.T. Seaborg, E.M. McMillan, J.W. Kennedy, A.C. Wahl, Phys. Rev. 69 (1946) 366.

[Seab1990] G.T. Seaborg, W.D. Loveland, *The Elements Beyond Uranium*, Wiley, New York (1990).

[Shaf1985] R.E. Shafer, *Characteristics of Directional Beam Position Monitors*, IEEE Trans. on Nucl. Sci., NS-32, No.5 (1985).

[Smol1995] R. Smolanczuk, A. Sobiczewski, Proc. EPS Conf. "Low energy Nuclear Dynamics", St. Petersburg 1995, edited by Yu. Ts. Oganessian *et al.*, World Scientific, Singapore, New Jersey, London, Hong Kong (1995) 313.

[Sold2008] A. Solders, I. Bergström, Sz. Nagy, M. Suhonen, R. Schuch, Phys. Rev. A 78 (2008) 012514.

[Ston2007] J.R. Stone and P.-G. Reinhard, Prog. Part. Nucl. Phys. 58, 587 (2007).

[Stre2009] B. Streicher, F.P. Heßberger, S. Antalic, S. Hofmann, D. Ackermann, S. Heinz, B. Kindler, I. Kojouharov, P. Kuusiniemi, M. Leino, B. Lommel, R. Mann, Š. Šáro, B. Sulignano, M. Venhart, submitted to EPJ (2009).

[Stru1967] V.M. Strutinsky, Nucl. Phys. A 95 (1967) 420.

[Stru1968] V.M. Strutinsky, Nucl. Phys. A 122 (1968) 1.

[Stur2007] S. Sturm, *Implementation of a mass separation method in the Penning trap REXTRAP and investigation of space-charge related phenomena*, Diploma Thesis, Ruprecht-Karls-Universität Heidelberg (2007).

[Suli2007] B. Sulignano, S. Heinz, F.P. Heßberger, S. Hofmann, D. Ackermann, S. Antalic, B. Kindler, I. Kojouharov, P. Kuusiniemi, B. Lommel, R. Mann, K. Nishio, A.G. Popeko, S. Saro, B. Streicher, M. Venhart, A.V. Yeremin, Eur. Phys. J. A 33 (2007) 327.

[TRIM] http://www.srim.org/

[Vaut1972] D. Vautherin and D.M. Brink, *Hartree-Fock Calculations with Skyrme's Interation. I. Spherical Nuclei*, Phys. Rev. C 5 (1972) 626.

[Vaut1973] D. Vautherin, *Hartree-Fock Calculations with Skyrme's Interation. II. Axially Deformed Nuclei*, Phys. Rev. C 7 (1973) 296.

[Weiz1935] C.F. von Weizsäcker, Z. Phys. 96 (1935) 431.

[Wern2008] J. Werner, *Flugzeitmassenspektroetrie und Designstudie für einen neuen RF-Quadrupol-Buncher bei SHIPTRAP*, Bachelor thesis, Justus-Liebig-Universität Gießen (2008).